

Copyright

by

Anjum Shagufta Mukadam

2004

The Dissertation Committee for Anjum Shagufta Mukadam  
certifies that this is the approved version of the following dissertation:

## **Ensemble Characteristics of the ZZ Ceti stars**

Committee:

---

D. E. Winget, Supervisor

---

S. O. Kepler

---

E. L. Robinson

---

J. C. Wheeler

---

J. Liebert

---

H. C. Harris

# **Ensemble Characteristics of the ZZ Ceti stars**

by

**Anjum Shagufta Mukadam, B.S., M.S., M.A.**

## **Dissertation**

Presented to the Faculty of the Graduate School of

The University of Texas at Austin

in Partial Fulfillment

of the Requirements

for the Degree of

**Doctor of Philosophy**

**The University of Texas at Austin**

August 2004

to you, Dad.

# Acknowledgments

*To teach someone is the most selfless thing one can do. I am indebted to my teachers for bestowing upon me the honor of knowledge.*

I am grateful to my advisor, Don, for believing in me when I didn't and for helping me grow. Don taught me to be more optimistic, and is chiefly responsible for developing my skills in scientific writing. I have a Hubble fellowship today, and I owe a large part of it to Don. Don's enthusiasm for science is very contagious, and I will never forget all the intense discussions in the WET lab. These moments remind us of why we are there in the first place.

No words could express the gratitude I feel for Ed. I am honored to have assisted him in building Argos, the efficient frame transfer CCD photometer. I got my fair share of being yelled at whenever I made silly mistakes. :- ) Had Argos not been the optical wonder that it is, my thesis would certainly not have been as good. I cannot thank Ed enough for his genius in conceiving Argos. Ed is solely responsible for my developing any computer skills at all, though I still have a long way to go. Ed and Don tried very hard that I should learn the difference between models and reality, and have been partially successful. I think it will take me a few years more to truly graduate.

Kepler is practically my co-advisor, who helped me immensely during the first few years of my Ph.D. with a lot of code, when I did not know where to

turn. Kepler was always friendly enough that I did not hesitate to ask him a lot of silly questions, and his support helped me gain confidence. I also thank him for introducing me to Chef's orange beef at the Chinese restaurant, Tien Hong.

Rob is the best teacher I have ever come across. He is exceptionally thorough, and possesses an impressive span of knowledge in diverse areas. I have fond memories of many arguments that I have had with Rob, and I was wrong on practically each of those occasions. I treasure a lot of admiration and respect for Rob, and I have certainly learnt a few lessons from him.

Atsuko taught me how to observe, taught me how things operate in the WET lab, and is the one I have to thank for helping me develop a veteran attitude towards my work. When I was a baby graduate student, she helped me merge in a different culture in a strange country, and she was always a big sister watching out for me. I learnt a lot of the everyday programming from her, and I could not imagine how I would ever make it through when she graduated.

Travis was the only other senior student at the time I joined the WET lab. I saw Travis as a cool, confident computer-geek, who had assembled the cluster Darwin to crunch out white dwarf evolutionary models. Travis was the first to teach me how to reduce data with IRAF, a useful skill. I enjoyed having lunch with Travis on the days when we did not have group lunch. During these times, we would discuss our day-to-day work and show each other plots about what we had been up to. This helped anticipate questions that other people may have, and I thank Travis for all those lunches together.

Scot taught me how to observe **well** with the 3-channel photometer. It took me a few days after he had left the mountain to assimilate all that he had taught me, which was very difficult in his intimidating presence. Scot helped me along the way in my first few years, but I got a chance to collaborate with him extensively when we started searching for variables in the Sloan Digital Sky

Survey. I began to appreciate the big brother in all of Scot's feedback after a few months. Thanks for looking out for me. I would like to thank Antonio profusely for his data reduction algorithms, which I used extensively during my search for new ZZ Ceti stars and for their subsequent analysis. Antonio also helped during the commissioning run of Argos, and has been a warm and kind inspiration.

I am very lucky to have observed extensively with Denis, a diligent observer and sound instrumentalist, who taught me quite a few things about observing. I had a lot of good discussions about my work with Denis during my last two years in Austin, as we were the only people working in the lab at the time. In stressful times, Denis always brought good cheer and helped me cope. He also tried, as did Ed, that I should learn to make better plots. In return, I tried to help them appreciate Indian folk music. :-)

Ted arrived in our group during the last two years of my stay. He helped us in achieving a higher success rate in discovering ZZ Ceti stars than the photometric method we were using at the time. Ted has been a kind, and supportive unofficial committee member, who helped me during the commissioning run of Argos, and also with subsequent observations. Ted has tried hard to teach me the genteel way of communication, rather than the abrupt and blunt manner that I am used to. :-) I can't say that he has been successful.

Mukremin taught me how to carry out spectroscopic observations at the 2.7m telescope at McDonald Observatory, and also showed me how to reduce spectroscopic data. Mukremin is a dear brother to me, and he has always lent me a shoulder to cry on, specially during the last couple years of my dissertation. I have always found his calm confident way of tackling problems, and his mature insights most admirable. I look up to him.

I overlapped with Mikemon for a bit, when he was trying to graduate. I thank him for dropping me to the airport in his car filled with pizza boxes at

that time. Mikemon returned to the WET lab six years later as a post-doc, only a few months before I was trying to graduate. I thank him once again for another ride to the airport in his new car devoid of pizza boxes. Times and people change. :-) Mikemon helped me get a physical insight about stellar pulsations, something I had failed to achieve even after six years in the WET lab. I am very grateful to him for helping me put together the fifth chapter of my thesis.

I feel sincere gratitude towards Dr. Frank Bash, without whose financial contribution, Argos may have remained a design on paper, and this thesis would have been quite different from what it has turned out to be. I also thank him for sending a letter to the US Consulate in Mumbai, that certainly helped me in getting back to the United States to finish writing my thesis. I am grateful to my committee member, Craig, for all his advice and more importantly, financial support for meetings and observing runs from the Cox funds. :-) I also thank Dr. Chris Sneden for bailing me out of tight spots by providing partial financial assistance from the dept. funds. I also thank Pawan for his support, and encouragement during my last few years in Austin. It is unfortunate that we did not get a chance to work together on a project that we had planned. I owe Derek Wills a special thanks for loaning me \$200 when I first arrived in the dept. from India, and I had only \$30 left to see me through the first one month. I also owe a special thanks to Dr. David Lambert, who has always encouraged me and suggested that I should apply for a Hubble fellowship.

I thank Phillip McQueen for helping me conceive the baffle design for Argos. I really appreciate all his time, knowing how tight his schedule is. I thank David Boyd and Gordon Wesley for the time and effort put in designing the mount for Argos, and also for taking the time to teach me about various useful tools. I thank Jimmy and George for helping us fix various mechanical problems with the Argos mount, for machining the baffles for Argos, and for

building the mount for Cyclops, a camera used to track the location of the dome slit. I also thank Jimmy and David Boyd for giving me my first lessons in using heavy machinery. I thank Gary Hansen and Doug Edmonston, who built a timing circuit for precise instrument timing. I also thank Fred Harvey for helping me with tasks concerning electronics.

I have no words to thank David Doss enough, for his advice and his insights, that I have been utilizing ever since I started observing six years ago. Dave has helped us immensely in fixing various problems with Argos, since the commissioning run of the instrument. His service and support remain unparalleled. I also thank Earl Green for a lot of discussions about instrument or telescope problems, that occur ever so often. I also thank Bob Franke, Kevin Meyer, Terry Wilemon, Mark Blackley, Darrin Cook, Marian Frueh, and Ed Dutchover for all their help and support. I also thank Patricia, Robert, and Miguel for making long runs bearable by providing good food, and for washing all the dirty dishes.

I also thank my graduate coordinators, Elizabeth Korves and Stephanie Crouch. You were lifesavers for twits like me, who never knew what forms had to be filled or when the submission deadlines were. I bow down to the efficiency, patience, and perseverance shown by Cindy Thompson, without whom we would have missed a lot of deadlines we could not afford to. I am also grateful for all the computing support given to me by Mark Cornell, Ron Wilhelm, Bill Spiesman, Martha Schaefer, and now Chris Wilkinson, Dario Landazuri, and Anita Cochran. I have to specially thank Peter Hoeflich for linux support at times when I was ready to tear my hair out. I thank Henry Cantu for making the mess, that are research grants, more legible to clueless selves like me and my advisor. I thank both Mae Collins and Bob Worley for helping with purchasing equipment, and Sherry for reimbursements. I thank Estela, then Melissa, and now Jamie Woods for helping with travel arrangements. I thank Yolanda, and

now Estela, for making sure that I was paid.

I thank Karen, Maegan, and Davis Winget for hosting a really nice graduation party. I am indebted to my friends Navin and Swati Palicherla, Don and Karen Winget, Srikant and Gauri, Randy and Gayathri, Anuroopa Shenoy, and Mikemon for a roof to stay under while working on my thesis. I would also like to thank all my batch mates, and all my friends and well-wishers in astronomy. You made the six years that I spent in Austin enjoyable, and I thank all the people with extra-soft shoulders for the times that weren't fun. I thank Mukremin, David Reaves, Atsuko, Scot, Kepler, Denis, Mikemon, Antonio, Mike Endl, Tommy Greathouse, Joe Tufts, Nairn, Marsha, Rica, Agnes Kim, Diane Paulson, Rob Hynes, Todd Watson, Bev and Derek Wills. I thank Priya for proof-reading various manuscripts of mine, and Rohit Grover for incessantly advising me about proper formatting of my thesis and all my plots. :-)

Last, but not the least, I thank my beloved MP for the immense support that you have given me ever since I arrived in Austin. I always poured all my troubles on you, and you soaked them dry till life was sunny for me again. And also thank you for re-doing my whole presentation in power point on the eve of my defense, at a time when I was struggling with low resolution PDF slides. Thanks for being there for six years.

ANJUM SHAGUFTA MUKADAM

*The University of Texas at Austin*

*August 2004*

# Ensemble Characteristics of the ZZ Ceti stars

Publication No. \_\_\_\_\_

Anjum Shagufta Mukadam, Ph.D.  
The University of Texas at Austin, 2004

Supervisor: D. E. Winget

Global pulsations of stars can be used to probe their interiors, similar to the method of using earthquakes to explore the Earth's interior. This technique, called asteroseismology, is the only systematic way to study stellar interiors. White dwarf stars represent a relatively simple stellar end state for most main sequence stars like the Sun. This is because they are not expected to have any central nuclear fusion and their evolution is dominated by cooling. These stars are scientifically interesting since they contain a fossil record of their previous evolution. Their high densities and temperatures make them good cosmic laboratories to study fundamental physics under extreme conditions. Besides, white dwarfs are not as centrally condensed as some other classes of variables, and hence the observed pulsations sample their interior better.

Each pulsation mode is an independent constraint on the structure of the star. We can probe stellar structure and composition by finding a single star rich in pulsation modes, and/or by finding a large number of pulsators to use the method of ensemble asteroseismology. A fraction of white dwarf pulsators are observed to be extremely stable clocks; this property allows us to look for

any orbiting planets. The drift rates of these stable clocks are expected to reveal the stellar cooling rate. Including this information in evolutionary white dwarf models allows us to determine the age of the star. Since most stars evolve into white dwarfs, we can use the distribution of white dwarf ages in different parts of the Galaxy to constrain the age of the Galaxy and its evolution. Variable white dwarfs can also be used as a means to measure Galactic distances. All these reasons motivate us to search for additional white dwarf pulsators.

Four out of five white dwarfs show hydrogen in their outermost layers and are classified as DAs. These are observed to pulsate in a temperature range of 11000–12000 K. I decided to search specifically for DA white dwarf variables (DAVs), also known as ZZ Ceti stars. To substantially increase the sample of ZZ Ceti stars, I was forced to search at greater distances (or fainter magnitudes). This is because various research groups around the world have already examined the relatively nearby (or bright) candidates for variability. Hence, I helped Dr. R. E. Nather in building a high speed time-series CCD photometer for the prime focus of the 2.1 m telescope at McDonald Observatory. This CCD instrument allows us to obtain usable time-series data on 19th magnitude objects, as opposed to a limiting magnitude of 17 with our previous instrument. The combination of an efficient new instrument and a large amount of telescope time ( $\approx 100$  nights/yr) gave me a unique opportunity to search extensively for new ZZ Ceti stars.

Other members of my research group also contributed towards the 15 month long observations at McDonald Observatory, and helped me in data analyses. We pre-selected candidates by using the photometric and spectroscopic observations of the Sloan Digital Sky Survey. I present 35 new pulsating DA (hydrogen atmosphere) white dwarf stars discovered from the Sloan Digital Sky Survey (SDSS) and the Hamburg Quasar Survey (HQS). This increases the sample

of 39 known ZZ Ceti stars to 74; the first ZZ Ceti star was accidentally discovered in 1968.

This is the first time in the history of white dwarf variables that we have a homogeneous set of spectra acquired using the same instrument on the same telescope, and with consistent data reductions, for a statistically significant sample of ZZ Ceti stars. The homogeneity of the spectra reduces the scatter in the spectroscopic temperatures; we have essentially re-defined the ZZ Ceti instability strip. We find a narrow ZZ Ceti strip of width  $\simeq 1000$  K, as opposed to the previous determination of 1500 K. We question the purity of the DAV instability strip as we find several non-variables within. We present our best fit for the red (cool) edge and our constraint for the blue (hot) edge of the instability strip, determined using a statistical approach.

I also present the observed pulsation spectra of 67 ZZ Ceti stars with reliable spectroscopic temperatures. I verify the well-established relation of the increase in observed pulsation periods and amplitudes for the new ZZ Ceti stars, traversing from the blue to the red edge of the instability strip. The data on the new ZZ Ceti stars suggests that pulsation amplitude declines prior to the red edge. This means that ZZ Ceti pulsations do not shut down abruptly at the red edge of the instability strip. This is the first possible detection of such an effect.

# Contents

<b>Acknowledgments</b>	<b>v</b>
<b>Abstract</b>	<b>xi</b>
<b>Chapter 1 Introduction</b>	<b>1</b>
1.1 White dwarfs: fossils of stars . . . . .	1
1.2 White dwarf variables: the inside story . . . . .	3
1.2.1 Short term seismology: structural constraints . . . . .	4
1.2.2 Long term seismology: drifting pulsation periods . . . . .	6
1.3 Motivation: why search for DAVs? . . . . .	7
1.3.1 Stellar structure . . . . .	8
1.3.2 Stable clocks can be used to find planets . . . . .	8
1.3.3 DAV seismology helps cosmochronometry . . . . .	9
1.3.4 Seismological distances from a flickering candle . . . . .	12
1.4 My dissertation . . . . .	13
1.4.1 Establishing the ZZ Ceti instability strip . . . . .	14
1.4.2 Ensemble seismology of the ZZ Ceti stars . . . . .	15
<b>Chapter 2 Ideal time-series photometer</b>	<b>16</b>
2.1 Time-series photometry and ideal instrumentation . . . . .	16
2.2 Argos: designed for time-series photometry . . . . .	19

2.2.1	The CCD camera . . . . .	19
2.2.2	Wavelength response . . . . .	21
2.2.3	Instrument timing . . . . .	24
2.2.4	The prime focus mount . . . . .	26
2.2.5	Baffling Argos . . . . .	29
2.3	Noise and measurement in photometry . . . . .	30
2.4	Time keeping with stellar clocks . . . . .	36
2.4.1	Uncertainty in period . . . . .	36
2.4.2	Uncertainty in phase . . . . .	37
2.4.3	Uncertainty in drift rate measurements . . . . .	38
2.5	Reflections . . . . .	41
<b>Chapter 3 Search for new ZZ Ceti stars</b>		<b>42</b>
3.1	Selection of DAV candidates from databases . . . . .	42
3.1.1	Sloan digital sky survey . . . . .	42
3.1.2	Hamburg quasar survey . . . . .	43
3.2	Techniques to select the SDSS DAV candidates . . . . .	43
3.2.1	Photometric technique for the SDSS DAV candidates . . . . .	44
3.2.2	Equivalent width technique for the SDSS DAV candidates . . . . .	45
3.2.3	Spectroscopic technique for the SDSS DAV candidates . . . . .	46
3.3	Spectroscopic technique for HQS DAV candidates . . . . .	48
3.4	Data acquisition and analysis . . . . .	50
3.4.1	Observing strategy . . . . .	50
3.4.2	Data acquisition . . . . .	51
3.4.3	Data reduction and results . . . . .	51
3.5	Pulsation properties of the new ZZ Ceti variables . . . . .	58
3.6	Conclusions . . . . .	59

<b>Chapter 4 Empirical DAV Instability Strip</b>	<b>63</b>
4.1 Empirical instability strip . . . . .	64
4.1.1 Biases in candidate selection . . . . .	66
4.1.2 Non-uniform detection efficiency . . . . .	67
4.1.3 Uncertainties in temperature and $\log g$ determinations . . .	69
4.2 Probing the non-uniform DAV distribution using pulsation periods	72
4.3 Questioning the impurity of the instability strip . . . . .	75
4.4 Narrow width of the ZZ Ceti strip . . . . .	77
4.5 Empirical blue and red edges . . . . .	78
4.5.1 Technique . . . . .	79
4.5.2 Estimating the uncertainties . . . . .	82
4.5.3 Comparison with empirical edges . . . . .	83
4.5.4 Comparison with theoretical edges . . . . .	83
4.6 Conclusion . . . . .	84
<b>Chapter 5 ZZ Ceti Ensemble characteristics</b>	<b>86</b>
5.1 Pulsations in ZZ Ceti models . . . . .	86
5.1.1 Growth of amplitude . . . . .	87
5.1.2 Fluid motions in the star . . . . .	88
5.2 Trends across the instability strip . . . . .	89
5.2.1 Observed pulsation periods . . . . .	89
5.2.2 Observed pulsation amplitudes . . . . .	91
5.2.3 Mode density . . . . .	93
5.3 Drifting eigenmodes . . . . .	93
5.4 Why study ZZ Ceti stars as an ensemble? . . . . .	95
5.5 Teaching different DAVs to play the same tune . . . . .	96
5.5.1 Scaling the pulsation spectra . . . . .	96
5.6 Conclusions . . . . .	108

<b>Chapter 6 Summary and future work</b>	<b>110</b>
6.1 Seismology of the ZZ Ceti stars . . . . .	110
6.1.1 Benefits of an ensemble of DAVs . . . . .	111
6.2 Ideal instrumentation for the DAV search . . . . .	111
6.3 Fruitful search for the ZZ Ceti stars . . . . .	113
6.4 Empirical ZZ Ceti instability strip . . . . .	114
6.5 Ensemble characteristics of the ZZ Ceti stars . . . . .	114
6.6 Future work . . . . .	115
<b>Bibliography</b>	<b>118</b>
<b>Vita</b>	<b>129</b>

# Chapter 1

## Introduction

### 1.1 White dwarfs: fossils of stars

White dwarf stars are the stellar remains of 98–99% of stars in the sky (Weidemann 1990), and contain an archival record of their main sequence lifetime. We can harness this archival record from white dwarfs relatively easily, instead of studying stars on the main sequence directly.

White dwarf cores contain 99.99% of the star by mass. Masses of white dwarf stars exhibit a narrow distribution around  $0.6M_{\odot}$  (e.g. Finley, Koester, & Basri 1997; Bergeron et al. 2001; Silvestri et al. 2001; Madej, Należyty, & Althaus 2004). The high density in the core serves to ionize it completely, and the core is immersed in a sea of electrons. The degenerate electrons make the core isothermal. However, the ions in the core remain non-degenerate. Degeneracy pressure supports the electrons, while the massive ions are subject to the contracting force of gravity. Charge separation between the ions and the electrons then allows the forces of gravity and degeneracy pressure to balance each other.

The core composition of a white dwarf is effectively determined by nuclear reaction rates in the red giant stage. White dwarf cores do not undergo

any further nuclear fusion, and their composition remains unaltered. Therefore, white dwarfs allow us the opportunity to study nuclear reaction rates  $^{12}\text{C}(\alpha, \gamma)^{16}\text{O}$  in red giant cores, without the inconvenience of central nuclear fusion (Metcalf, Winget, & Charbonneau 2001; Metcalfe, Salaris, & Winget 2002; Metcalfe 2003).

White dwarf spectra reveal that 80% of them have atmospheres dominated by hydrogen (DAs; Fleming, Liebert, & Green 1986), and  $\lesssim 20\%$  have atmospheres dominated by helium (DBs). This insulating outer layer controls the rate at which the residual thermal energy of the ions in the isothermal core is radiated into space. White dwarf evolution is dominated by cooling, leading to a simple relation between effective temperature and age of the white dwarf, described approximately by Mestel theory (Mestel 1952; Van Horn 1971).

Known white dwarfs at  $T_{eff} \sim 4500$  K are among the oldest stars in the solar neighborhood, and they serve as reliable chronometers. The exponential decrease in their cooling rate should cause a pile up of white dwarfs at lower temperatures, if we assume the star formation rate to be constant. The volume density of white dwarfs per unit absolute bolometric magnitude plotted as a function of their luminosity, i.e. the luminosity function, is expected to show more and more white dwarfs in lower temperature bins. However, the best current observational determinations of the white dwarf luminosity function for the disk indicate a turn-down in the space density of low luminosity stars (Liebert, Dahn & Monet 1988; Oswalt et al. 1996; Leggett, Ruiz & Bergeron 1998), interpreted to be a signature of the finite age of the disk; the luminosity where this turn-down occurs, in conjunction with theoretical cooling calculations, allowed Winget et al. (1987) to estimate the age of the Galactic disk.

## 1.2 White dwarf variables: the inside story

Landolt (1968) accidentally discovered the first variable white dwarf, HL Tau 76, while attempting to gather data on white dwarf standards. Subsequently, McGraw, Robinson, Lasker, and Hesser searched systematically for other variables; this led to the discovery of the first significant sample of what came to be known as the class of DA variables (DAVs; Lasker & Hesser 1971; McGraw & Robinson 1975, 1976; McGraw 1976; Hesser, Lasker, & Neupert 1976; Robinson et al. 1978). Nather (1978) was the first to distinguish these pulsating DA white dwarfs from cataclysmic variables. R 548 (ZZ Ceti) was the first white dwarf to be deciphered (Robinson, Nather, & McGraw 1976), and the DAVs were later called the ZZ Ceti stars (McGraw 1980), as the proto-type R 548.

Pioneering efforts by McGraw (1979) and Greenstein (1982) established the location of the ZZ Ceti instability strip in temperature. Greenstein (1982) found ZZ Ceti stars in the range 10700–11700 K, on an extension of the Cepheid instability strip. However, the observed pulsation periods were two orders of magnitude longer than predicted for radial pulsations in white dwarf stars. Hence, Warner & Robinson (1972) and Chanmugam (1972) suggested that the observed pulsations were nonradial g-modes. However, Brickhill (1975) found the lowest order modes of non-radial adiabatic oscillations in his models, at the same temperatures as HL Tau 76 and G 44-32, to be smaller than the observed periods by a factor of two. Dolez & Vauclair (1981) initially suggested that DAs with a thin hydrogen layer ( $M_H/M < 1.5 \times 10^{-14}$ ) were pulsationally unstable in the range 11500–13500 K due to the  $\kappa$  mechanism in the helium partial ionization zone. They also suggested that DAs with a thicker hydrogen layer ( $M_H/M > 1.5 \times 10^{-14}$ ) pulsate between  $\sim 10000$  K and 11500 K, and in this case the  $\kappa$  mechanism in the hydrogen partial ionization zone was driving the pulsations. Dziembowski (1977), Keeley (1979), and Dziembowski & Koester (1981)

also found nonradial g-mode instabilities in their white dwarf models, driven by the  $\text{He}^+$  ionization zone.

Winget et al. (1982a) carried out non-adiabatic calculations for a large grid of stratified, evolutionary white dwarf models and found ZZ Ceti pulsations to be a result of hydrogen driving. Their models were pulsationally unstable for a wide range of H layer masses. Winget et al. (1982a) also claimed to find a second instability strip at  $T_{\text{eff}} = 19000\text{K}$  in their ZZ Ceti models with thin hydrogen layers ( $M_{\text{H}}/M_{\star} < 10^{-10}$ ) due to He driving. They suggested that He driving may also produce DB variables at  $T_{\text{eff}} \sim 19000\text{K}$ . The first DB variable (DBV) was discovered soon after (Winget et al. 1982b), and there are now 13 DBVs known to date (see Bradley 1998, 2000; Nitta et al. 2004). There are comparatively 74 DAVs in the literature, including the new DA variables listed in this document.

Apart from the DAV and DBV instability strips, there exist 15 other hot white dwarf variables. These are called the DO variables (DOVs, GW Vir stars) and the planetary nebula nuclei variables (PNNVs), found in an effective temperature range of 80000 to 170000 K with  $\log g \approx 6$ . McGraw et al. (1979a, 1979b) discovered the first hot white dwarf variable in this class, PG 1159-035. This hot instability strip is not well defined in temperature; it is not clear whether these pulsators belong to a single strip or are indicating the presence of two distinct hot instability strips.

### **1.2.1 Short term seismology: structural constraints**

The purity of the instability strip led to the conclusion that pulsations are an evolutionary effect in otherwise normal white dwarfs (Robinson 1979; Fontaine et al. 1985; Fontaine et al. 2001, 2003; Bergeron et al. 2004). Hence, we conclude that there is nothing unusual or unique about pulsating white dwarfs and

we can apply what we learn from them to white dwarfs at different temperatures. Each pulsation mode is an independent constraint on the structure of the star; the more modes we detect, the better our understanding of the stellar structure. Using an ensemble of modes gathered from different pulsators, we can draw general characteristics of white dwarf stars. This technique is beneficial to decipher pulsators that show only a few modes, such as the typical hDAVs.

Each of the eigenmodes that can be excited in the star is described by a set of indices:  $k$  is the radial quantum number that gives the number of nodes between the surface and the center of the star,  $\ell$  is the azimuthal quantum number that gives the number of nodes on the surface, and  $m$  is the number of nodes along the meridian; it is used to describe the frequency if the spherical symmetry is lost due to rotation or a magnetic field. We use spherical harmonics ( $Y^\ell_m$ ) to describe these eigenmodes. This is a manifestation of the spherical gravitational potential, and is similar to the quantum numbers used to describe the state of an electron bound by the spherical electrostatic potential of the nucleus. The radial quantization results from boundary conditions that dictate an anti-node at the surface and a node at the center of the star in our models. The azimuthal quantization results from surface boundary conditions; nodes and anti-nodes along the surface have to add up to the circumference of the star. See the review by Winget (1998) for a detailed discussion.

White dwarfs exhibit nonradial pulsations; this is easily understood when we consider that to pulsate radially, the star must expand and contract against gravity ( $\log g \sim 8$ ), requiring a substantial amount of energy. Comparatively, it is much easier for the star to pulsate nonradially. All variable stars are expected to have larger pulsation amplitudes at the surface compared to the core due to the density profile. White dwarfs are not as centrally condensed as some

other classes of variables, and hence the observed nonradial modes sample their interiors better (Montgomery & Winget 1999; Montgomery, Metcalfe, & Winget 2003). Their high densities and temperatures make these stars good cosmic laboratories to study fundamental physics under extreme conditions.

### 1.2.2 Long term seismology: drifting pulsation periods

There are two competing internal evolutionary processes that govern the change in pulsation period with time ( $dP/dt = \dot{P}$ ) for a single mode in the models of white dwarf variables. Winget, Hansen, & Van Horn (1983) found that cooling increased the periods in their models as a result of the increasing degeneracy, and residual gravitational contraction decreased the periods in their models. For white dwarfs with high effective temperatures, contraction is still significant. The DOV star PG1159-035 revealed a drift rate of  $(13.0 \pm 2.6) \times 10^{-11}$  s/s for its main periodicity at 516 s (Costa, Kepler, & Winget 1999). This value of  $\dot{P}$  agrees in sign with the theoretical models, but is an order of magnitude larger. Such a reliable drift rate has not yet been measured for the DBV white dwarfs. The unidirectional drift rate of the ZZ Ceti stars close to the blue edge has been constrained to be smaller than a few  $\times 10^{-15}$  s/s (O'Donoghue & Warner 1987; Kepler et al. 2000a; Mukadam et al. 2003a).

These drift rate measurements rely on the precision with which we can measure the arrival times of pulses from the stellar clock. Such a determination relies on the accuracy of instrument timing (see section 2.2.3), and the precision with which we can measure the pulsation period. Measuring the period with sufficient accuracy to begin measuring the drift rate of a clock can greatly benefit from initial multi-site observations to distinguish between the true frequencies and aliases, and subsequent single-site observations to increase the baseline (refer to section 2.4 for more details). Constraining the evolution of these clocks

is not a simple task.

We theoretically expect DAV evolution to be simple cooling at a nearly constant radius, and the measured drift rates are consistent with cooling rates in our models. However, different modes in the same star show drift rates different by a factor of 10 or more. Hence, we cannot be certain that the drift rate we have measured reflects cooling (see section 5.2.3).

### **1.3 Motivation: why search for DAVs?**

Since 80% of all white dwarf stars have atmospheres dominated by hydrogen (DAs; Fleming, Liebert, & Green 1986), to understand the DA variables (DAVs) is to understand the most common type of white dwarf. The ZZ Ceti pulsation periods range from  $\sim 100$ – $1200$  s and are consistent with nonradial g-mode pulsations. The pulsation periods and amplitudes of the DAV stars show a distinct trend with temperature (see Clemens 1993). The hot DAVs (hDAVs) in the hotter half of the instability strip show relatively few pulsation modes, with low amplitudes ( $\sim 0.1$ – $3\%$ ) and periods around  $100$ – $300$  s. The cooler DAVs (cDAVs) show longer periods, around  $600$ – $1000$  s, larger amplitudes (up to  $30\%$ ) and greater amplitude variability (e.g. Pfeiffer et al. 1996; Kleinman et al. 1998). This well-established period-temperature and amplitude-temperature correlation (see section 5.2 for the theory) allows us to classify DAV stars meaningfully into hot DAVs (hDAVs) and cool DAVs (cDAVs).

Understanding the structure and evolution of a statistically significant sample of DAVs has implications for other areas of astronomy, some of which are discussed below.

### 1.3.1 Stellar structure

We can probe stellar structure and composition by finding a single star rich in pulsation modes, and/or by finding a large number of pulsators to use the method of ensemble asteroseismology. A unique model fit to the observed periods can lead us to a determination of the stellar mass, core composition, age, rotation rate, magnetic field strength, and distances using asteroseismology. Apart from our search, there are 38 DAVs in the literature (see Bergeron et al. 2004 and Warner & Woudt 2003); additional pulsators and additional modes will help us understand the DAVs as a class. Measuring the rotation period for DAVs and comparing it with other classes of white dwarf pulsators at different temperatures can give us clues about the evolution of angular momentum.

Even though the mass distribution is centered around  $0.6 M_{\odot}$ , we find a small fraction of higher mass white dwarfs. BPM 37093 is a known  $M_{\odot}$  pulsator (Kanaan et al. 1992). Therefore, a search for a large number of DAVs is bound to yield extreme mass pulsators. Low mass ( $\log g \leq 7.6$ ) DAVs could well be helium core white dwarfs; pulsating He core white dwarfs should allow us to probe their equation of state. We expect that these stars originate from interacting binaries, as the Galaxy is too young for single star evolution to result in white dwarfs of  $\leq 0.5 M_{\odot}$ . High mass ( $\log g \geq 8.5$ ) DAVs are potentially crystallized, paving the way for an empirical test of the theory of crystallization in stellar plasma (Winget et al. 1997; see section 1.3.3 for a detailed discussion). This should also have implications for models of neutron stars and pulsars, which are thought to have crystalline crusts.

### 1.3.2 Stable clocks can be used to find planets

The dominant modes (probably  $\ell = 1, k = 2$ ) in hDAVs like G 117-B15A, R 548 (ZZ Ceti), and L19-2 have been found to exhibit extreme amplitude and fre-

quency stability ( $\dot{P} \sim 10^{-15}$  s/s), implying that these stars can serve as reliable clocks. To put this number in perspective, these clocks are expected to lose or gain one cycle in a few billion years. Should such stable clocks have an orbiting planet around them, their reflex motion around the center of mass of the system would become measurable, providing a means of detecting the planet (e.g. Kepler et al. 1991; Mukadam, Winget, & Kepler 2001; Winget et al. 2003). These hDAVs were once main sequence stars, suitable hosts for planet formation. Theoretical work indicates outer terrestrial planets and gas giants will survive the red giant phase (e.g. Vassiliadis & Wood 1993) with orbits stable on timescales longer than a fraction of a billion years (Duncan & Lissauer 1998). These timescales are comparable to the cooling time required by a newly formed white dwarf to reach the pulsational DAV strip. The success of a planet search around these stable clocks rests on finding a statistically significant number of hDAV stars.

### 1.3.3 DAV seismology helps cosmochronometry

White dwarfs at  $T_{eff} \sim 4500$  K are among the oldest stars in the solar neighborhood; an average white dwarf may take up to several billion years to cool to 4500 K. We can use these chronometers to determine the ages of the Galactic disk and halo (e.g. Winget et al. 1987; Hansen et al. 2002). Renzini et al. (1996) and Zoccali et al. (2001) have also used this method to determine the ages of the globular clusters NGC 6752 and 47 Tucanae (NGC 104) respectively. While von Hippel & Gilmore (2000) and Kalirai et al. (2001) utilized this method to determine the ages of the open clusters NGC 2420 and NGC 2099 (M37) respectively. This method, known as white dwarf cosmochronometry, has a different source of uncertainties and model assumptions than main sequence stellar evolution. This is because white dwarfs spend most of their time on the cooling sequence.

A significant part of the theoretical uncertainty in the age estimation of white dwarfs comes from uncalibrated model cooling rates and uncertainties in the constitutive physics and basic parameters such as compositional stratification, crystallization, and phase separation, used in calculating the cooling rates. The outer non-degenerate layers and the core composition play an important role in dictating the cooling rates. Although these cool white dwarfs ( $T_{eff} \sim 4500$  K) have not been observed to pulsate (Nitta et al. 2000a), we can still use asteroseismology to calibrate theoretical cooling curves, thus reducing the uncertainties in determining white dwarf ages.

### **Massive pulsators help us study crystallization**

As a white dwarf star cools, theory suggests that the thermal energy of the ions becomes much smaller than the energy of the Coulomb interaction, and the interior of the white dwarf should begin to crystallize (Abrikosov 1960; Kirzhnits 1960; Salpeter 1961). The model equation of state for matter, i.e. electrons and nuclei, at zero temperature and very large densities revealed that the nuclei form a lattice rather than a gas. For a  $0.6 M_{\odot}$  model, the onset of crystallization begins at  $T_{eff} = 6000$  K for a C core, and at  $T_{eff} = 7200$  K for an O core (Wood 1992). Crystallization affects the cooling rate of the white dwarf by releasing latent heat, and the outward moving crystallization front causes the periods to increase. In a 99% crystallized star, pulsation periods can increase over an evolutionary timescale by as much as 30% or more. Pulsation modes get excluded from the crystallized region, as the crystallization front represents a hard boundary.

Van Horn (1968) first showed that as the star crystallizes it releases latent heat, affecting the cooling times by adding an additional energy source. In addition, theoretical calculations suggest that it does not freeze completely as an

alloy, some phase separation occurs between the C and O; this enhances the oxygen content in the crystallized region, while the overlying fluid layer becomes carbon enhanced (Stevenson 1980; Segretain & Chabrier 1993; Montgomery et al. 1999; Isern et al. 2000). The phase separation is an additional energy source, as it releases gravitational binding energy from the star.

Crystallizing temperatures for most white dwarfs are much cooler than the DAV instability strip from 11 000-12 500 K, implying that ordinarily effects such as crystallization and phase separation cannot be studied with asteroseismology. However, because of the larger central pressures in massive pulsators ( $\log g \geq 8.6$ ), they should be substantially crystallized even at 12 000 K (Winget et al. 1997; Montgomery & Winget 1999). These variables can provide the first test of the theory of crystallization in stellar plasma. Metcalfe, Montgomery, & Kanaan (2004) present strong asteroseismological evidence that the massive DAV, BPM 37093, is 90% crystallized.

### **Stable pulsators provide a calibration of white dwarf cooling curves**

Kepler et al. (2000a) conclude that the rate of cooling dominates the drift rate ( $\dot{P}$ ) for the hDAV stars; the rate of contraction ( $\dot{R}$ ) of a model DAV with a radius of  $9.6 \times 10^8$  cm is negligible  $\sim 1$  cm/yr. Cooling rates for a large sample of hDAVs with different masses and internal compositions will prove fruitful in calibrating the DA white dwarf cooling curves. Note that a stable clock with an orbiting companion will show both the parabolic cooling and the periodic variations due to the companion (see Kepler et al. 1991; Mukadam, Winget, & Kepler 2001); these effects are discernible and will most likely have different timescales.

We expect that a change in the gravitational constant ( $G$ ) should alter the radius of the white dwarf, thus changing its rate of cooling. The observed drift rates of white dwarfs like G 117-B15A, R 548, and L 19-2 place a constraint on the

rate of change of  $G$  with time (Benvenuto, García-Berro, & Isern 2004). Should the cooling rate alter as a consequence of a change in  $G$ , we should also be able to discern its effects in the white dwarf luminosity function. The observed white dwarf luminosity function also places an independent upper limit on the rate of change of  $G$  (Isern, Garcia-Berro, & Salaris 2002).

### **H & He layer masses from seismology help improve models**

Lack of knowledge of mass loss and details of thermal pulses lead to uncertainties in the H and He layer masses. The outer non-degenerate layers control the rate at which the residual thermal energy of the core is radiated into space. Poorly determined hydrogen and more importantly, helium mass fractions increase the uncertainty of white dwarf ages by  $\sim 0.75$  Gyr for an order of magnitude change in the He layer mass (Wood 1990, 1992). Although we can utilize pulsating white dwarfs to measure cooling rates directly, we can do so only in selected temperature ranges where pulsations occur because of the development of partial ionization zones. Hence, determining hydrogen and helium layer masses from asteroseismology will be helpful in improving evolutionary models and better determining white dwarf ages.

#### **1.3.4 Seismological distances from a flickering candle**

Obtaining a unique model fit to the pulsation modes allows us to determine an asteroseismological distance by matching the observed luminosity of the star with the model luminosity. Typically, the asteroseismological distance is more accurate than what we determine from measured parallax (e.g. Bradley & Winget 1994a; Bradley 2001). This also holds true for other kinds of pulsating stars, such as delta Scuti variables (e.g. Peterson & Hog 1998) and Cepheids (e.g. Kervella et al. 2004). Variable white dwarfs with a rich pulsation spec-

trum should therefore be of great interest for an independent calibration of the Galactic distance scale.

Alternatively, Salaris et al. (2001) derived distances to globular clusters by fitting a local template DA white dwarf sequence with accurate parallax measurements, and with  $T_{\text{eff}}$  between 10000K and 20000K, to the de-reddened cluster counterpart. The vertical shift applied to the local template sequence to fit the cluster sequence provides a measure of the distance to the cluster. This white dwarf fitting technique assumes that the average mass of the white dwarfs in the cluster is the same as the average mass of white dwarfs in the local DA template sequence. Uncertainties in this technique can be reduced via asteroseismology by measuring stellar masses and hydrogen layer thicknesses for DA pulsators and extending the results systematically to other DAs.

## 1.4 My dissertation

Having established the importance of finding additional ZZ Ceti stars, we realized that most of the nearby bright DAVs had already been discovered. (For example, Kepler et al. (1995) searched for DAVs among the brighter candidates and found many non-variables.) Finding a significant number of new DAVs required observing newer candidates at fainter magnitudes. The 3-channel photometer in our possession (Kleinman, Nather, & Phillips 1996), based on photomultiplier tubes (PMTs), allowed us to obtain usable photometry on objects of magnitude  $\leq 17$  at the 2.1 m telescope at McDonald Observatory. This necessitated the building of an efficient time-series photometer that would allow us to observe fainter stars ( $B \leq 19$ ), enabling us to reach white dwarfs in a larger volume. The number density of DA white dwarfs brighter than  $g = 17.0$  per square degree is  $\sim 0.2$ , while the density of DA white dwarfs brighter than  $g = 19.0$  per square degree is  $\sim 2$  (Fan 1999).

Assisting Dr. R. E. Nather in building Argos, an ideal time-series photometer, for the 2.1 m telescope at McDonald Observatory, constituted the first part of my thesis. Carrying out the search to discover a statistically significant number of DAVs was the second step towards my project. Characterizing the shape and mass dependence (or lack of) of the instability strip was the third part of my thesis. Lastly, I hope to use the increased population of new DAVs towards ensemble seismology. Although this part of the thesis remains a work in progress, it certainly establishes the preliminary steps in the direction.

#### **1.4.1 Establishing the ZZ Ceti instability strip**

Pulsation models indicate that the limits of the ZZ Ceti instability strip depend on the effective temperature and mass of the star (Bradley & Winget 1994b). This was observationally confirmed by Giovannini et al. (1998) and Bergeron et al. (2004). Most model atmospheres of DAV stars treat convection with a mixing length prescription, assuming some parameterization, the choice of which can shift the edges of the instability strip in temperature by a few thousand Kelvin (Bergeron et al. 1995; Koester & Allard 2000). Determining the location of the red edge in theoretical models is difficult due to convective and nonlinear effects (Winget et al. 1982a; Brickhill 1983; Bradley & Winget 1994b; Wu & Goldreich 1999, 2001). Kanaan et al. (2000a) and Kanaan, Kepler, & Winget (2002) find the observed red edge for the ZZ Ceti instability strip at 11 000 K. They conclude it is not an observational selection effect because their noise level was 50 times smaller than the expected amplitude at the red edge. Even  $\ell=3$  modes should be detectable at that S/N ratio. Finding more DAVs at different temperatures and masses will improve our observational determination of the edges of the ZZ Ceti strip, as well as determine its mass dependence.

### 1.4.2 Ensemble seismology of the ZZ Ceti stars

The almost isothermal cores of these stars constitute 99.99% of the star by mass. White dwarf stars with masses in the range  $0.55\text{--}1.1 M_{\odot}$  comprise chiefly of carbon and oxygen (Iben 1990); the ratio of carbon to oxygen is determined during the main sequence lifetime by the astrophysically important, but experimentally uncertain,  $^{12}\text{C}(\alpha, \gamma)^{16}\text{O}$  nuclear reaction rates (Metcalfé, Winget, & Charbonneau 2001; Metcalfé, Salaris, & Winget 2002; Metcalfé 2003). Hence, we theoretically expect white dwarf cores to be similar; pulsation modes that probe the core better than others are expected to show a signature of this similarity.

The ZZ Ceti stars are musical instruments, capable of ringing in thousands of modes. Ensemble seismology can use all the observed pulsation periods in all the similar ZZ Ceti stars to unravel their stellar structure.

## Chapter 2

# Ideal time-series photometer

### 2.1 Time-series photometry and ideal instrumentation

To study phenomena variable at short timescales, we use a special technique called relative time-series photometry or high-speed differential photometry. There is more to time-series photometry than meets the eye; it is not just relative photometry with a precise measurement of the observation epoch.

A good time series photometer not only requires a precise measurement of the start time of an exposure, but also the duration of the exposure. Elements that cause a jitter in these measurements are undesirable. These include, but are not limited to, an undisciplined or drifting clock used for timing, a mechanical shutter, and an unregulated time-share data acquisition system.

Besides accuracy in timing, a good time-series photometer must be able to provide sufficient time resolution to sample the variable phenomena well. For example, to study the hot ZZ Ceti stars that exhibit pulsation periods in the range 100–300 s, we need a suitable time resolution of 5–10 s. This not only requires that the photometer should allow a short exposure time, but that it also allows an insignificant dead time between consecutive exposures. Frame

transfer CCDs are ideal for time-series photometry as they can provide contiguous exposures with no dead time. Photometers with a chip readout time above  $\sim 10$  s are incapable of good time-series photometry, even if they allow a 1 s exposure time. Figure 2.1 shows the light curve of a pulsating white dwarf acquired using the low resolution spectrograph (LRS) in imaging mode on the 9.2 m Hobby-Eberly Telescope at McDonald Observatory (top panel). The bottom panel shows observations of the same star using Argos (see section 2.2) on the 2.1 m Otto Struve telescope. The data from the 9.2 m telescope exhibits uncertainties in period and phase larger by a factor of 1.5 than the 2.1 m data in the lower panel. q.e.d.

Multi-site observations make it easier to distinguish between the true frequencies and aliases in our data<sup>1</sup>. The Sun never rises on instruments like the Whole Earth Telescope (WET; Nather et al. 1990) used for the study of variable white dwarfs; WET comprises a collaboration of observatories around the globe. Increasing the precision of our frequency measurements of these pulsators requires data over a long timespan with accurate timing, acquired ideally from multiple sites with suitable time-series photometers.

Each detected mode provides an independent constraint on the stellar structure, so maximizing the number of observed modes is essential for identifying a unique model-fit to the data. High instrument detection efficiency, larger apertures, and smaller number of reflections will allow us to observe modes of small amplitude ( $\sim 0.1\%$ ), increasing the number of known modes for the star.

---

<sup>1</sup>The Fourier Transform (FT) of a sine curve of finite length shows aliases of amplitude comparable to, but smaller than, the amplitude of the true frequency. For noise-free data, this is mathematically expressed as the function  $\sin(x)/x$ .

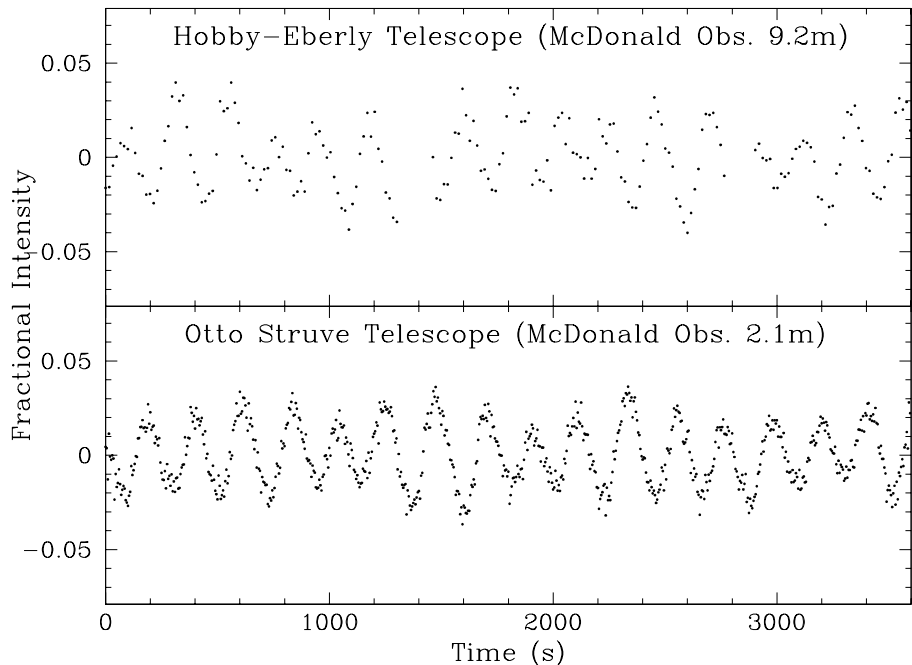


Figure 2.1: The top panel shows the light curve of a stable DAV G117-B15A ( $B=15.5$ ) acquired with the Hobby-Eberly Telescope at McDonald Observatory (effective aperture 9.2 m), using the low resolution spectrograph in imaging mode. The bottom panel shows a light curve of the same star obtained using the 2.1 m Otto Struve telescope also at McDonald Observatory. In the second case, the data was acquired with an efficient instrument idealized for high speed time-series photometry, a prime focus frame transfer CCD camera with the only optical surfaces between the star and the CCD being the primary mirror, a BG40 filter, and the glass window enclosing the vacuum around the CCD chip.

## 2.2 Argos: designed for time-series photometry

R. E. Nather has designed a prime focus CCD photometer, optimized for high speed time-series measurements of oscillating white dwarf stars (Nather and Mukadam 2004), which he has named Argos. I have assisted Ed in making the instrument operational, and in the subsequent testing phase. After light reflects from the primary mirror, it focuses directly onto the small CCD chip without any intervening optics; lack of multiple reflections makes the instrument highly efficient. The combination of an efficient instrument and a large amount of telescope time ( $\approx 100$  nights/yr) at the 2.1 m telescope has given me a unique opportunity to search for many pulsators. Note that this chapter is not meant to be a stand-alone description of Argos, but supposed to complement the publication by Nather & Mukadam (2004).

### 2.2.1 The CCD camera

Argos is based on a commercial CCD camera made by Roper Scientific, the Princeton Micromax 512 BFT NTE-CCD camera <sup>2</sup>. Its specifications are shown in Table 2.1.

We acquire an image scale of 3.05 pixels per arcsecond (F/3.9) for our  $512 \times 512$  pixel CCD chip, and a field of view of 2.8 arcmin on a side. Frame transfer, initiated by pulses from a GPS system, allows us to obtain contiguous exposures as short as 1 s. The CCD is back-illuminated for improved blue sensitivity and provides a quantum efficiency of 80% in the wavelength range 4500–6500 Å. With thermoelectric cooling, we maintain the chip at a temperature of  $-45^\circ\text{C}$ , and obtain a dark current of 1–2 ADU/s/pixel. The readout time for the entire chip with no binning is 0.28 s; the readout noise is less than 8 electrons RMS.

---

<sup>2</sup><http://www.roperscientific.com/micromax.html>

Figure 2.2: Wavelength Response: The top panel shows the response of the Argos CCD chip convolved with atmospheric extinction. The middle panel shows the modified response, if we include a blue bandpass filter to reduce sky brightness and increase the measured pulsation amplitude of our hot pulsating white dwarfs. The lower panel shows the wavelength response of a PMT, a detector we used before Argos. The improvement in sensitivity is a factor of 9, as measured on the same telescope.

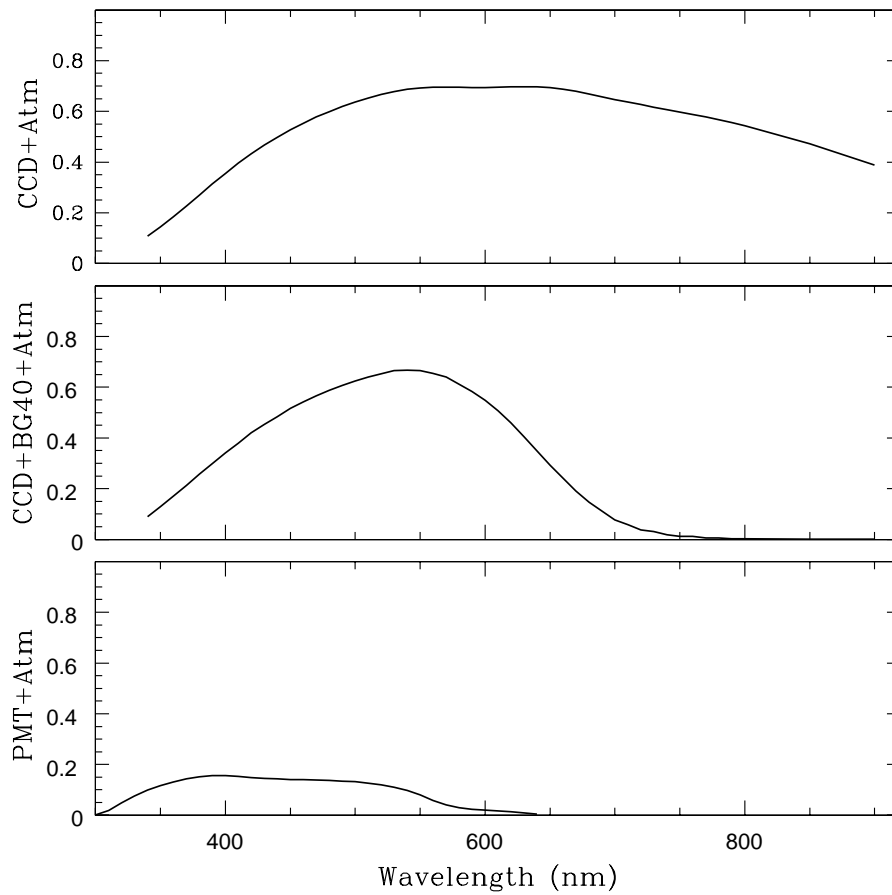


Table 2.1: Summary of Camera Specifications

Pixel size:	$13\mu \times 13\mu$
Pixel array size:	512×512, back illuminated
On-chip storage:	512×512, frame transfer operation
Frame transfer time:	310 $\mu$ s
Readout rate:	1 MHz, 16 bit A/D conversion
Readout time:	0.28 s, full frame with no binning
Cooling:	Thermoelectric + fan air exhaust
Chip temperature:	-45 C
Measured Read noise:	4 electrons RMS
Gain	2 electrons/ADU
Dark noise:	1-2 ADU/s/pixel
Optical coating:	broadband anti-reflection
Quantum Efficiency:	30% at 3500A, 80% 4500-6500A, 40% at 9000A
Linearity:	$\sim$ 1% below 40,000 ADU (saturation at 65,000 ADU)

### 2.2.2 Wavelength response

We show the wavelength response of the CCD chip in the top panel of Figure 2.2, taking atmospheric extinction into account. Our chief interest lies in blue pulsating DA white dwarfs, whose pulsation amplitudes are a function of wavelength (Robinson et al. 1995; Nitta et al. 1998, 2000b). Including photons redward of the PMT cutoff (ca. 650 nm), which are less modulated by the pulsation process, reduces the measured amplitude (Kanaan et al. 2000b). We find that the pulsation amplitudes for our instrument, with and without a blue bandpass filter (Schott BG40 1 mm), are different by as much as 35–42% (see Figure 2.3). A blue bandpass filter is traditionally used to measure amplitudes comparable to blue-sensitive detectors like PMTs with bi-alkali photocathodes (see Kanaan et al. 2000b), that have been used to observe variable stars since the late sixties.

Filterless observations of the ZZ Ceti star G 117-B15A yield an amplitude of 12.6 mma for the 215 s period, shown in the top panel of Figure 2.3. We measure noise in the FT to be 0.43 mma, average amplitude in the high frequency

region devoid of pulsations. This gives us a S/N ratio of 29.3 from an hour long filterless observing run on G 117-B15A ( $B=15.5$ ) with Argos. Observing the same star for an hour with the BG40 filter gives us an amplitude of 21.8 mma and a noise level of 0.7 mma, measured in the same way as before. This yields a S/N ratio of 31.1, marginally better than filterless observations. However, this may not hold true for the same star in cloudy weather (also see Figure 2.4 and related discussions).

We show the response of our instrument including a 1 mm BG40 Schott glass filter in the middle panel of Figure 2.2. Although the pulsation amplitude increases due to a blue bandpass filter, the middle panel indicates the loss of photons, which is close to a factor of two for hot white dwarfs, and a factor of six or so for cooler red stars in the field. We find an increase in measurement noise in the light curves of the target and comparison stars due to photon losses with the BG40 filter. To use a blue bandpass filter or not, is a decision that must be made individually for each pulsator, depending upon its magnitude and pulsation amplitude, as well as the number and relative magnitudes of the comparison stars to the target pulsator.

A bright pulsator, surrounded only by a couple of relatively fainter comparison stars in the field, will benefit if the blue filter is not used while observing. This is shown by the light curves of WD1345-0055 ( $g=16.7$ ) in Figure 2.4. With the filter, we obtain an average noise of 1.0 mma, and 0.7 mma without. This translates into a S/N ratio of 10.4 with the BG40 filter, and 12.4 without the filter. Excluding the BG40 filter for stars like WD1345-0055 yields a better S/N ratio.

We are unable to demonstrate the case for a faint pulsator in a similar manner; we did not find a faint pulsator where the dominant mode is a singlet with a stable amplitude, ideal for the test. If there is any amplitude modula-

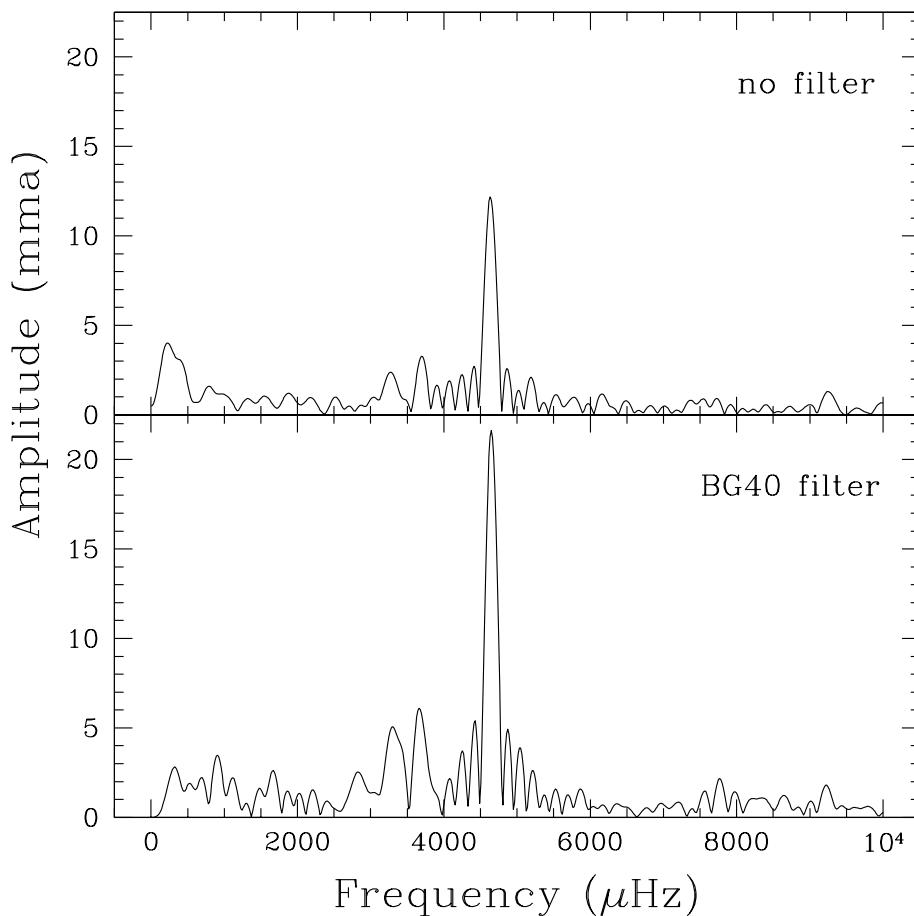


Figure 2.3: The top panel shows an hour of filterless observations of the optical clock, G 117-B15A, where the dominant mode has an amplitude of 12.6 mma. We acquired the data using Argos at the prime focus of the 2.1 m telescope at McDonald Observatory. The lower panel shows a Fourier Transform also based on one hour of data acquired with the same instrument using a BG40 filter. The dominant mode shows an amplitude of 21.8 mma with the filter, a difference in amplitude of 42%. This difference is also evident in the other modes. We compute a S/N ratio of 29 without the filter and 31 with the BG40 filter, marginally better.

tion, then the signal to noise ratio that we measure in our light curves changes correspondingly, and this change in S/N is not related to our detection system. We also do not have a good season of observations with and without a filter on any of the stars that show multiplet structure. It is our conjecture that using a filter will be helpful in observing faint stars with low pulsation amplitudes, surrounded by multiple bright comparison stars. But it remains to be tested.

Observers should carefully think about their decision to use a blue band-pass filter or not, individually for each pulsator. The factors to consider are the loss of pulsation amplitude by 35–42% without the filter, the loss of photons for the white dwarf pulsator by a factor of two with the filter, and the loss of photons for each comparison star by a factor of six with the filter. A simple S/N calculation for each variable should help the observer in making an informed decision.

The bottom panel of the Figure 2.2 shows a PMT (Photo Multiplier Tube, R 647 Hamamatsu) wavelength response for comparison, convolved with atmospheric extinction. We used a PMT photometer, called P3Mudgee, on the same telescope to gather data on pulsating white dwarfs before Argos (see Kleinman, Nather, & Phillips 1996 and Nather & Warner 1971). Argos is nine times more sensitive than P3Mudgee; we now obtain usable time-series photometry on objects of apparent magnitude 19, where the limit with P3Mudgee on the same telescope was  $B \sim 17$ . The faintest known white dwarf pulsator to date, WD0947+0155, of apparent magnitude  $g=20$  has been discovered with Argos.

### 2.2.3 Instrument timing

A time-series photometer must know precisely when an exposure is started, and precisely how long it took. The Argos timing system is based on a GPS clock<sup>3</sup>

---

<sup>3</sup><http://www.trimble.com/thunderbolt.html>

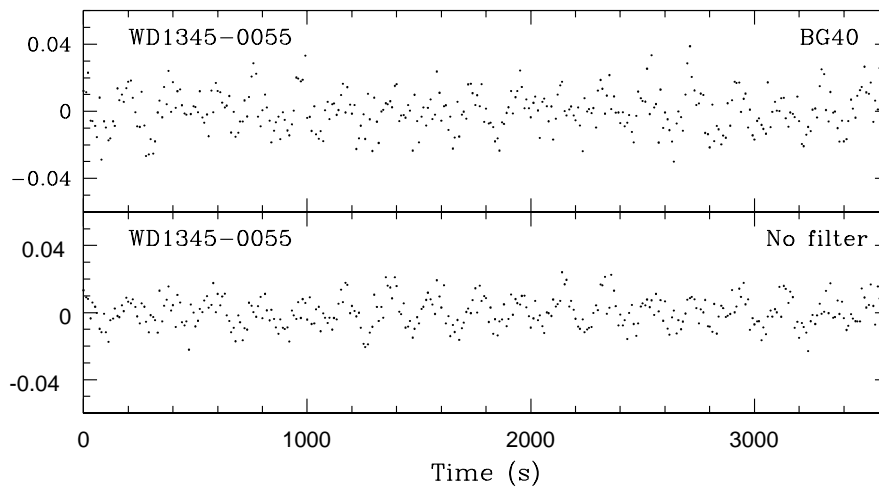


Figure 2.4: We show the reduced light curves of WD1345-0055 ( $g=16.7$ ) with and without a BG40 filter. We find an improved S/N ratio after excluding the BG40 filter, inspite of the reduction in signal by as much as 35-42%.

designed primarily for precision timekeeping. An antenna ensures that the clock remains synchronized with the GPS satellites. The claimed uncertainty for the GPS pulse is about 50 ns, considerably more precise than we need.

We have assembled a simple timer card that plugs into the parallel port of the data acquisition computer. The timer card comprises a count-down register that accepts 1 Hz pulses from the GPS clock. When the user sets the exposure time in the acquisition program in the allowed range of 1–30 s, the register counts down from the integral exposure value and sends an output pulse to the CCD camera at the end of the exposure. The positive edge of the output pulse triggers a frame transfer in the CCD chip. The exposure intervals are thus contiguous, and determined directly from the clocking hardware. The jitter in the timing for this operation is hard to measure, but we certainly expect it is  $\leq 100 \mu\text{s}$ .

Mechanical shutters introduce a timing jitter, which is not desirable in a good time-series photometer. They also cause non-uniform illumination of the field and introduce a source of correlated noise in the light curve. Coherence of the pulsations over long timescales allows us to gain over random noise with time, but it is harder to eliminate non-Gaussian sources of noise. Besides, mechanical shutters have a lifetime of order a million cycles; at 5 s exposures we would have to replace the shutter every ten months of observing, if we assume observing 15 days every month with 10 hr observations every night.

#### **2.2.4 The prime focus mount**

The Argos camera is shown on its prime focus mount in Figure 2.5, at the end of the 2.1 m telescope. A smaller CCD camera (Cyclops) with a wide angle field of view ( $150^\circ$ ) is attached to the Argos camera to capture regular images of the dome slit. The dome of the 2.1 m telescope does not track, and hence the images

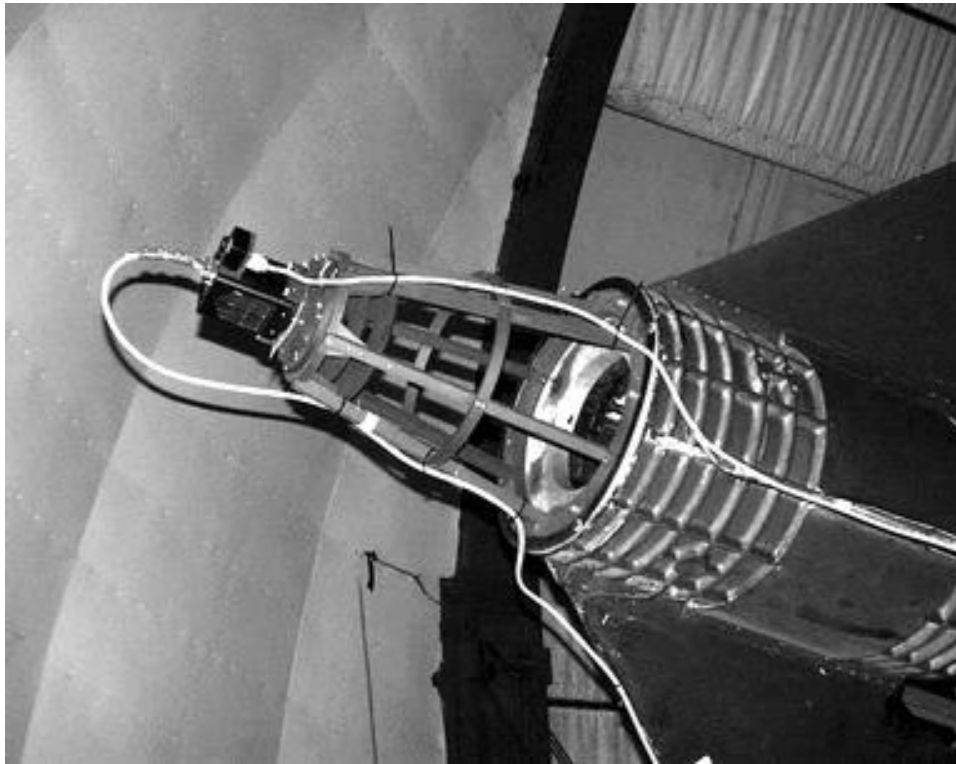


Figure 2.5: We show the CCD photometer Argos on its prime focus mount at the 2.1 m telescope at McDonald Observatory. Attached to Argos is a smaller camera that captures images of the dome slit. These images allow the user to track the slit manually from the control room.

prove useful to the observer in deciding when to move the dome.

Design considerations for the prime focus mount necessitate that the optic axis pass through the center of the  $6\text{ mm} \times 6\text{ mm}$  CCD chip, while the plane of the chip remains perpendicular to the optic axis. Since we cannot rely on machining precision alone to center the optic axis on the chip, we mount the camera on a metal plate that can move by half an inch in two orthogonal directions using x-y adjustment screws. These x-y axes align with the rows and columns of the CCD chip. The tip/tilt of the camera can be controlled by a push-pull arrangement of screws, to orient the CCD chip perpendicular to the optic

axis.

The two-step alignment procedure involves centering the optic axis on the chip, and then adjusting the plane of the CCD chip till it is perpendicular to the optic axis. For the first step, we point to a bright star of fourth or fifth apparent magnitude, and defocus the telescope to get a donut-shaped stellar image. Non-uniform illumination of the donut breaks the circular symmetry and points in the direction of the optic axis. By moving the telescope, we place the donut-shaped image in different parts of the chip. Analyzing the images so obtained, we get an idea of the location of the optic axis on the chip. If it is not located at the center of the chip, we use the x-y alignment to move the camera relative to the optic axis. By successive iterations, we are able to align the optic axis to within the central fifth of the chip ( $\pm 50$  pixels). This level of precision is sufficient for a small CCD chip such as ours. When properly aligned, the corners of the chip are 2 arcmin from the optical axis, where aberration from coma due to the parabolic primary mirror is calculated to expand a point image to about 1 arcsecond in diameter. We rarely experience sub-arcsecond seeing at the McDonald Observatory site, so we have not been able to verify this calculation.

Argos mounts on the focus assembly of the 2.1 m telescope, and the entire photometer moves along the optic axis when we focus the telescope. In order to check if the plane of the CCD is perpendicular to the optic axis, we point to a crowded field at the zenith in conditions of good seeing. We defocus the telescope, and then move in the direction of the focus in small steps. We continue past best focus, taking images at regular intervals. If the CCD is not perpendicular to the optic axis, then we expect to see stars in one part of the chip come to focus before stars in the diagonally opposite section. Performing this test on our instrument reveals that we need a negligible adjustment of the

push-pull alignment screws.

We align the instrument as described above, every time the primary mirror is re-aluminized, and additionally as needed if the stellar images seem distorted. Our instrument can potentially be used by the observatory staff to ensure that the primary mirror is aligned well and in the same place as before. Argos is sensitive to misalignments of the optic axis by as small a value as 0.4 arcmin.

### **2.2.5 Baffling Argos**

Scattered light initially posed a significant problem for Argos. The first three nights of the commissioning run proved beyond doubt that the shiny aluminium surfaces of the mount had to be anodized. We chose hard black anodizing that does not corrode as easily as regular anodizing. Also, hard anodizing reflects less light than regular anodizing at a small or grazing angle of incidence due to its dull matt grey finish.

We replaced the single crude baffle in the original design with a five-stage baffle system consisting of two thin plates very close to the camera (henceforth, camera baffles), and three other baffles in the body of the mount (henceforth, mount baffles). The two camera baffles and the mount baffle closest to the camera have square shaped apertures with rounded corners and are derived by projecting the light beam backwards from the CCD chip. These are a few percent larger than the converging light beam from the primary. The other two mount baffles have circular apertures, which are 5-7% larger than the light beam. The edges of all the light baffles are at an angle of  $45^\circ$  with respect to the optic axis, so they may reflect light away from the CCD camera.

The camera baffles play a crucial role in preventing scattered light from reaching the camera. The mount baffles serve as a mere support system, and

reduce scattered light from multiple reflections. Light can be incident on the CCD chip from a small annulus enclosing the primary without any intervention from the baffle system. Scattered light can also be incident on the chip from specific angles after at least two reflections, but the dull black finish of the mount reduces the amount of stray photons at each reflection. CCD images acquired during twilight indicate that the baffle system is effective.

Constructing a special camera baffle that vignettes the CCD chip on all sides by a measured amount can also serve as a means of aligning the primary mirror of the telescope after aluminizing. This procedure can be done during the day time, and is much more precise than the method suggested in section 2.2.4. We should be able to detect changes  $\geq 10$  arcseconds in the orientation of the optic axis with ease, which would change the umbra of the vignetting pattern by 30 pixels.

## 2.3 Noise and measurement in photometry

During data reduction, we subtract the sky background from all the stars in the field, and use the constant stars to help divide out any modulations introduced by the Earth's atmosphere in the light curve of the target. We now discuss the precision of the extracted photometry and the dominant sources of noise as a function of stellar magnitude. We will not be discussing noise sources particular to an extraction algorithm or to an instrument.

The measured counts for a star contain statistical photon noise, scintillation noise mainly due to turbulence high up in the atmosphere, seeing noise chiefly due to turbulence close to the telescope, and modulations from varying atmospheric transparency. Sky counts also include statistical fluctuations, modulations from changes in transparency, etc. Noise in the stellar and sky counts add in quadrature to give us the observed noise in the reduced light curve.

Using the scintillation power spectrum published in Dravins et al. (1998), we estimate a 0.4% scatter in the light curves of bright stars with exposure times  $\sim 1 - 3$  s. Scintillation noise arises due to atmospheric turbulence, which occurs at different spatial and temporal scales (Dravins et al. 1997). Although a large aperture allows us to average the high frequency components, we are still susceptible to the low frequency variations. Additional transparency changes occur due to changing mist, dust, etc. in the light path. Figure 2.6 shows a series of bright stars observed with Argos, along with the faint target (top panel,  $g=19.7$ ). We can easily see the correlation in the light curves of the different bright comparison stars, spread over the chip at angular separations of 2-2.5 arcmin. We verified this correlation for a series of observing runs. We conclude that the cumulative effect of low frequency scintillation and transparency changes is mostly correlated over the CCD chip. For faint stars, read noise and stochastic sky noise add in quadrature to swamp out scintillation effects.

We show the root mean square (RMS) scatter in the light curves of constant stars as a function of magnitude in Figure 2.7. We used 10 s exposures for all the data shown in the plot. RMS scatter is a good indicator of the different sources of noise discussed above. It depends chiefly on the length of the exposure, weather conditions, extinction, and filters used. It can vary by as much as a factor of two for a given instrument set up, and for the same exposure time. Note that the magnitude on the x axis is not the true apparent magnitude of the star; it is an instrumental magnitude obtained by comparing the counts of the constant star with the target<sup>4</sup>. The scatter in the plot comes from using a different set of comparison stars for different fields, and from a varied range of weather conditions and extinction values. Figure 2.7 shows a model of photon noise and sky noise. Photon noise is the dominant source of noise

---

<sup>4</sup>When we use a faint target to determine the magnitude of a fairly bright unsaturated comparison star, our determination will be far from the true apparent magnitude of the star.

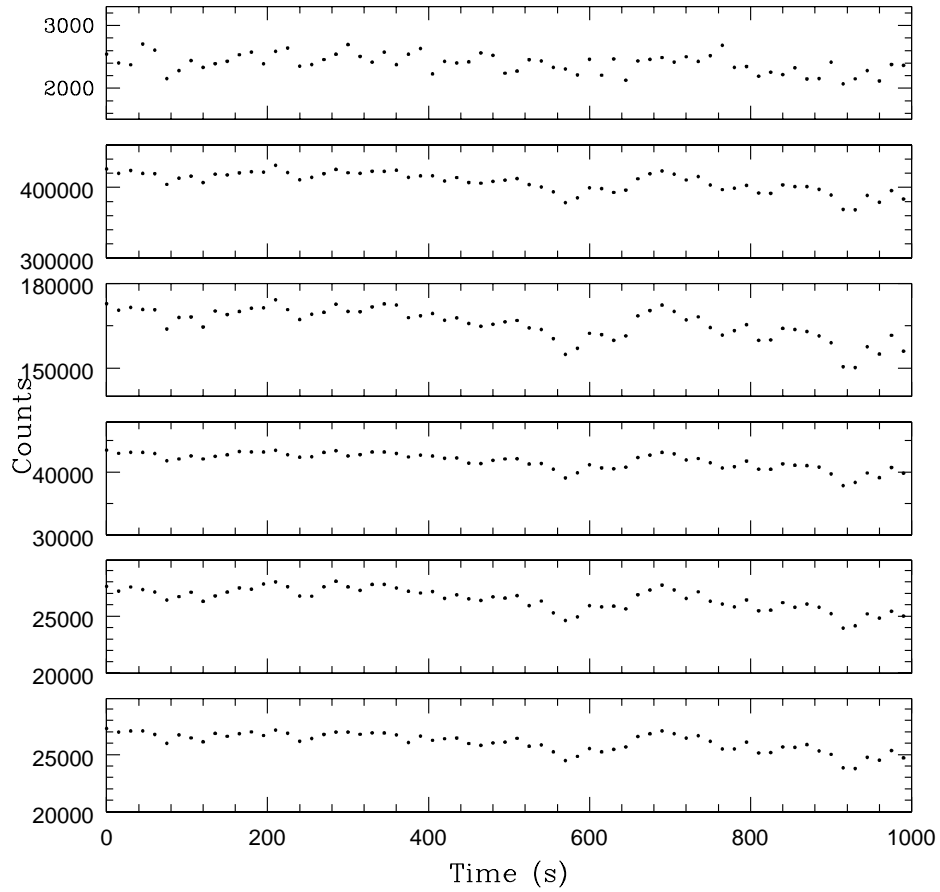


Figure 2.6: We show the sky-subtracted light curves of a white dwarf (top panel,  $g=19.7$ ) along with the comparison stars in the field. The light curves of the bright comparison stars show that low frequency scintillation noise and transparency changes are mostly correlated over the chip, as these stars are at angular separations of 2.0-2.5 arcmin.

for bright stars, while read noise and sky noise dictate the noise level for faint stars<sup>5</sup>. The magnitude at which this transition takes place helps characterize the sensitivity of an instrument. We determine this to be  $\sim g=16.5$  for Argos, with an uncertainty of order one magnitude arising from our imprecise calibration of instrumental magnitudes. Figure 2.7 also proves that the data reduction techniques we use are reliable even at the faint limits of what we can observe.

Other sources of noise include deteriorating weather conditions or increase in cloud. We show our data on the new DA variable WD0949-0000 (Mukadam et al. 2004) obtained using Argos with 10 s exposures in cloudy conditions on 2 April, 2003 in the top two panels of Figure 2.8. The top panel of the figure shows the sum of a few comparison stars in the field; the drop in the raw counts allows us to estimate that the clouds are about 10-20%. The second panel shows the reduced light curve of the faint ( $B \approx 18.8$ ) target star, after dividing by the summed comparison.

Bad seeing conditions prove to be just as detrimental to faint stars, as do clouds. The lower two panels of Figure 2.8 show the light curves of the same star WD0949-0000, acquired on 27 March, 2003, when the seeing conditions deteriorated from 2 arcseconds to 3 arcseconds. These light curves were obtained using a constant aperture weighted with a Gaussian, and hence the change in seeing conditions causes a large change in the raw counts. This is not worrisome as the pattern divides out quite well. The lowest panel of the figure shows the reduced light curve of the target with a larger scatter than due to 20% cloud.

---

<sup>5</sup>Specifications for the CCD camera indicate a read noise of 8 electrons RMS. This value makes the expected noise much higher than the observed noise for the faint stars. We measure a read noise of 4 electrons RMS by requiring that the quadrature sum of read noise and stochastic sky noise should match the observed noise for faint stars.

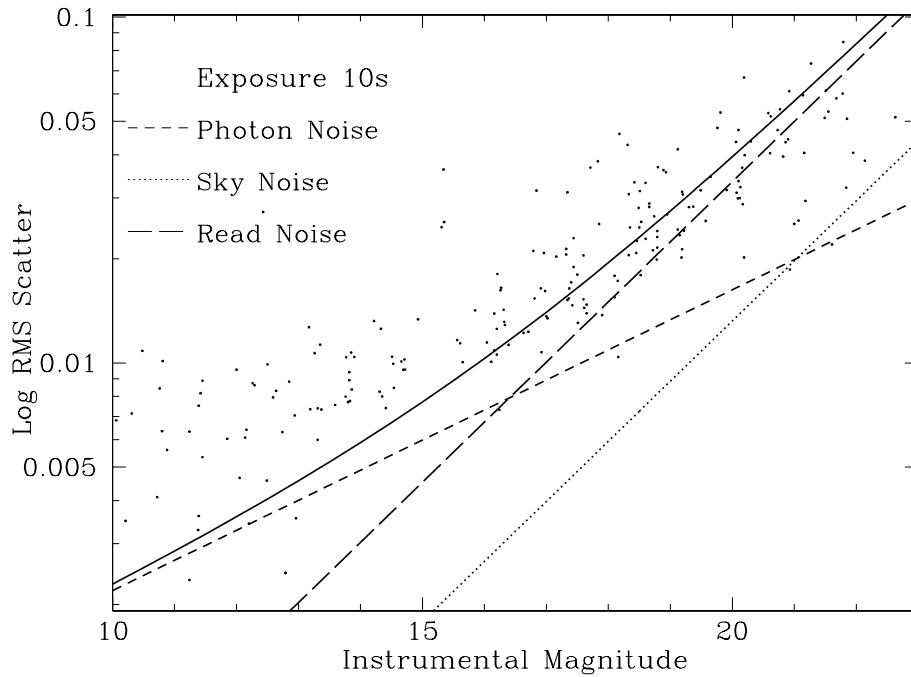


Figure 2.7: We show the root mean square scatter in the light curves of the comparison stars or the photometric precision as a function of magnitude. We derive this relative magnitude by comparing the photon counts of the comparison star to the known white dwarf in the field. The scatter in the plot is caused by different weather conditions and different comparison stars in each field used for differential photometry. Photon noise dominates the observed noise in bright stars, while the quadrature sum of read noise and sky noise essentially determines the noise in faint stars.

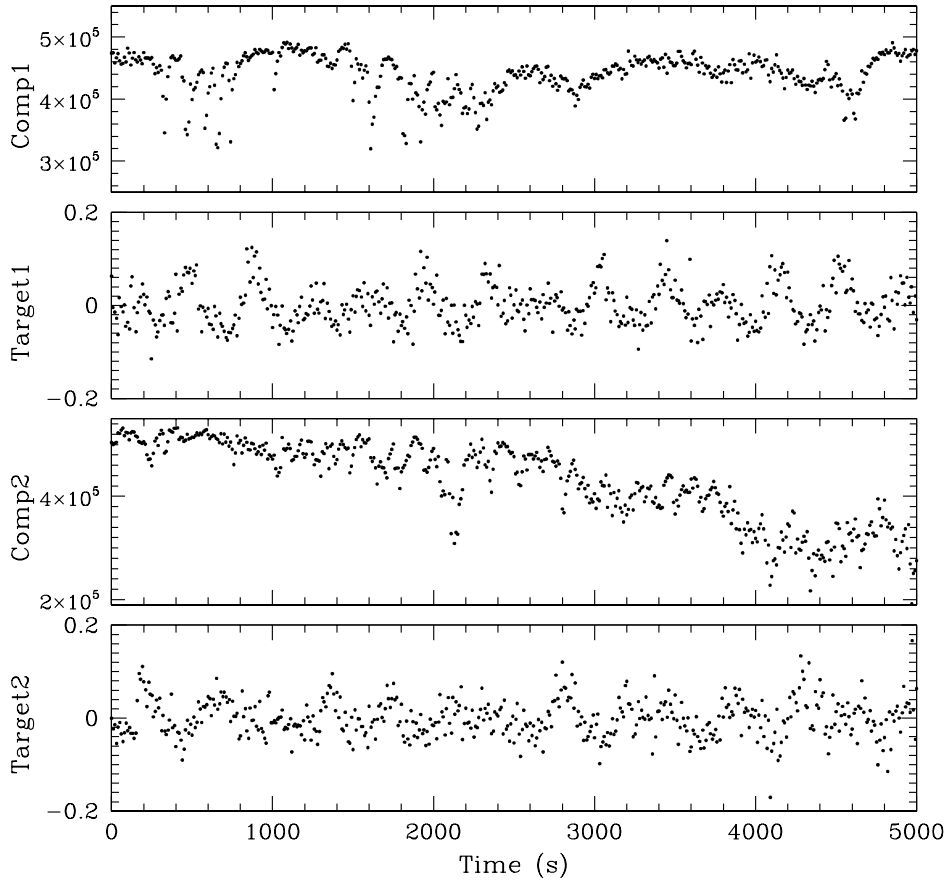


Figure 2.8: Non-photometric Weather conditions: The top two panels show data acquired in cloudy conditions, and the lower two panels show data obtained in bad seeing conditions. The top panel shows the summed light curve of a few comparison stars in the field and the reduced counts indicate 10-20% cloud. The second panel shows the reduced light curve of the faint ( $B \approx 18.8$ ) new DA variable WD0949-0000 (Mukadam et al. 2003a, 2003b), after it has been divided by the summed comparison. The third panel shows the weighted comparison in bad seeing conditions (2-3"), and the fourth panel shows the reduced light curve of WD0949-0000. Being able to extract usable data on faint stars in 20% cloud and 3 arcsecond seeing shows the limit of what is possible with Argos.

## 2.4 Time keeping with stellar clocks

We cannot measure the absolute value of time, but we can compare two different clocks with each other. The  $O - C$  diagram is a quantitative measure of the discrepancy of two clocks (e.g. Kepler et al. 1991), where  $O$  is the observed value of the phase for one clock and  $C$  is the calculated value based on a constant clock with the best fit period. A linear trend in the  $O - C$  diagram implies a correction to the best period, while a non-linear trend indicates that one clock is drifting with respect to the other. The ( $O - C$ ) technique can be used to improve the period estimates for any periodic phenomenon.

Using the hot DAVs as stellar clocks for time keeping requires high signal-to-noise data sets that resolve the pulsation spectrum well. The intervals between these seasonal data sets should be short enough to determine the number of clock ticks or cycles during the interval without an ambiguity. This phasing of data sets allows us to utilize the  $O - C$  technique to improve our determination of the period, phase, and drift rate of the stellar clock.

### 2.4.1 Uncertainty in period

When determining the period of a mono-periodic light curve without any gaps, we are essentially measuring the start time of the first cycle and the end of the last cycle. Dividing this time interval by the total number of cycles yields the period. The uncertainty in period is then related only to the precision of measuring two points in time, as we know the number of cycles definitively for continuous data. As we include additional cycles, the uncertainty in period reduces linearly with time. This reduction cannot continue indefinitely; it ceases when we reach the threshold set by the photometric precision of the light curves.

Suppose we have multiple data sets of a mono-periodic clock, and the gaps between them allow bootstrapping (see Winget et al. 1985). This technique

helps us construct data to bridge the gaps using period and phase values of the observed data. In an ideal world, where mono-periodic clocks dwell in a noise-free environment, this technique will enable the uncertainty in period to reduce linearly with time. In practice, data with gaps imply aliases. If and only if we can discern between the true frequency and the aliases, can we overcome this source of non-Gaussian noise and acquire an improvement in the period, linearly with time.

For the last case, we will consider multiple data sets that cannot be bootstrapped. We can obtain individual measurements of the period from each light curve and weight them according to their uncertainties. The uncertainty in period in this case reduces as the square root of the number of measurements, and also depends on the individual uncertainties.

The top panels of Figures 2.9 and 3.0 show the uncertainties in period determined by a non-linear least squares fit to light curves of different durations. Both stars shown in Figure 2.9, G 117-B15A and WD1354+0108, consist of a single dominant period, and can effectively be treated as mono-periodic clocks. Their uncertainties scale inversely with time and also with pulsation amplitude.

#### **2.4.2 Uncertainty in phase**

Measuring the period in a given light curve is a different process than using the light curve to determine the phase, and consequently the uncertainties in these quantities behave differently. Phase is only meaningful when we can define the period of a phenomenon. Each cycle in the light curve provides an independent measure of the phase, and so we improve as the square root of the number of measurements. The uncertainty in phase reduces as square-root of time passes by.

For multiple data sets that have been successfully bootstrapped, the un-

certainty in phase should reduce as the square-root of time only if we identify the true frequency correctly from among the aliases. For multiple data sets that cannot be bootstrapped, we cannot improve our phase value beyond that of a single set.

The lower panels of Figures 2.9 and 3.0 show the corresponding plot for the uncertainty in phase. We can determine the uncertainty in phase for a mono-periodic star of the same brightness by scaling inversely with pulsation amplitude.

### 2.4.3 Uncertainty in drift rate measurements

G 117-B15A and R 548 are the most stable optical clocks known; constraints on the drift rates of their dominant modes are smaller than a few times  $10^{-15}$  s/s (Kepler et al. 2000a; Mukadam et al. 2003a). These constraints have been established with observations that span over three decades, using bootstrapped data sets.

If there are no cycle count errors in the  $O - C$  diagram, then we can expect that initial drift rate measurements will improve linearly with time. This is because the initial improvement in the drift rate comes from an improving measure of the period. After this initial era, the scatter in the  $O - C$  diagram will inhibit further improvement in the period. Only after our measurement of the period is precise enough, can we start using the  $O - C$  diagram to obtain meaningful constraints on the drift rate. Adding subsequent observations to the  $O - C$  diagram should theoretically result in drift rate constraints that improve as the square of time goes by, until impeded by the scatter in the diagram. However, Kepler et al. (2000a) find that drift rate uncertainties decrease linearly with time for G 117-B15A, possibly due to the 1.8 s scatter. We cannot verify this theoretical expectation for R 548 either because the  $O - C$  diagram consists

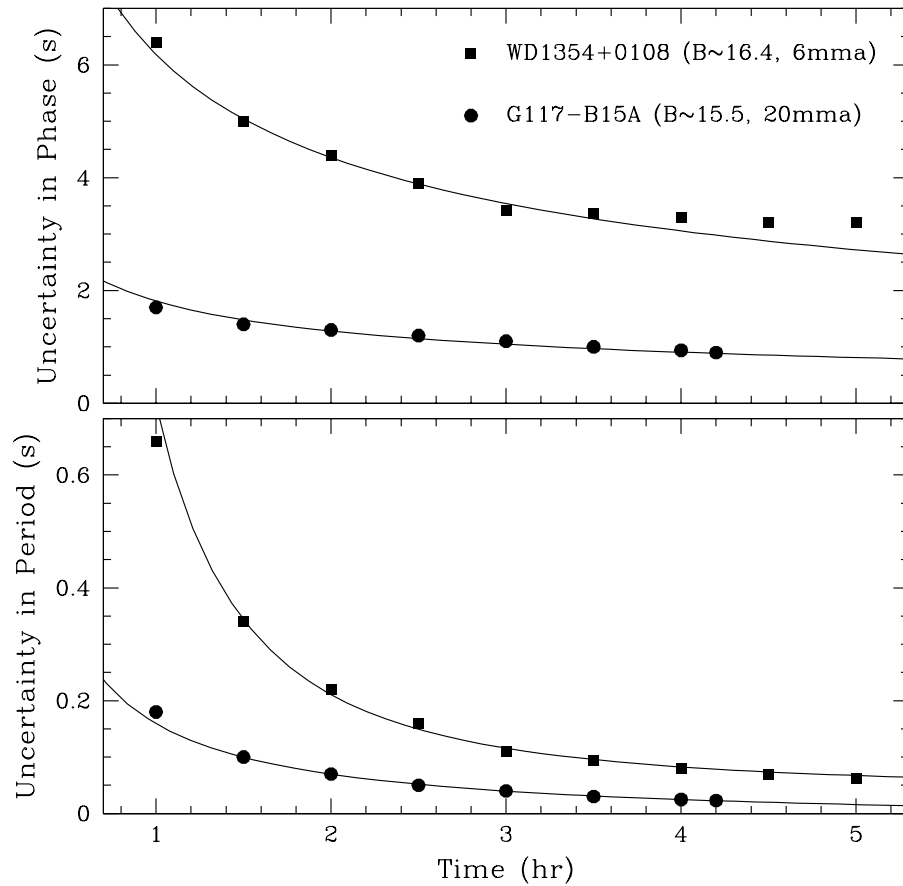


Figure 2.9: The top panel shows the uncertainty in period reducing linearly with time for G117-B15A and WD1354+0108. Both these stars can effectively be thought of as mono-periodic clocks. Their uncertainties scale inversely with pulsation amplitude. The lower panel shows the uncertainty in phase improve with the square root of time. Changes in sky transparency and approaching twilight at the end of the observing run on WD1354+0108 do not allow the uncertainty in phase to improve any further.

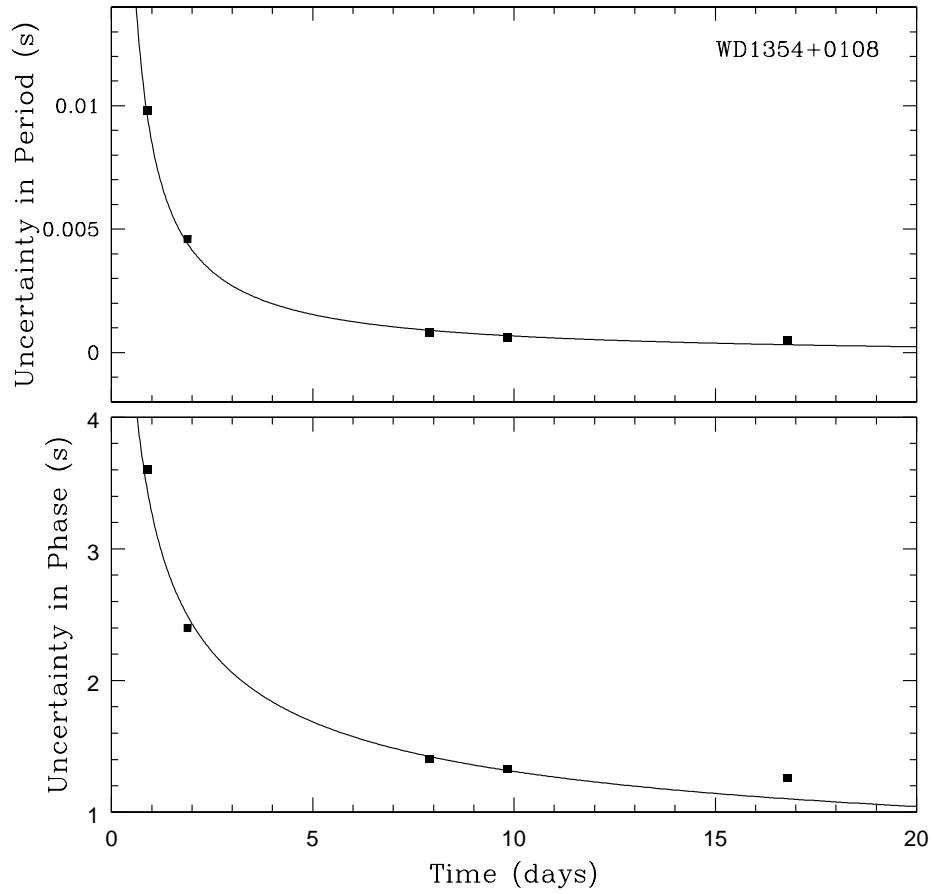


Figure 2.10: The top panel shows the uncertainty in period and in phase for a mono-periodic clock WD1354+0108 over 17 days. The uncertainty in period reduces linearly with time and the uncertainty in phase reduces with the square root of time.

only of 10 points, and these observations were not acquired with telescopes of similar aperture (or more precisely, detection systems of comparable efficiency, i.e. comparable telescope apertures, instrument efficiencies, and weather conditions).

## 2.5 Reflections

Argos saw first light on 1 November, 2001, at the prime focus of the 2.1 m telescope at McDonald Observatory, six months after we purchased the CCD camera from Roper Scientific. After struggling with initial problems concerning timing, scattered light, inexperienced observers, and so on, we slowly settled into an intensive program of observing 6 weeks every trimester. We discovered 35 new ZZ Ceti stars with Argos, mainly observing DAV candidates from the Sloan Digital Sky Survey. We discovered the faintest white dwarf pulsator known to date, a 20th magnitude DB variable, WD0947+0155 (Nitta et al. 2004; in preparation).

Argos was also instrumental in the discovery of optical bursts from a low mass X-ray binary MS 1603.6+2600. The optical bursts confirmed that the compact object was a neutron star (Hynes, Robinson, & Jeffery 2004).

## Chapter 3

# Search for new ZZ Ceti stars

### 3.1 Selection of DAV candidates from databases

In order to find a substantial number of ZZ Ceti stars, we required a large database for candidate selection; homogeneity of the database would ensure a high efficiency for our search. We decided to turn to the ongoing Sloan Digital Sky Survey (SDSS) and the Hamburg Quasar Survey (HQS).

#### 3.1.1 Sloan digital sky survey

Using a dedicated 2.5 m telescope with a CCD camera (see Gunn et al. 1998), the SDSS will ultimately result in five band photometry of ten thousand square degrees in the north Galactic cap (York et al. 2000). It is a calibrated photometric and astrometric digital survey (see Hogg et al. 2001; Pier et al. 2003) with follow-up spectroscopy of selected objects, mainly targeting bright galaxies and quasars from the imaging survey. Potential white dwarfs are allocated fibers for spectroscopy only when the number of higher priority targets is insufficient to fill the 640-fiber spectroscopic plug plates (Kleinman et al. 2004). There have been three public data releases by the SDSS: the Early Data Release (EDR;

Stoughton et al. 2002), Data Release 1 (DR1; Abazajian et al. 2003), and Data Release 2 (DR2; Strauss et al. 2004). Kleinman et al. (2004) present 2561 spectroscopically identified white dwarfs from DR1; Harris et al. (2003) presented the initial survey of the SDSS white dwarfs.

### 3.1.2 Hamburg quasar survey

Hagen et al. (1995) describe the HQS as a wide angle objective prism survey to find bright quasars in the northern sky in an area of 14 000 square degrees using plates taken at the Calar Alto Schmidt telescope. Homeier & Koester (2001a) have produced a catalog of about 3000 DA white dwarfs in the temperature range of 9 000–30 000 K using an automated classification of the low resolution digitized photographic prism spectra, 1100 of which were found to have effective temperatures close to the ZZ Ceti instability strip. Homeier et al. (1998) present  $T_{\text{eff}}$  and  $\log g$  values from follow-up spectroscopy of 80 HQS DA white dwarfs.

## 3.2 Techniques to select the SDSS DAV candidates

We outline below the different techniques that we used to select the SDSS DAV candidates along with the corresponding success rates. The success rate of discovering ZZ Ceti stars depends not only on the number of variables found, but also on our definition of a non-variable, i.e., at what detection threshold do we stop pursuing a DAV candidate and call it a non-variable. The success rate for all search techniques is higher for brighter stars ( $14.5 \leq B \leq 17.5$ ), for which we obtain a typical noise level of 1–3 mma in 1–1.5 hr runs with Argos on the 2.1 m telescope. However, most of our targets are fainter ( $18 \leq B \leq 19.5$ ) and require a larger amount of telescope time to achieve the same noise level.

For such stars, our typical 2 hr observing runs lead to a detection threshold of 3–6 mma with Argos.

### 3.2.1 Photometric technique for the SDSS DAV candidates

Greenstein (1982) acquired multichannel spectrophotometry for 14 DAVs and found that they lie in a narrow range in color space  $-0.41 \leq G - R \leq -0.29$ . He concluded that the narrow band ( $G - R$ ) color is an excellent temperature indicator for DAs. The SDSS color system comprising the filters  $u$ ,  $g$ ,  $r$ ,  $i$ , and  $z$ , calibrated by Smith et al. (2002), is a broadband color system like that of Johnson. Fontaine et al. (1982) show that DAV candidate selection based on the Johnson filter system yields a 30% success rate, for spectroscopically identified DA white dwarfs. Hence we expected to find one pulsator for every 3 candidates observed at the telescope and started using the photometric technique in the initial stages of the project.

Selection of candidates from the SDSS EDR (Stoughton et al. 2002) required us to calibrate the DAV strip in the SDSS colors as the EDR did not include any known DAVs. The original SDSS filter system  $u'$ ,  $g'$ ,  $r'$ ,  $i'$ , &  $z'$  is described in Fukugita et al. (1996). Stoughton et al. (2002) describe how the current adaptation  $u$ ,  $g$ ,  $r$ ,  $i$ , &  $z$  differs from the original filters. We utilized this technique in the early stages of the search and hence the following description alone is given in terms of the original SDSS filter system.

Lenz (1998) derived synthetic colors in the SDSS filter system for white dwarfs with Multi-Channel Spectro-Photometric (MCSP) data from Greenstein & Liebert (1990). We used DA white dwarfs common to both papers and compared their MCSP  $G - R$  colors to their synthetic SDSS  $g' - r'$  colors and also  $U - V$  colors to  $u' - g'$  colors. Neglecting higher order terms, a best-fit parabola to the resultant plots gave us the following transformations:

$$g' - r' = a + b(G - R) + c(G - R)^2 \quad (3.1)$$

$$u' - g' = d + e(U - V) + f(U - V)^2 \quad (3.2)$$

where  $a = 0.0296 \pm 0.0057$ ,  $b = 0.679 \pm 0.010$ ,  $c = 0.000 \pm 0.024$ ,  $d = 0.137 \pm 0.011$ ,  $e = 0.776 \pm 0.029$ , and  $f = 0.013 \pm 0.021$ .

Using this transformation, we chose spectroscopically identified DA white dwarfs in the color range  $0.3 \leq u' - g' \leq 0.6$  and  $-0.26 \leq g' - r' \leq -0.16$  as our highest priority candidates. We achieved a success rate of 25% at the detection threshold of 1-3 mma for the candidates so chosen. We found the success rate to be 13% for the detection threshold of 3-6 mma. We found five pulsators with this technique (Mukadam et al. 2003b) before moving to spectroscopic selection techniques with a higher yield.

### 3.2.2 Equivalent width technique for the SDSS DAV candidates

Although the primary goal of the SDSS is extragalactic objects, spectroscopy of interesting stellar objects is also obtained. The SDSS program to target quasars and other blue objects resulted in many white dwarf spectra. DA white dwarf spectra show Balmer absorption lines, pressure broadened by the extremely high gravity. The SDSS spectra cover a wavelength range of 3800-9200 Å and have a resolving power of  $\sim 2000$ , sufficient to resolve the absorption lines clearly. The equivalent widths of the  $H_\beta$  and  $H_\gamma$  lines correlate well with the effective temperature of the star, which essentially determines whether or not the star will pulsate.

We have measured the equivalent widths of the  $H_\beta$  and  $H_\gamma$  lines for all the observed variables and non-variables, which had been previously selected by the photometric method. We find that the variables form a cluster in equivalent width space (except for the unusual pulsator WD2350-0054), as shown in Figure 3.1, suggesting a new technique to pre-select ZZ Ceti candidates. It is

not necessary to derive the absolute temperature of a DAV candidate for this relative method, but to compare its equivalent widths (for  $H_\beta$  &  $H_\gamma$ ) to those from a homogeneous set of observed variables and non-variables. We find a success rate of 56% at the detection threshold of 1–3 mma, and a success rate of 30% at the detection threshold of 3–6 mma for this technique. This is effectively a low resolution spectroscopic technique and hence has a lower success rate compared to the following spectroscopic technique. Except for the opacity maximum, there are generally two temperature solutions for a given equivalent width of  $H_\beta$  and  $H_\gamma$  (see Figure 4 in Bergeron et al. 1995), and this additionally explains the relatively low success rate of this technique.

### 3.2.3 Spectroscopic technique for the SDSS DAV candidates

Our collaborators in the SDSS use Detlev Koester’s atmosphere models that treat convection with  $ML2/\alpha = 0.6$ <sup>1</sup>, best described in Finley, Koester, & Basri (1997) and references therein, to derive  $T_{\text{eff}}$  and  $\log g$  fits for DA white dwarf spectra in the range 3870 Å to 7000 Å. Kleinman et al. (2004) give a detailed discussion of the method used to derive the temperatures and gravities for these white dwarfs<sup>2</sup> Since we are establishing the ZZ Ceti strip empirically, we need not worry about any minor discrepancies between different theoretical models, as long as a consistent set of models are utilized for all candidates.

We choose our high priority ZZ Ceti candidates between an effective tem-

---

<sup>1</sup>Various parameterizations of the mixing-length theory (MLT) are used to treat convection in models of ZZ Ceti stars. Böhm & Cassinelli (1971) describe the ML2 version of convection, assuming the ratio of the mixing length ( $l$ ) to the pressure scale height ( $H$ ),  $\alpha \equiv l/H = 1$ . Bergeron et al. (1995) analyzed optical and ultraviolet (UV) spectrophotometric data of ZZ Ceti stars and found that model atmospheres calculated using the ML2 version, assuming  $\alpha = 0.6$ , provide the best internal consistency between the optical and UV temperature estimates, the observed photometry, the trigonometric parallax measurements, and the gravitational redshift masses.

<sup>2</sup>The DR1 white dwarf catalog in the public domain can be found at <http://hello.apo.nmsu.edu/~sjnk/sdsswds/dr1cat/vac/wdDAS.table.DR1.html>. The DR2 public website can be found at <http://www.sdss.org/DR2>.

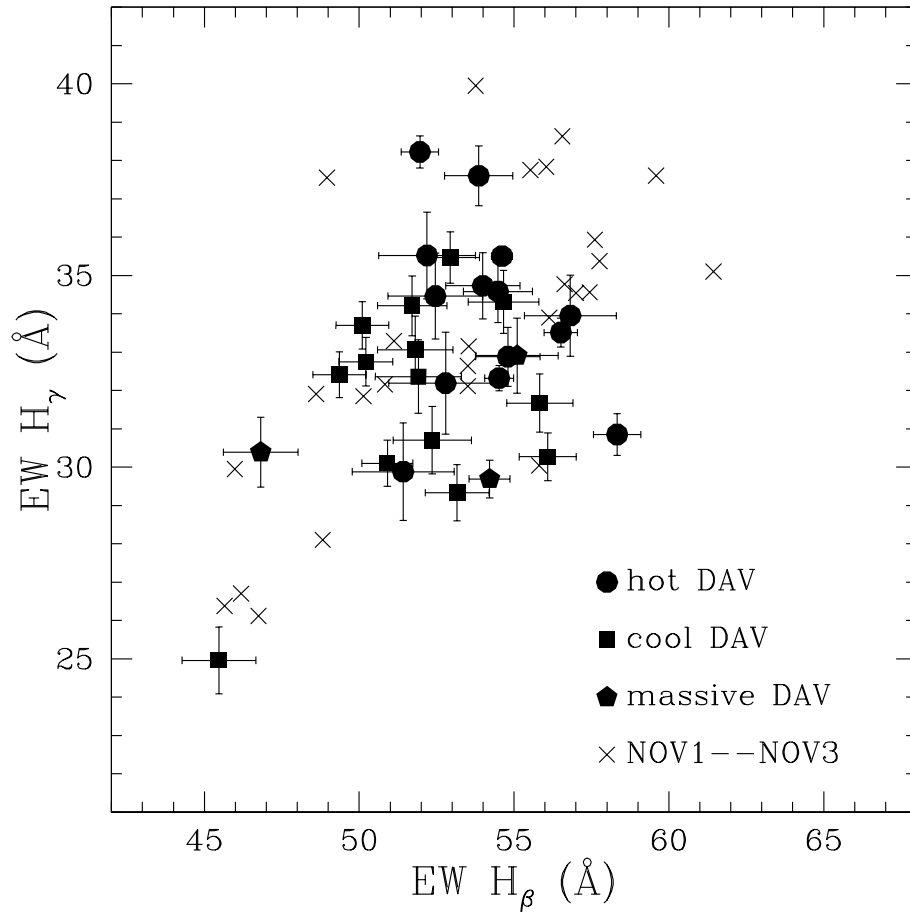


Figure 3.1: Plot of equivalent widths of  $H_\gamma$  and  $H_\beta$  lines for the observed SDSS DA white dwarfs: All but one of the SDSS pulsators are found in a small region in equivalent width space. In this region, we find a success rate of 56% at a detection threshold of 1-3 mma.

perature of 12 500 K and 11 000 K. We achieve a success rate of 80% at a detection threshold of 1–3 mma for this technique and a success rate of 50% at a detection threshold of 3–6 mma. These rates are reflected in Figure 3.2. We can achieve a higher success rate of 90% by confining our candidates to the temperature range 12 000–11 000 K, but being mainly interested in finding hDAV stars, we choose to include candidates in the temperature range 12 500–12 000 K in our observations. Our choice of candidates will also help in better establishing the blue edge of the ZZ Ceti strip.

Note that we use the spectroscopic technique in conjunction with the equivalent width method during our search. It is therefore difficult to present meaningful statistics on these two techniques separately. However, we realize that equivalent width information is already contained in the line profiles; the equivalent width method is a low resolution spectroscopic technique. We concur with Fontaine et al. (2001, 2003) that the spectroscopic technique is the most fruitful way to search for these pulsators.

### 3.3 Spectroscopic technique for HQS DAV candidates

The spectroscopic technique can be applied to photographic spectra as well, and has been used to obtain temperature estimates of DA candidates from the HQS (Homeier & Koester 2001b; Homeier 2001). Due to the significantly lower  $S/N$  ratio of the prism spectra, which also do not show resolved line profiles, errors in  $T_{\text{eff}}$  are typically 1 000–2 000 K. In some cases, the solutions can be on the wrong side of the Balmer line maximum (e. g. PG 1632+153). Also, Homeier (2003) estimate that 10–20% of this sample may not be white dwarfs. This collectively explains our low success rate at finding DAVs from this sample, and why we focused mainly on the SDSS white dwarfs. We achieve a success rate of 12.5% at the detection threshold of 1–3 mma and 9% for 3–6 mma in finding new

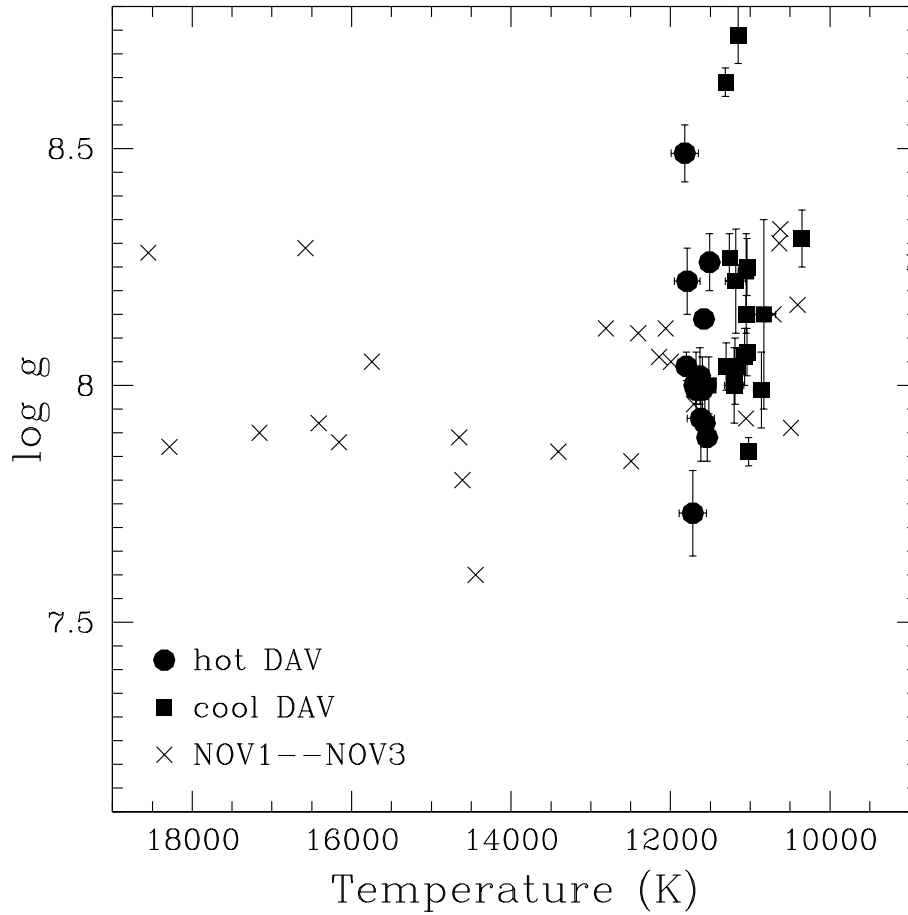


Figure 3.2: We show temperature and  $\log g$  determinations of the observed SDSS DA white dwarfs using Koester's model atmospheres. By restricting our observations in the range  $11\,000 < T_{\text{eff}} < 12\,500\text{K}$ , we achieve a success rate of 80% in identifying new DAV stars with this method.

DAVs from the HQS.

## 3.4 Data acquisition and analysis

### 3.4.1 Observing strategy

Searching for coherent signals in light curves helps in overcoming noise, as our signal-to-noise ratio improves with the time-base until we reach a limit set by photometric precision. In time series photometry, the signal-to-noise ratio can be calculated in Fourier space. Note that the signal-to-noise ratio depends not only on the magnitude of the star and the amplitude of pulsation modes, but also on the quality and duration of the data. We typically observe bright candidates ( $14.5 \leq g \leq 17.5$ ) for 1-1.5 hr each and faint candidates ( $18 \leq g \leq 19.5$ ) for about 2 hr each. We run online data extraction routines that allow us to plot the light curve and FT of the star in real time. If any of these show interesting features, we observe the target for longer. If we find a pulsator, we observe it for a few hours, and at least twice to confirm its variability. We have been obtaining multiple four hour long data sets on the newly discovered hDAVs for our planet search project.

A ZZ Ceti star may have closely spaced modes or multiplet structure, both of which cause beating effects. A fraction of our low success rate with any technique can be attributed to our single-run investigations of most candidates; an apparent non-pulsator could well be a beating ZZ Ceti star or a low amplitude variable. For example, McGraw (1977) claim BPM 37093 to be non-variable, but Kanaan et al. (1992) show it to be a low amplitude variable with evident beating. Dolez, Vauclair, & Koester (1991) state that the non-variability limit of G 30-20 is a few mmag<sup>3</sup>, but Mukadam et al. (2002) found G 30-20 to be a beating

---

<sup>3</sup>One milli-magnitude (mmag) equals 0.1086% change in intensity.

variable with an amplitude of 13.8 mma. Further observations of these stars are necessary to acquire in order to be certain of the purity of the instability strip. We will re-observe our apparent non-variables that lie in the empirically established ZZ Ceti strip with our collaborators in the coming year.

### 3.4.2 Data acquisition

We have obtained high speed time series photometry with the prime focus CCD photometer Argos on the 2.1 m telescope at McDonald Observatory for 125 nights since February 2002, using the acquisition software written by R. E. Nather (see Nather & Mukadam 2004). During this time, we observed approximately 120 SDSS DA white dwarfs and 20 HQS stars. We used 5–15 s exposures for most of our targets. We have used a 1 mm thick Schott glass BG40 filter<sup>4</sup> for most of our observations (see 2.2.2).

### 3.4.3 Data reduction and results

We extract sky-subtracted light curves from the CCD frames using the IRAF script developed by A. Kanaan. O'Donoghue et al. (2000) find this technique of weighted circular aperture photometry to be one of the best extraction techniques. We use the average seeing during the observing to serve as the Full Width at Half Maximum (FWHM) for the weighting Gaussian function. Weighting minimizes the dependence of the S/N ratio of the reduced light curve on aperture size. To select the optimum aperture size, we employ two different methods. The first method involves computing FTs for light curves extracted using different aperture sizes, but with the same weighting function. We compute the average noise of each FT, determined from the high frequency region devoid of pulsation modes. A plot of noise as a function of aperture radius then

---

<sup>4</sup>The transmission of this filter can be found at <http://www.besoptics.com>

allows us to choose the optimal aperture. We check that the amplitude of the dominant mode remains the same for all the aperture sizes. In the rare instance that it does not, we compute the S/N ratio for each light curve to make our choice.

Secondly, we use a technique suggested by M. Kilic, that involves subtracting all the light curves from a reference light curve extracted using the largest aperture. The set of residual light curves so obtained do not contain modulations due to pulsations, only noise added in quadrature from the original light curve and the reference light curve. We plot the Root Mean Square (RMS) scatter of these light curves as a function of aperture size, and the residual light curve with the lowest scatter serves as a good indicator of the optimal aperture size. This is a relative method, and the RMS scatter does not indicate an absolute measure of noise.

If these two methods do not give the same answer, then the larger of the two apertures serves as the conservative choice. The light curves of the comparison stars are also extracted with the same aperture size as the target. This is done to ensure that we do not have systematic effects from using different aperture sizes. We then correct for extinction variations and divide the light curve of the target star with the sum of one or more comparison stars; we prefer brighter stars for the division as their light curves have lower noise. After this preliminary reduction, we bring the data to the same fractional amplitude scale and convert the times of arrival of photons to Barycentric Coordinated Time (TCB; Standish 1998). We then compute a discrete FT for all the light curves.

We present the new DAVs in Table 3.1, listing their coordinates, temperature and  $\log g$  information, colors, equivalent widths, and magnitudes, along with identification numbers required to locate their spectra in the SDSS database. The SDSS spectral objects can be identified on the basis of a plate number, mod-

ified Julian date (MJD) of observation, and a fiber number. A single object may have multiple spectra, but the combination of a plate, MJD, and fiber number will always lead to a unique observation. In Tables 3.2 and 3.3, we present similar information for our observed non-variables from the SDSS. The best re-reduced photometry and spectral parameters should be obtained from the SDSS directly. We plan to publish and maintain a table with all the pulsators, complete with the latest photometry and spectral fits on [www.whitedwarf.org](http://www.whitedwarf.org) at a future date. We list our observed variables and non-variables with the non-variability limit from the HQS in Table 3.4, some of which may not necessarily be DA white dwarfs.

We designate a ZZ Ceti candidate Not Observed to Vary as NOV and add the non-variability limit as a suffix to this symbol. For example, NOV2 implies a DAV candidate not observed to vary at a detection threshold of 2 mma. If peaks in the FT of a DAV candidate seem to be less than or equal to twice the average amplitude, then these peaks are most probably consistent with noise. The highest white noise peak then defines the detection threshold or the non-variability limit. If the highest peak is also reflected in the FTs of the reference stars, then we do not use it to define the detection threshold. In that case, we would apply the same test to the second-highest peak, and so on. If a peak seems significantly higher than the average amplitude, then we re-observe the candidate to determine whether the peak is real or pure noise. Scargle (1982) gives a thorough discussion of the reliability of detecting a periodic signal in noisy data.

Table 3.1: New ZZ Ceti variables

Object	SDSS Name	Plate	MJD	Fiber	RA2000	Dec2000	$T_{\text{eff}}$ (K)	$\log g$	EW ( $H\beta$ ) (Å)	EW ( $H\gamma$ ) (Å)	$u-g$	$g-r$	$g$
WD0102-0032 <sup>a</sup>	SDSS J010207.17-003259.4	396	51816	262	01:02:07	-00:32:59	11050 ± 100	8.24 ± 0.08	54.66 ± 1.14	34.31 ± 0.82	0.43	-0.04	18.21
WD0111+0018	SDSS J011100.63+001807.2	694	52209	597	01:11:01	+00:18:07	11510 ± 110	8.26 ± 0.06	52.19 ± 1.56	35.52 ± 1.13	0.41	-0.19	18.76
WD0214-0823	SDSS J021406.78-082318.4	668	52162	354	02:14:07	-08:23:18	11570 ± 090	7.92 ± 0.05	54.80 ± 1.04	32.88 ± 0.77	0.28	-0.14	17.92
WD0318+0030 <sup>a,d</sup>	SDSS J031847.09+003029.9	413	51821	483	03:18:47	+00:30:30	11040 ± 070	8.07 ± 0.05	56.09 ± 0.92	30.27 ± 0.62	0.44	-0.18	17.81
WD0332-0049 <sup>d</sup>	SDSS J033236.61-004918.3	415	51810	211	03:32:37	-00:49:18	11040 ± 070	8.25 ± 0.06	53.16 ± 1.03	29.33 ± 0.73	0.42	-0.11	18.18
WD0815+4437	SDSS J081531.75+443710.3	547	51959	350	08:15:32	+44:37:10	11620 ± 170	7.93 ± 0.09	52.79 ± 1.83	32.19 ± 1.33	0.34	-0.06	19.30
WD0825+4119	SDSS J082547.00+411900.0	760	52264	604	08:25:47	+41:19:00	11820 ± 170	8.49 ± 0.06	55.10 ± 1.33	32.91 ± 0.98	0.34	-0.11	18.50
WD0842+3707	SDSS J084220.73+370701.7	864	52320	548	08:42:21	+37:07:02	11720 ± 170	7.73 ± 0.09	56.82 ± 1.48	33.95 ± 1.06	0.54	-0.18	18.75
WD0847+4510	SDSS J084746.81+451006.3	763	52235	144	08:47:47	+45:10:06	11680 ± 110	8.00 ± 0.07	53.99 ± 1.20	34.73 ± 0.86	0.42	-0.22	18.32
WD0906-0024 <sup>d</sup>	SDSS J090624.26-002428.2	470	51929	081	09:06:24	-00:24:28	11520 ± 090	8.00 ± 0.06	52.94 ± 0.95	35.47 ± 0.67	0.44	-0.18	17.73
WD0923+0120	SDSS J092329.81+012020.0	473	51929	074	09:23:29	+01:20:20	11150 ± 70	8.74 ± 0.06	46.82 ± 1.20	30.39 ± 0.91	0.29	-0.16	18.34
WD0939+5609	SDSS J093944.89+560940.2	556	51991	476	09:39:45	+56:09:40	11790 ± 160	8.22 ± 0.07	52.46 ± 1.53	34.46 ± 1.12	0.43	-0.17	18.70
WD0942+5733 <sup>d</sup>	SDSS J094213.13+573342.5	452	51911	023	09:42:13	+57:33:43	11260 ± 070	8.27 ± 0.05	50.91 ± 0.82	30.10 ± 0.60	0.39	-0.13	17.43
WD0949-0000 <sup>a</sup>	SDSS J094917.04-000023.6	266	51630	037	09:49:17	-00:00:24	11180 ± 130	8.22 ± 0.11	51.42 ± 1.65	29.88 ± 1.27	0.45	-0.13	18.80
WD0958+0130	SDSS J095833.13+013049.3	500	51994	163	09:58:33	+01:30:49	11680 ± 060	7.99 ± 0.03	51.96 ± 0.60	38.22 ± 0.42	0.41	-0.23	16.70
WD1015+0306	SDSS J101548.01+030648.4	503	51999	329	10:15:48	+03:06:48	11580 ± 030	8.14 ± 0.02	54.61 ± 0.34	35.50 ± 0.24	0.37	-0.10	15.66
WD1015+5954	SDSS J101519.65+595430.5	559	52316	350	10:15:20	+59:54:31	11630 ± 110	8.02 ± 0.06	54.48 ± 1.11	34.58 ± 0.81	0.65	-0.31	17.95
WD1056-0006 <sup>d</sup>	SDSS J105612.32-000621.7	276	51909	073	10:56:12	-00:06:22	11020 ± 050	7.86 ± 0.03	49.36 ± 0.85	32.41 ± 0.60	0.15	-0.20	17.52
WD1122+0358 <sup>d</sup>	SDSS J112221.10+035822.4	836	52376	214	11:22:21	+03:58:22	11070 ± 080	8.06 ± 0.06	51.71 ± 1.12	34.21 ± 0.78	0.47	-0.01	18.13
WD1125+0345	SDSS J112542.84+034506.3	836	52376	050	11:25:43	+03:45:06	11600 ± 120	7.99 ± 0.07	53.86 ± 1.10	37.60 ± 0.78	0.46	-0.12	18.07
WD1157+0553	SDSS J115707.43+055303.6	841	52375	377	11:57:07	+05:53:04	11050 ± 050	8.15 ± 0.04	50.22 ± 0.87	32.75 ± 0.63	0.32	-0.04	17.59
WD1345-0055	SDSS J134550.93-005536.5	300	51666	288	13:45:51	-00:55:37	11800 ± 060	8.04 ± 0.03	56.51 ± 0.54	33.51 ± 0.38	0.38	-0.17	16.70
WD1354+0108	SDSS J135459.89+010819.3	301	51641	322	13:55:00	+01:08:19	11700 ± 050	8.00 ± 0.02	54.52 ± 0.47	32.32 ± 0.33	0.42	-0.17	16.36
WD1417+0058 <sup>d</sup>	SDSS J141708.81+005827.2	304	51609	345	14:17:09	+00:58:27	11300 ± 080	8.04 ± 0.05	55.83 ± 1.07	31.67 ± 0.76	0.47	-0.22	18.03
WD1443+0134 <sup>b</sup>	SDSS J144330.93+013405.8	537	52027	279	14:43:31	+01:34:06	10830 ± 150	8.15 ± 0.20			0.46	-0.12	18.72
WD1502-0001 <sup>d</sup>	SDSS J150207.02-000147.1	310	51990	229	15:02:07	-00:01:47	11200 ± 120	8.00 ± 0.08	52.36 ± 1.26	30.70 ± 0.88	0.37	-0.14	18.68
WD1524-0030 <sup>c,d</sup>	SDSS J152403.25-003022.9				15:24:03	-00:30:23					0.38	-0.23	16.03
WD1617+4324 <sup>d</sup>	SDSS J161737.63+432443.8	815	52374	390	16:17:38	+43:24:44	11190 ± 100	8.03 ± 0.07	51.81 ± 1.22	33.06 ± 0.88	0.45	-0.19	18.33
WD1700+3549 <sup>d</sup>	SDSS J170055.38+354951.1	820	52433	110	17:00:55	+35:49:51	11160 ± 050	8.04 ± 0.04	50.10 ± 0.85	33.70 ± 0.62	0.47	-0.16	17.26
WD1711+6541	SDSS J171113.01+654158.3	350	51691	362	17:11:13	+65:41:58	11310 ± 040	8.64 ± 0.03	54.32 ± 0.63	28.54 ± 0.46	0.19	-0.11	16.89
WD1724+5835 <sup>a</sup>	SDSS J172428.42+583539.0	366	52017	264	17:24:28	+58:35:39	11540 ± 080	7.89 ± 0.05	58.33 ± 0.77	30.85 ± 0.54	0.43	-0.19	17.54
WD1732+5905 <sup>a</sup>	SDSS J173235.19+590533.4	366	52017	591	17:32:35	+59:05:33	10860 ± 100	7.99 ± 0.08	51.91 ± 1.39	32.36 ± 0.96	0.47	-0.10	18.74
WD2350-0054	SDSS J235040.72-005430.9	386	51788	135	23:50:41	-00:54:31	10350 ± 060	8.31 ± 0.06	45.81 ± 1.23	27.16 ± 0.90	0.42	-0.11	18.10

<sup>a</sup> Multiple Spectra: WD0318+0030 (413 51929 494), WD0949-0000 (266 51602 31), WD1724+5835 (356 51779 271), WD1732+5905 (356 51779 584), WD1345-0055 (300 51943 282), WD1354+0108 (301 51942 324), WD1417+0058 (304 51957 338)

<sup>b</sup> The SDSS spectrum of WD1443+0134 shows only half of the  $H\gamma$  line; its temperature and  $\log g$  values are not reliable.

<sup>c</sup> WD1524-0030 does not have a spectrum; Photometric ID information: Run=756, Rerun=8, Camcol=2, & Field ID=769

<sup>d</sup> Large pulsation amplitudes in cDAVs imply that the true uncertainty in their photometric magnitudes can be as high as 0.1-0.2.

<sup>e</sup> The latest  $T_{\text{eff}}$  and  $\log g$  fits should be obtained either from the SDSS website directly or from [www.whitedwarf.org](http://www.whitedwarf.org) at a future date.

Table 3.2: Not Observed to Vary (NOV) (mostly single 2 hr runs) at a detection threshold of 1-3 mma

Object	SDSS Object Name	Plate	MJD	Fiber	RA2000	Dec2000	$T_{\text{eff}}$ (K)	$\log g$	EW ( $H_{\beta}$ ) (Å)	EW ( $H_{\gamma}$ ) (Å)	$u-g$	$g-r$	$g$	NOV (mma)
WD0040-0021	SDSS J004022.88-002130.1	392	51793	063	00:40:23	-00:21:30	16160 ± 060	7.88 ± 0.01	53.51 ± 0.25	32.64 ± 0.17	0.39	-0.13	14.83	NOV1
WD0152+0100	SDSS J015259.20+010018.4	402	51793	523	01:52:59	+01:00:18	12490 ± 070	7.84 ± 0.02	59.59 ± 0.47	37.60 ± 0.33	0.53	-0.16	16.43	NOV2
WD0210+1243	SDSS J021028.69+124319.0	428	51883	138	02:10:29	+12:43:19	17160 ± 090	7.90 ± 0.02	55.81 ± 0.58	30.04 ± 0.36	0.19	-0.37	16.86	NOV3
WD0222-0100	SDSS J022207.04-010050.3	406	51817	252	02:22:07	-01:00:50	12060 ± 120	8.12 ± 0.05	56.56 ± 1.03	38.63 ± 0.71	0.39	-0.16	18.04	NOV3
WD0257+0101	SDSS J025746.41+010106.1	410	51816	578	02:57:46	+01:01:06	16580 ± 210	8.29 ± 0.04	57.61 ± 0.86	35.93 ± 0.57	0.16	-0.27	17.66	NOV3
WD0318+0044	SDSS J031802.34+004439.8	413	51821	466	03:18:02	+00:44:40	18290 ± 240	7.87 ± 0.04	48.82 ± 1.13	28.10 ± 0.74	0.11	-0.29	18.35	NOV3
WD0733+2831	SDSS J073356.99+283123.8	754	52232	226	07:33:57	+28:31:24	14610 ± 290	7.80 ± 0.06	56.63 ± 1.44	34.77 ± 1.01	0.32	-0.25	18.83	NOV3
WD0740+2505	SDSS J074033.49+250511.9	857	52314	388	07:40:33	+25:05:12	18560 ± 190	8.28 ± 0.04	53.51 ± 0.93	32.11 ± 0.64	0.13	-0.35	17.83	NOV2
WD0746+3510	SDSS J074633.01+351022.8	542	51991	476	07:46:33	+35:10:23			51.12 ± 0.57	33.29 ± 0.40	0.24	-0.30	16.69	NOV2
WD0747+2503	SDSS J074724.61+250351.1	857	52314	625	07:47:25	+25:03:51	11050 ± 110	7.93 ± 0.08	53.53 ± 1.01	33.15 ± 0.71	0.44	-0.12	18.39	NOV3
WD0751+4335	SDSS J075115.11+433513.9	434	51885	445	07:51:15	+43:35:14	19330 ± 200	8.11 ± 0.03	48.61 ± 1.23	31.91 ± 0.82	0.12	-0.33	18.38	NOV3
WD0814+4608	SDSS J081451.28+460803.6	441	51868	280	08:14:51	+46:08:04	14450 ± 230	7.60 ± 0.06	50.83 ± 0.90	32.16 ± 0.62	0.39	-0.20	17.79	NOV2
WD0827+4224	SDSS J082716.89+422418.7	761	52266	476	08:27:17	+42:24:19	16410 ± 090	7.92 ± 0.02	50.14 ± 0.82	31.85 ± 0.56	0.19	-0.29	17.44	NOV3
WD0946+5814	SDSS J094624.31+581445.4	453	51915	124	09:46:24	+58:14:45	08940 ± 020	8.26 ± 0.04	27.02 ± 0.89	17.62 ± 0.66	0.48	-0.04	17.39	NOV3
WD0949-0019	SDSS J094901.28-001909.5	266	51630	026	09:49:01	-00:19:10	10710 ± 030	8.15 ± 0.03	46.75 ± 0.57	26.12 ± 0.43	0.46	-0.16	16.51	NOV3
WD1136-0136	SDSS J113604.01-013658.2	327	52294	535	11:36:04	-01:36:58	11710 ± 070	7.96 ± 0.04	57.00 ± 0.89	34.54 ± 0.63	0.37	-0.19	17.76	NOV2
WD1138+6239	SDSS J113854.36+623903.4	776	52319	511	11:38:54	+62:39:03	14650 ± 230	7.89 ± 0.05	53.76 ± 1.24	39.95 ± 0.87	0.24	-0.28	18.38	NOV3
WD1235+5206	SDSS J123541.62+520611.9	885	52379	231	12:35:42	+52:6:12	12140 ± 100	8.06 ± 0.04	57.76 ± 0.63	35.37 ± 0.45	0.41	-0.22	16.87	NOV2
WD1243+6248	SDSS J124341.27+624836.3	782	52320	360	12:43:41	+62:48:36	11990 ± 130	8.05 ± 0.06	57.44 ± 0.98	34.56 ± 0.71	0.50	-0.22	17.85	NOV3
WD1302-0050	SDSS J130247.98-005002.7	294	51986	293	13:02:48	-00:50:03	10640 ± 030	8.30 ± 0.02	46.18 ± 0.55	26.70 ± 0.39	0.40	-0.13	16.55	NOV3
WD1444-0059	SDSS J144433.80-005958.9	308	51662	256	14:44:34	-00:59:59	15750 ± 070	8.05 ± 0.02	56.14 ± 0.45	33.90 ± 0.32	0.36	-0.18	16.22	NOV2
WD1529+0020 <sup>a,b</sup>	SDSS J152933.26+002031.2	314	51641	354	15:29:33	+00:20:31	10490 ± 060	7.91 ± 0.06	48.96 ± 1.04	37.55 ± 0.71	0.48	-0.12	18.21	NOV3
WD1659+6209	SDSS J165935.59+620934.0	351	51780	372	16:59:36	+62:09:34	12410 ± 080	8.11 ± 0.03	56.04 ± 0.45	37.83 ± 0.33	0.42	-0.19	16.25	NOV2
WD1659+6352	SDSS J165926.58+635212.9	349	51699	520	16:59:27	+63:52:13	10410 ± 030	8.17 ± 0.03	45.65 ± 0.93	26.38 ± 0.65	0.44	-0.14	17.88	NOV3
WD1718+5621	SDSS J171857.82+562150.2	367	51997	416	17:18:58	+56:21:50	12810 ± 090	8.12 ± 0.03	55.53 ± 0.73	37.75 ± 0.50	0.38	-0.21	17.47	NOV3
WD1735+5730	SDSS J173513.30+573011.5	366	52017	053	17:35:13	+57:30:12	13410 ± 160	7.86 ± 0.03	61.44 ± 0.48	35.10 ± 0.33	0.37	-0.25	16.51	NOV2
WD2326-0023	SDSS J232659.21-002348.0	383	51818	111	23:26:59	-00:23:47	10620 ± 050	8.33 ± 0.04	45.98 ± 0.87	29.95 ± 0.63	0.49	-0.09	17.52	NOV2

<sup>a</sup> The star is a member of a DA4M binary system.<sup>b</sup> The non-variability limit of 3 mma comes from a half an hour long observing run and must be regarded with prudence.

Table 3.3: Not Observed to Vary (NOV) (mostly single 2 hr runs) at a detection threshold of 3–6 mma

Object	SDSS Object Name	Plate	MJD	Fiber	RA2000	Dec2000	$T_{\text{eff}}(K)$	$\log g$	EW ( $H_{\beta}$ ) (Å)	EW ( $H_{\gamma}$ ) (Å)	$u - g$	$g - r$	$g$	NOV (mma)
WD0037+0031	SDSS J003719.13+003139.2	392	51793	531	00:37:19	+00:31:39	10960 ± 050	8.41 ± 0.03	51.11 ± 0.84	30.54 ± 0.61	0.38	-0.07	17.48	NOV5
WD0050-0023	SDSS J005047.62-002316.9	394	51876	225	00:50:48	-00:23:17	11490 ± 090	8.98 ± 0.03	55.53 ± 1.39	31.15 ± 0.99	0.31	-0.10	18.81	NOV6
WD0054-0025 <sup>a</sup>	SDSS J005457.61-002517.1	394	51812	118	00:54:58	-00:25:17	10100 ± 060	8.02 ± 0.07	50.75 ± 1.37	30.84 ± 0.92	0.32	-0.16	18.55	NOV8
WD0106-0014 <sup>b</sup>	SDSS J010622.99-001456.3	396	51816	068	01:06:23	-00:14:56	14360 ± 210	7.50 ± 0.05	48.98 ± 1.20	35.95 ± 0.83	0.50	-0.22	18.18	NOV9
WD0135-0057	SDSS J013545.62-005740.1	400	51820	060	01:35:46	-00:57:40	12570 ± 500	7.80 ± 0.10	56.67 ± 1.30	36.91 ± 0.92	0.40	-0.20	18.52	NOV5
WD0215-0015	SDSS J021553.99-001550.5	703	52209	174	02:15:54	-00:15:51	15820 ± 160	7.85 ± 0.04	51.88 ± 1.42	34.60 ± 0.95	0.21	-0.28	18.65	NOV8
WD0217+0058	SDSS J021744.29+005823.9	405	51816	601	02:17:44	+00:58:24	13600 ± 240	7.94 ± 0.04	57.35 ± 0.86	38.99 ± 0.58	0.37	-0.22	17.53	NOV7
WD0224+0038	SDSS J022435.46+003857.5	406	51817	501	02:24:35	+00:38:58	09790 ± 080	8.11 ± 0.12	37.19 ± 1.65	26.94 ± 1.16	0.45	+0.05	19.06	NOV4
WD0236-0038	SDSS J023613.64-003822.2	407	51820	029	02:36:14	-00:38:22	14280 ± 440	7.65 ± 0.09	56.92 ± 1.68	29.72 ± 1.19	0.44	-0.27	19.25	NOV5
WD0238+0049	SDSS J023808.09+004908.8	408	51821	420	02:38:08	+00:49:09	13300 ± 300	7.88 ± 0.06	61.18 ± 1.43	38.66 ± 1.00	0.27	-0.19	18.79	NOV5
WD0303-0808	SDSS J030325.22-080834.9	458	51929	188	03:03:25	-08:08:34	11400 ± 110	8.49 ± 0.06	51.61 ± 1.43	30.33 ± 1.03	0.33	-0.06	18.78	NOV4
WD0326+0018	SDSS J032619.44+001817.5	414	51869	467	03:26:19	+00:18:18	12150 ± 080	8.09 ± 0.03	60.16 ± 0.76	34.24 ± 0.53	0.38	-0.20	17.42	NOV5
WD0329-0007	SDSS J032959.57-000732.5	414	51869	037	03:30:00	-00:07:33	16690 ± 330	7.82 ± 0.07	49.62 ± 1.71	29.20 ± 1.18	0.35	-0.21	19.13	NOV7
WD0330+0024	SDSS J033031.48+002454.9	414	51869	583	03:30:31	+00:24:55	14500 ± 600	7.75 ± 0.09	54.75 ± 1.51	35.38 ± 1.01	0.29	-0.20	18.97	NOV8
WD0336-0006	SDSS J033648.33-000634.2	415	51810	595	03:36:48	-00:06:34	10400 ± 040	8.26 ± 0.04	44.31 ± 0.95	27.49 ± 0.67	0.39	-0.06	17.93	NOV5
WD0340+0106	SDSS J034044.10+010621.9	416	51811	420	03:40:44	+01:06:22	12060 ± 140	8.06 ± 0.05	57.95 ± 1.10	40.45 ± 0.76	0.50	-0.17	18.23	NOV5
WD0345-0036	SDSS J034504.20-003613.5	416	51811	015	03:45:04	-00:36:14	11430 ± 150	7.76 ± 0.09	54.81 ± 1.29	30.30 ± 0.91	0.45	-0.17	19.00	NOV5
WD0753+3543	SDSS J075328.74+354304.9	757	52238	284	07:53:29	+35:43:05	16620 ± 240	8.28 ± 0.04	53.20 ± 1.30	35.20 ± 0.89	0.11	-0.27	18.46	NOV6
WD0756+3803	SDSS J075607.77+380331.7	543	52017	550	07:56:08	+38:03:32	16040 ± 250	7.84 ± 0.05	54.61 ± 1.37	34.33 ± 0.95	0.30	-0.29	18.72	NOV5
WD0816+3307	SDSS J081625.01+330740.4	862	52325	277	08:16:25	+33:07:40	15460 ± 200	7.75 ± 0.05	51.92 ± 0.92	35.19 ± 0.64	0.29	-0.32	17.78	NOV4
WD0853+0005	SDSS J085325.55+000514.2	468	51912	132	08:53:26	+00:05:14	11750 ± 110	8.11 ± 0.06	56.19 ± 1.14	33.77 ± 0.83	0.39	-0.15	18.23	NOV4
WD0953-0051	SDSS J095329.20-005100.7	267	51608	099	09:53:29	-00:51:01	10690 ± 100	8.64 ± 0.11	43.13 ± 1.53	25.88 ± 1.10	0.40	-0.05	18.85	NOV4
WD1019+0000	SDSS J101911.51+000017.3	272	51941	307	10:19:12	+00:00:17	12760 ± 150	8.35 ± 0.06	59.71 ± 1.13	37.16 ± 0.83	0.51	-0.21	18.16	NOV4
WD1031+6122	SDSS J103116.34+612232.6	772	52375	090	10:31:16	+61:22:33	11480 ± 180	7.68 ± 0.11	52.79 ± 1.46	34.85 ± 1.03	0.57	-0.20	18.71	NOV4
WD1045-0018 <sup>a</sup>	SDSS J104517.79-001833.9	275	51910	230	10:45:18	-00:18:34	09540 ± 040	8.09 ± 0.06	49.30 ± 1.19	30.40 ± 0.81	0.16	-0.14	18.36	NOV4
WD1103+0037	SDSS J110326.71+003725.9	277	51908	513	11:03:27	+00:37:26	10540 ± 050	8.22 ± 0.05	46.22 ± 0.96	29.22 ± 0.70	0.43	-0.19	17.64	NOV6
WD1105+0016	SDSS J110515.32+001626.1	277	51908	596	11:05:15	+00:16:26	12850 ± 060	8.26 ± 0.02	59.82 ± 0.29	37.05 ± 0.21	0.35	-0.19	15.20	NOV4
WD1126+5144	SDSS J112638.75+514430.9	879	52365	472	11:26:39	+51:44:31	11900 ± 150	8.03 ± 0.07	53.61 ± 1.27	34.85 ± 0.91	0.37	-0.19	18.41	NOV4
WD1216+6158	SDSS J121613.37+615817.0	779	52342	169	12:16:13	+61:58:16	12200 ± 180	8.19 ± 0.07	56.49 ± 1.13	37.49 ± 0.80	0.29	-0.16	18.19	NOV8
WD1229-0017	SDSS J122959.23-001714.5	289	51990	109	12:29:59	-00:17:15	13160 ± 180	7.89 ± 0.04	58.84 ± 0.78	40.72 ± 0.54	0.45	-0.21	17.36	NOV5
WD1315-0131	SDSS J131557.18-013125.3	340	51691	587	13:15:57	-01:31:26	12550 ± 210	8.12 ± 0.08	55.85 ± 1.22	35.85 ± 0.89	0.47	-0.21	18.24	NOV4
WD1337+0104	SDSS J133714.44+010443.8	298	51662	604	13:37:14	+01:04:44	11830 ± 210	8.39 ± 0.11	54.18 ± 1.56	33.14 ± 1.15	0.35	-0.11	18.57	NOV4
WD1338-0023	SDSS J133831.75-002328.0	298	51662	021	13:38:32	-00:23:27	11650 ± 090	8.08 ± 0.05	54.89 ± 0.68	34.48 ± 0.50	0.45	-0.18	17.09	NOV4
WD1342-0159	SDSS J134230.14-015932.8	912	52427	590	13:42:30	-01:59:33	11320 ± 160	8.42 ± 0.09	48.05 ± 1.57	34.00 ± 1.14	0.43	-0.15	18.80	NOV4
WD1345+0328	SDSS J134552.01+032842.6	529	52025	609	13:45:52	+03:28:43	11620 ± 140	7.80 ± 0.08	51.58 ± 1.23	36.92 ± 0.89	0.49	-0.22	18.58	NOV6
WD1431-0012	SDSS J143154.57-001231.2	306	51637	196	14:31:55	-00:12:31	12200 ± 180	7.92 ± 0.07	57.84 ± 1.22	35.27 ± 0.85	0.45	-0.16	18.40	NOV7
WD1432+0146	SDSS J143249.11+014615.6	536	52024	318	14:32:49	+01:46:16	11290 ± 070	8.23 ± 0.06	53.62 ± 0.86	33.21 ± 0.63	0.52	-0.16	17.49	NOV5
WD1443-0006	SDSS J144312.69-000657.9	308	51662	357	14:43:13	-00:06:58	11960 ± 150	7.87 ± 0.07	56.96 ± 1.35	34.07 ± 0.96	0.44	-0.14	18.66	NOV5
WD1450+5543	SDSS J145040.50+554321.4	792	52353	311	14:50:41	+55:43:21	15010 ± 120	7.48 ± 0.03	49.33 ± 0.83	32.91 ± 0.58	0.31	-0.33	17.21	NOV4
WD1503-0052	SDSS J150330.49-005211.3	310	51990	133	15:03:30	-00:52:11	11600 ± 130	8.21 ± 0.07	55.35 ± 1.12	36.85 ± 0.77	0.43	-0.15	18.39	NOV4
WD1545+0321	SDSS J154545.35+032150.0	594	52027	500	15:45:45	+03:21:50	15050 ± 370	7.88 ± 0.07	54.82 ± 1.45	37.91 ± 0.98	0.29	-0.24	18.76	NOV4
WD1642+3824	SDSS J164248.61+382411.2	818	52395	476	16:42:49	+38:24:11	18810 ± 200	8.40 ± 0.04	52.73 ± 1.15	31.70 ± 0.82	0.07	-0.31	17.98	NOV4
WD1651+6334	SDSS J165128.84+633438.3	349	51699	265	16:51:29	+63:34:38	14190 ± 150	7.68 ± 0.03	54.33 ± 1.09	33.08 ± 0.76	0.38	-0.31	18.21	NOV4
WD1653+6254	SDSS J165356.29+625451.4	349	51699	208	16:53:56	+62:54:51	13230 ± 170	7.94 ± 0.05	62.35 ± 1.30	39.68 ± 0.91	0.43	-0.21	18.71	NOV8
WD1657+6244	SDSS J165747.03+624417.5	349	51699	097	16:57:47	+62:44:18	13610 ± 250	7.77 ± 0.05	59.75 ± 1.40	37.82 ± 0.96	0.41	-0.21	18.87	NOV8
WD1658+3638	SDSS J165815.53+363816.0	820	52433	514	16:58:16	+36:38:16	11110 ± 120	8.36 ± 0.09	50.04 ± 1.85	27.03 ± 1.38	0.43	-0.13	19.15	NOV4
WD1706+6316	SDSS J170654.01+631659.6	349	51699	030	17:06:54	+63:17:00	13140 ± 100	8.51 ± 0.03	58.84 ± 0.81	32.88 ± 0.58	0.40	-0.13	17.72	NOV4
WD1717+6031	SDSS J171700.06+603141.8	354	51792	264	17:17:00	+60:31:42	13710 ± 480	8.17 ± 0.14	56.41 ± 1.88	38.09 ± 1.41	0.34	-0.27	19.41	NOV10
WD1718+5909	SDSS J171853.27+590927.5	366	52017	342	17:18:53	+59:09:28	12430 ± 350	7.94 ± 0.11	59.89 ± 1.28	35.29 ± 0.91	0.43	-0.16	18.64	NOV7
WD1720+6350 <sup>a</sup>	SDSS J172045.09+635031.7	350	51691	007	17:20:45	+63:50:32	11690 ± 170	8.08 ± 0.09	50.79 ± 1.34	30.68 ± 0.89	0.28	-0.21	18.63	NOV8
WD1723+5546 <sup>a</sup>	SDSS J172346.69+554619.0	367	51997	512	17:23:47	+55:46:18	11730 ± 120	8.07 ± 0.06	49.54 ± 1.40	38.52 ± 0.96	0.37	-0.14	18.91	NOV5
WD1724+6205	SDSS J172405.37+620501.4	352	51694	085	17:24:05	+62:05:01	13590 ± 300	7.81 ± 0.06	59.10 ± 1.24	38.11 ± 0.84	0.38	-0.25	18.41	NOV6
WD1724+6323	SDSS J172452.91+632324.9	352	51694	595	17:24:53	+63:23:25	14530 ± 390	7.79 ± 0.09	52.60 ± 1.59	32.63 ± 1.06	0.31	-0.28	19.01	NOV6
WD1726+5331	SDSS J172600.16+533104.1	359	51821	178	17:26:00	+53:31:03	11000 ± 110	8.23 ± 0.08	49.55 ± 1.37	27.98 ± 1.01	0.49	-0.14	18.75	NOV7
WD1735+5356	SDSS J173536.49+535658.1	360	51816	212	17:35:36	+53:56:58	12940 ± 280	7.85 ± 0.07	60.11 ± 1.34	34.77 ± 0.95	0.45	-0.19	18.65	NOV4
WD2334-0014	SDSS J233454.18-001436.2	384	51821	151	23:34:54	-00:14:36	13370 ± 250	7.86 ± 0.05	56.55 ± 1.28	41.01 ± 0.91	0.41	-0.20	18.33	NOV6
WD2336-0051	SDSS J233647.01-005114.7	384	51821	008	23:36:47	-00:51:15	13250 ± 250	7.86 ± 0.05	56.61 ± 1.23	40.05 ± 0.88	0.57	-0.25	18.28	NOV5
WD2341+0032	SDSS J234110.13+003259.9	385	51877	481	23:41:10	+00:33:00	13380 ± 330	7.90 ± 0.08	57.18 ± 1.99	36.38 ± 1.38	0.41	-0.14	19.16	NOV6
WD2341-0109	SDSS J234141.64-010917.1	385	51877	124	23:41:42	-01:09:17	13090 ± 170	7.92 ± 0.04	58.98 ± 1.07	38.34 ± 0.75	0.47	-0.21	18.04	NOV4
WD2346-0037	SDSS J234639.77-003716.0	386	51788	297	23:46:40	-00:37:16	12980 ± 330	7.97 ± 0.08	56.63 ± 1.34	36.16 ± 0.95	0.32	-0.20	18.34	NOV6

<sup>a</sup> The star is a member of a DAM binary system.

<sup>b</sup> Kleinman et al. (2004) give an interesting discussion of this most probable eclipsing star.

Table 3.4: Observed stars from the Hamburg Quasar Survey

Object	Alternate Name	NOV (mma)	$RA_{1950}$	$Dec_{1950}$	$T_{\text{eff}}$ (K)	$B_J$
HS0951+1312		hDAV	09:51:03.1	+13:12:41	11000	16.7
HS0952+1816		cDAV	09:52:25.4	+18:16:29	11000	16.2
HS0406+1700	LB 227	NOV1	04:06:37.0	+17:00:03	16000	15.4
HS0843+1956	WD 0843+199	NOV3	08:43:42.5	+19:56:05	10000	16.4
HS0848+1213		NOV2	08:48:22.0	+12:13:14	13000	16.6
HS0914+0424		NOV2	09:14:18.2	+04:24:08	13000	16.7
HS0942+1416		NOV2	09:42:04.4	+14:16:28	13000	16.9
HS0950+0745	PG 0950+077	NOV3	09:50:20.4	+07:45:19	12000	15.6
HS1102+0032		NOV2	11:02:41.4	+00:32:37	12000	14.7
HS1431+1521	PG 1431+153	NOV2	14:31:44.5	+15:21:25	11000	15.7
HS1637+1940		NOV2	16:37:58.9	+19:40:31	12000	16.7
HS1643+1423 <sup>a</sup>	PG 1643+143	NOV3	16:43:21.5	+14:23:08	$25450 \pm 260$	15.5
HS1711+1716		NOV2	17:11:41.1	+17:16:57	11000	16.7
HS2157+8152 <sup>b</sup>		NOV3	21:57:18.5	+81:53:01	$10700 \pm 40$	B=16.0
HS2306+1303	PG 2306+130	NOV1	23:06:00.3	+13:03:07	13000	15.2
HS2322+2040	PG 2322+206	NOV1	23:22:05.4	+20:40:04	13000	15.5
HS0727+6915 <sup>c</sup>		NOV4	07:27:34.6	+69:15:57	$12100 \pm 250$	B=16.9
HS0827+0334		NOV8	08:27:38.5	+03:34:51	12000	16.7
HS0838+1643		NOV4	08:38:18.7	+16:43:05	11000	17.1
HS0852+1916	LB 8888	NOV3	08:52:40.1	+19:16:06	13000	15.7
HS0926+0828		NOV6	09:26:56.8	+08:28:58	12000	16.5
HS0932+1731		NOV4	09:32:05.5	+17:31:37	12000	16.8
HS0949+0823		NOV4	09:49:17.5	+08:23:44	12000	16.6
HS1654+1927		NOV5	16:54:17.0	+19:27:46	11000	16.2

<sup>a</sup>  $\log g = 7.79 \pm 0.05$  from Finley, Koester & Basri (1997)

<sup>b</sup>  $\log g = 8.71 \pm 0.08$  from Homeier et al. (1998)

<sup>c</sup>  $\log g = 8.29 \pm 0.14$  from Homeier et al. (1998)

### 3.5 Pulsation properties of the new ZZ Ceti variables

We find that the hot DAV stars are mostly distinct from the cool DAV stars in terms of their pulsation characteristics, chiefly the pulsation periods and the pulse shapes. Short pulsation periods typically in the range of 100–300 s are representative of hDAVs, while periods longer than 600 s are typically indicative of cDAVs. Some intermediate temperature DAVs show a rich pulsation spectrum with periods ranging from a few hundred seconds up to 500 s, exhibiting characteristics of both classes. For our purposes, we classify WD0111+0018, WD0214–0823, WD1015+0306, and WD1724+5835 as hDAVs since their dominant mode is representative of the hDAV class. We use the same basis to classify WD0906–0024 as a cDAV. WD2350–0054 is by far the coolest pulsator and is unusual because it is not expected to pulsate according to our empirical determination of the edges of the ZZ Ceti strip. The effective temperature of WD2350–0054 derived from its SDSS spectrum places it 650 K below the cool edge of the instability strip. Its spectrum does not show any unusual features that we could attribute to a binary companion or contamination of any sort. Furthermore, it shows pulsation periods and pulse shapes characteristic of the hot DAV stars. The SDSS spectrum of WD1443+0134 has a missing section, and hence its temperature and  $\log g$  values are not reliable.

The hot ZZ Ceti stars show pulse shapes distinct from the cDAVs, e.g., see the light curve of WD0214–0823 compared to WD1524–0030. The brighter variables have well defined pulse shapes, while the low amplitude faint variables do not. Among the hDAVs, only the light curves of the intermediate temperature DAVs like WD1015+5954 show pulse shapes distinct from the rest. The light curves of WD0923+0120 and WD1711+6541 show pulse shapes and amplitudes distinct from other cDAVs. Their low amplitude is a result of their high gravity ( $\log g \geq 8.6$ ). The nonradial g-modes have a non-negligible radial component,

the amplitude of which scales inversely with stellar mass and plays a role in dictating the amplitude of the non-radial component.

We plot the light curves and FTs of all the new variables in Figures 3.3-3.5. We present the period spectra of the new variables in Chapter 5.

### **3.6 Conclusions**

We conclude that the spectroscopic technique, determining temperatures and  $\log g$  values by comparing the stellar spectra to a grid of atmosphere models, is the most fruitful way to search for ZZ Ceti pulsators, in accordance with Fontaine et al. (2001, 2003). We can achieve a 90% success rate by confining our candidates between 12 000 K and 11 000 K with this technique at a detection threshold of 1-3 mma. But our interest in hDAVs and the blue edge of the instability strip leads us to choose candidates between 12 500 K and 11 000 K, reducing our success rate to 80%. With the discovery of 35 new DAVs, we almost double the current sample of 39 published ZZ Ceti stars discovered over three decades.

Figure 3.3: Light curves and FTs of the new SDSS DAVs

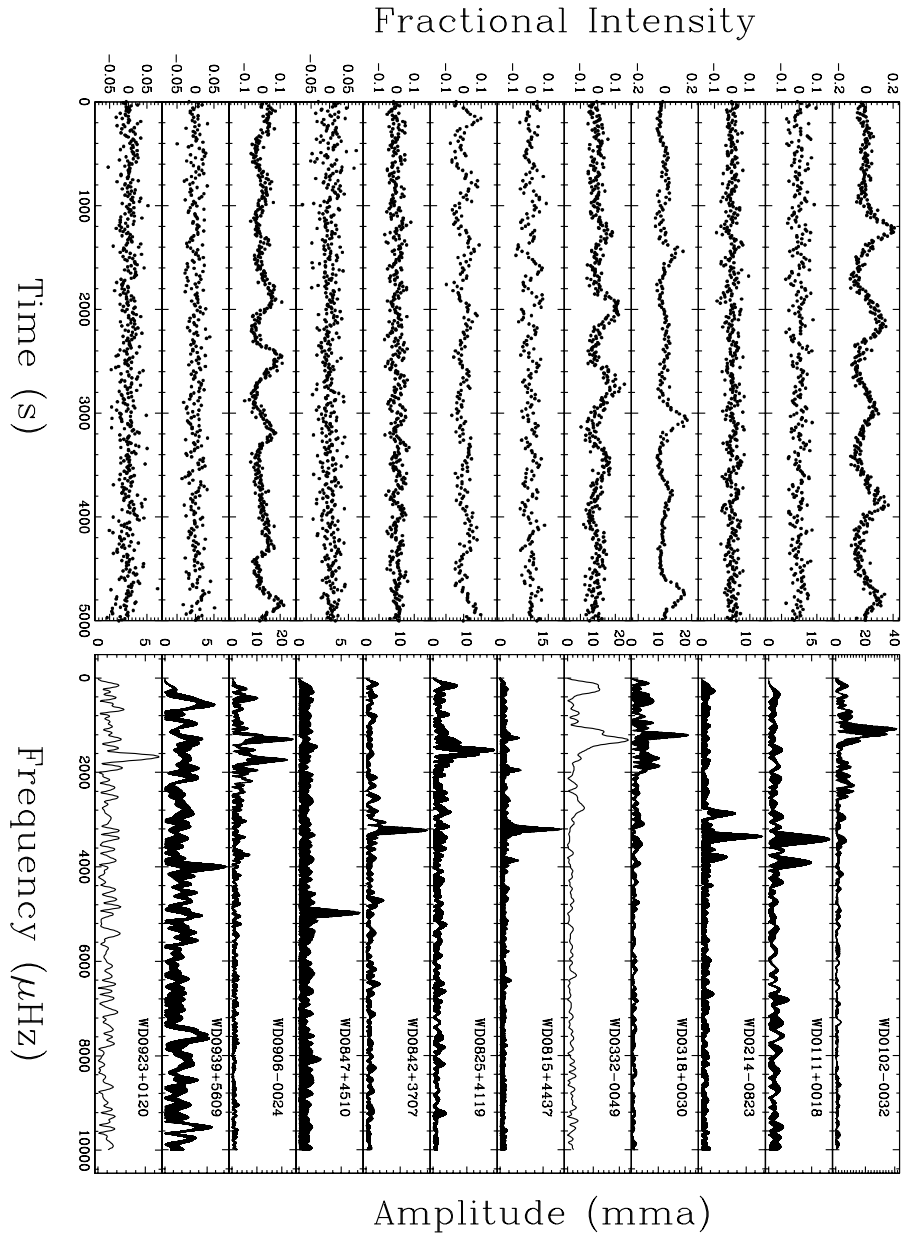


Figure 3.4: Light curves and FTs of the new SDSS DAVs

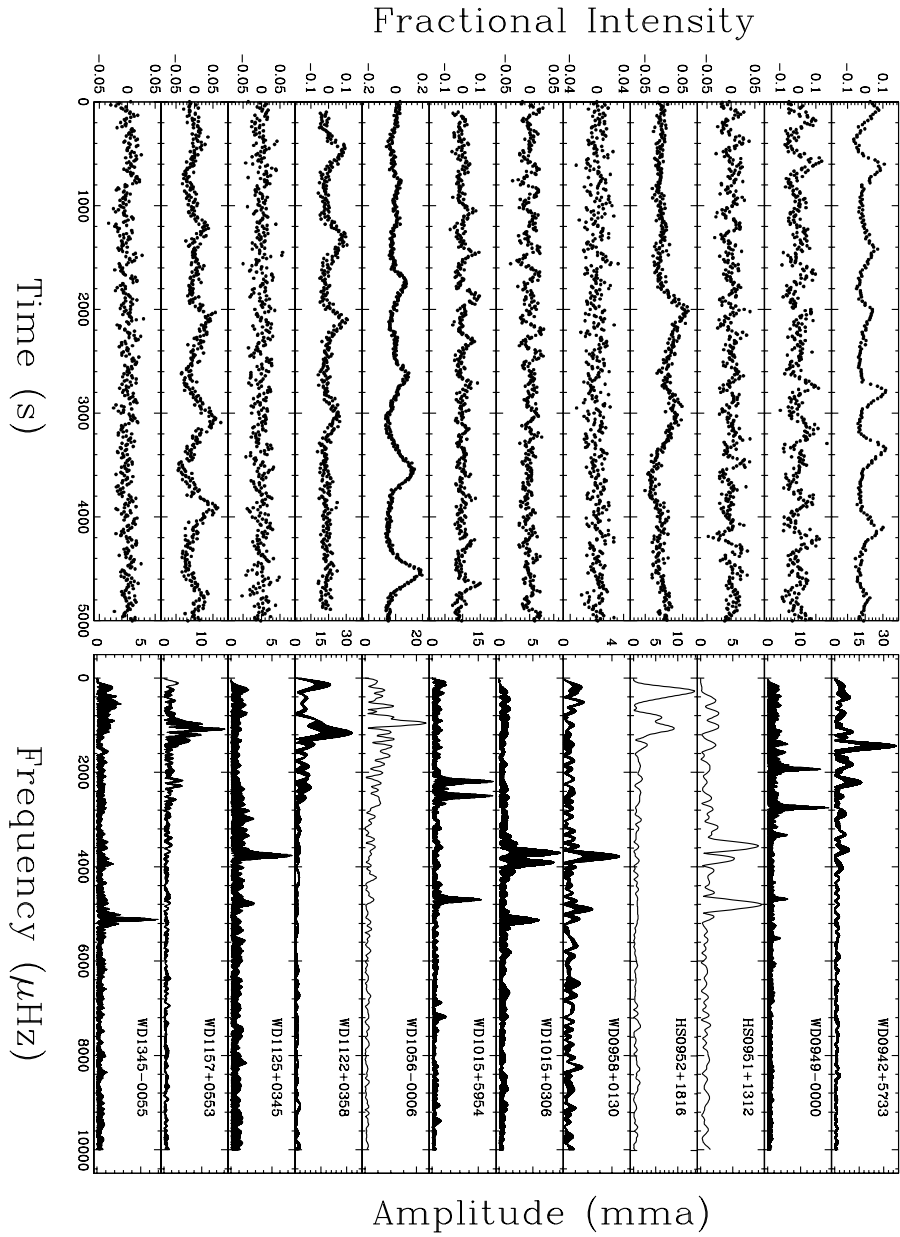
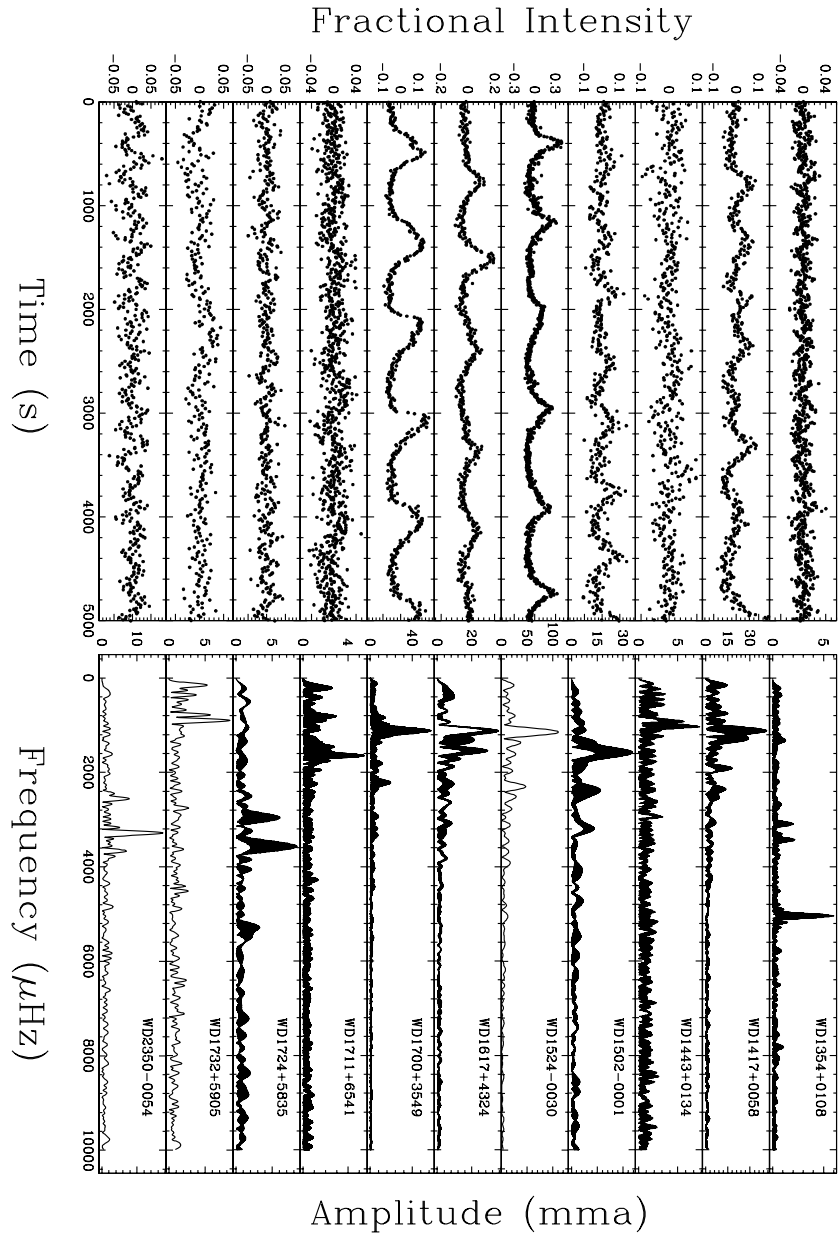


Figure 3.5: Light curves and FTs of the new SDSS DAVs



## Chapter 4

# Empirical DAV Instability Strip

This is the first time in the history of white dwarf asteroseismology that we have a statistically significant homogeneous set of ZZ Ceti spectra, acquired entirely with the same detection system, namely the SDSS spectrograph on the 2.5 m telescope at Apache Point Observatory. All the spectra have been reduced and analyzed consistently using the same set of model atmospheres and fitting algorithms, including the observed photometric colors (see Kleinman et al. 2004). This homogeneity should reduce the relative scatter of the variables in the  $T_{\text{eff}}-\log g$  plane, and possibly allow us to see emerging new features. The sample size of known DAVs is now almost twice as large since the last characterization of the instability strip by Bergeron et al. (2004). However, we will not include the previously known DAVs in our analysis with the exception of G 238-53, as these pulsators do not have SDSS spectra and will only serve to reduce the homogeneity of our sample.

We list the  $T_{\text{eff}}$  and  $\log g$  values of all the variables and non-variables we discovered within the SDSS data in Paper-I, along with their internal uncertainties. Note that we will not be considering WD2350-0054 in this paper as it may be a unique pulsator; it shows pulsation periods and pulse shapes characteristic

of the hot DAV stars, while the SDSS temperature determination places it below the cool edge of the instability strip. We focus on the general trends of the majority of the DAVs, and hence a discussion of WD2350–0054 is postponed to a future date. We will not be including WD1443–0054 either, as its temperature and  $\log g$  determinations are unreliable due to a missing portion in its SDSS spectrum. We will be including G 238-53, the only previously known ZZ Ceti star with a published SDSS spectrum.

## 4.1 Empirical instability strip

We show the empirical SDSS instability strip in Figure 4.1, as determined by 30 new ZZ Ceti stars and G 238-53. We plot histograms of the observed variables as a function of temperature and  $\log g$ , and weighted histograms (see section 2.2) for the non-variables (Not Observed to Vary; NOVs). Figure 4.1 has two striking features: a narrow strip of width 950 K and non-variable DA white dwarfs within the instability strip.

Pulsations are believed to be an evolutionary effect in otherwise normal white dwarfs (Robinson 1979; Fontaine et al. 1985; Fontaine et al. 2003; Bergeron et al. 2004). Non-variables in the middle of the strip question this semi-empirical premise, even if we use the uncertainties in temperature to justify the non-variables close to the edges.

We also note that the DAV distribution appears to be non-uniform across the strip. The features of this plot are influenced by various factors such as biases in candidate selection, non-uniform detection efficiency in the  $T_{\text{eff}}\text{-}\log g$  plane, and uncertainties as well as systematic effects in spectroscopic temperature and  $\log g$  determinations. We address these issues and their effects on the DAV distribution in the next few sub-sections.

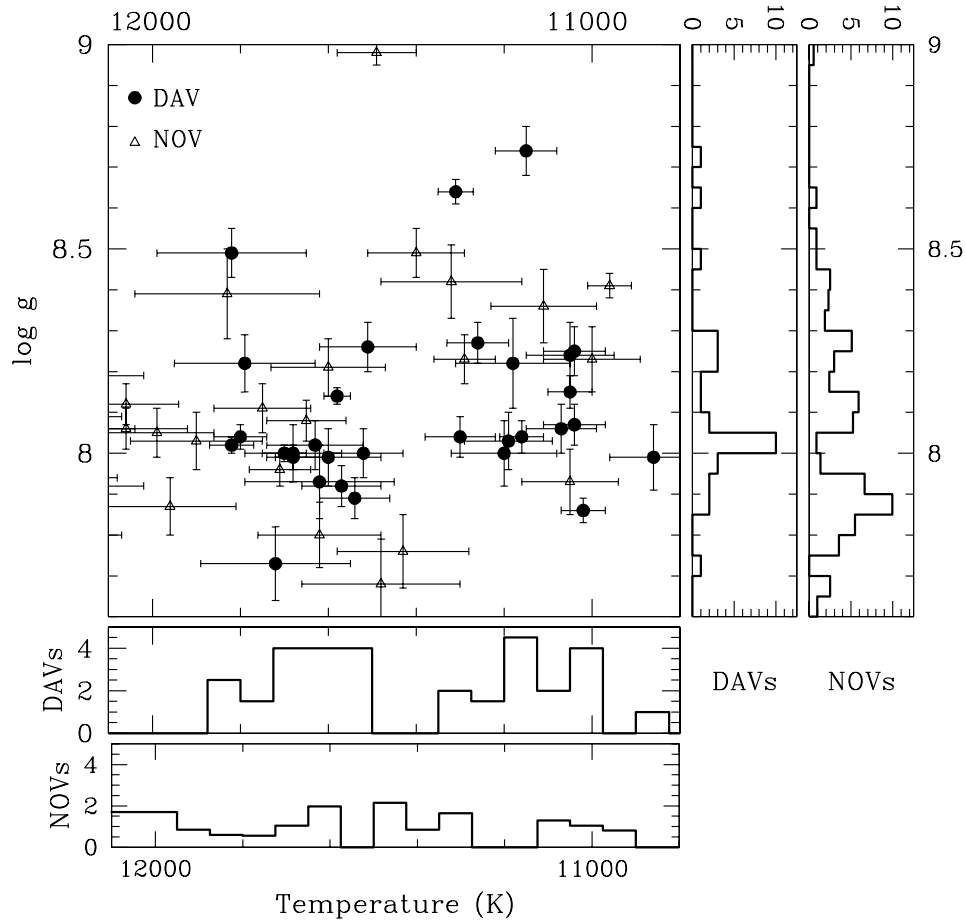


Figure 4.1: The distribution of new SDSS DAVs and NOVs (Mukadam et al. 2004) as a function of temperature and  $\log g$ . We also include G 238-53 in this plot. The narrow width of the instability strip and the presence of non-variables within form the two prominent features of this figure. We also note the paucity of DAVs in the middle of the instability strip.

### 4.1.1 Biases in candidate selection

We selected SDSS DAV candidates for high-speed photometry from those spectroscopically identified DA white dwarfs that lie in the temperature range 11000–12500 K. These temperature fits are derived by our SDSS collaborators using the spectral fitting technique outlined in Kleinman et al. (2004). Paper-I gives a discussion of other candidate selection methods used in our search for ZZ Ceti stars prior to the spectral fitting technique.

Our various science goals lead to some biases in selecting DAV candidates for observation. The hot DAV (hDAV) stars exhibit extreme amplitude and frequency stability (e.g. Kepler et al. 2000a; Mukadam et al. 2003a). We plan to search for reflex motion caused by orbiting planets around such stable pulsators (e.g. Kepler et al. 1991; Mukadam, Winget, & Kepler 2001; Winget et al. 2003). These stable clocks drift at their cooling rate; measuring the drift rate in the absence of orbital companions allows us to calibrate our evolutionary models. These models are useful in determining ages of the Galactic disk and halo using white dwarfs as chronometers (e.g. Winget et al. 1987; Hansen et al. 2002). Therefore, we preferentially choose to observe hDAV candidates in the range 11700–12300 K to increase the sample of known stable pulsators with both the above objectives in mind. This bias is partially compensated for, as hDAVs are harder to find (see section 2.2).

We also preferentially observe DAV candidates of extreme masses. Low mass ( $\log g \leq 7.6$ ) DAVs could well be helium core white dwarfs; pulsating He core white dwarfs should allow us to probe their equation of state. High mass ( $\log g \geq 8.5$ ) DAVs are potentially crystallized (Winget et al. 1997; Montgomery & Winget 1999), providing a test of the theory of crystallization in stellar plasma. Metcalfe, Montgomery, & Kanaan (2004) present strong evidence that the massive DAV, BPM 37093, is 90% crystallized.

The distribution of *chosen* DAV candidates also depends on the distribution of *available* DAV candidates. We have an additional bias due to the SDSS criteria in choosing candidates for spectroscopy. But a histogram of the available DAV candidates is consistent with a random distribution and does not reflect any systematic effects.

The non-uniform nature of the DAV distribution does not appear to be a candidate selection effect. However, we are in the domain of small number statistics since we observed only four DAV candidates in the range 11350–11500K. Of these, two are massive and consequently expected to be low amplitude pulsators (see section 2.2), making detection difficult. Our data are suggestive of a bimodal DAV distribution in temperature. We hope to investigate this issue further by observing additional DAV candidates in the range 11350–11500K with our collaborators.

#### 4.1.2 Non-uniform detection efficiency

The hDAVs show relatively few pulsation modes, with low amplitudes ( $\sim 0.1$ – $3\%$ ) and periods around 100–300 s. The cooler DAVs (cDAVs) typically show longer periods, around 600–1000 s, larger amplitudes (up to 30%), and greater amplitude variability (Kleinman et al. 1998). Massive pulsators show low amplitudes as a result of their high gravity ( $\log g \geq 8.6$ ). These distinct trends of the pulsation periods and amplitudes with temperature and  $\log g$  imply that the detection efficiency must also be a function of  $T_{\text{eff}}$  and  $\log g$ . The detection efficiency not only varies in the  $T_{\text{eff}}$ – $\log g$  plane, but is also dependent upon weather conditions and the magnitude of the DAV candidate. Furthermore, a ZZ Ceti star may have closely spaced modes or multiplet structure, both of which cause beating effects. Some of the non-variables in the instability strip could well be pulsators, that were in the destructive phase of their beating cycle

during the observing run. McGraw (1977) claimed BPM 37093 to be non-variable, but Kanaan et al. (1992) showed that it is a low amplitude variable with evident beating. Dolez, Vauclair, & Koester (1991) claimed the non-variability limit of G 30-20 to be a few mmag<sup>1</sup>, but Mukadam et al. (2002) found G 30-20 to be a beating variable with an amplitude of 13.8 mma<sup>2</sup>.

In order to address these issues systematically, we simulate light curves of real pulsators for different conditions and compute the resulting Fourier Transform (FT) to see if the signal is detectable above noise. We utilize the real periods and amplitudes, with randomly chosen phases (to sample the beat period), to simulate two hour long light curves<sup>3</sup>. We independently shuffle the magnitudes and average seeing conditions of real data on the DAVs. This ensures a realistic distribution for both these parameters. We randomly select a magnitude and seeing value from these distributions to simulate white noise, the amplitude of which is determined using a noise table based on real data. We compute a FT of the light curve and check if the star can be identified as a pulsator or if the signal was swamped by noise. We repeat this procedure 100 times for each DAV for different phases, magnitudes, and seeing values. Note that our noise simulation is not completely realistic, as it does not include effects due to variable seeing, gaps in the data due to clouds, and low frequency atmospheric noise. However, it does help us understand how the detection efficiency changes in the  $T_{\text{eff}}\text{-log } g$  plane.

We find that we are able to *rediscover* almost all of the average and low mass cDAVs in the hundred simulated attempts. The high mass ( $\log g \geq 8.6$ ) DAVs with a substantially lower amplitude are recovered with a  $\sim 70\%$  success rate. This implies that non-variables in Figure 4.1 in the region  $\log g \geq 8.6$  have

---

<sup>1</sup>One milli-magnitude (mmag) equals 0.1086% change in intensity.

<sup>2</sup>One milli modulation amplitude (mma) corresponds to 0.1% change in intensity.

<sup>3</sup>We generally observe the DAV candidates for two hours at a time when searching for new variables.

a 30% chance of being low amplitude variables. At the hot end of the instability strip, both low pulsation amplitude and beating can cause us to miss even the average or low mass hDAVs 35 out of 100 times.

Table 1 lists the non-variables in the instability strip along with their temperature,  $\log g$ , magnitude, and number of observing runs. The number after the NOV designation indicates the best non-variability limit in mma. Based on the simulations, we assign each non-variable a weight based on our estimate of the probability that the observed candidate is a genuine non-variable, and not a low-amplitude or beating pulsator. We use the non-variability limits to assign the weights 0.98, 0.95, 0.90, 0.85, 0.80, 0.70, and 0.60, for NOV1, NOV2, NOV3, NOV4, NOV5, NOV6, and NOV7 or higher, respectively. If the NOV is massive ( $\log g \geq 8.6$ ), then we additionally multiply its weight by a factor of 0.7. If the NOV is close to the blue edge of the strip, then we multiply by a factor of 0.65 to account for low amplitude and/or beating pulsators. However if the NOV has been observed multiple times, then it is unlikely to have been missed as a result of beating. In such a case, we multiply its weight only by a factor of 0.8 instead of 0.65, to allow for a possible low amplitude variable. We utilize these weights in section 6 to compute best-fit red and blue edges.

#### 4.1.3 Uncertainties in temperature and $\log g$ determinations

The true external uncertainties in the SDSS  $T_{\text{eff}}$  determinations are likely to be larger than listed in Paper-I. We expect that the external uncertainties are of the order of 300K. However, the uncertainty that is relevant in determining the width and purity of the instability strip defined by a homogeneous ensemble is the internal uncertainty.

The low signal-to-noise of the blue end of the SDSS spectra reduces the reliability of the  $\log g$  values. The H8 and H9 lines depend mostly on gravity

Table 4.1: Non-variables in the ZZ Ceti instability strip

Object	Limit	Obs. runs	SDSS $T_{\text{eff}}$ (K)	SDSS $\log g$	$g$	Weight
WD0037+0031	NOV5	2	$10960 \pm 050$	$8.41 \pm 0.03$	17.5	0.80
WD0050-0023	NOV6	2	$11490 \pm 090$	$8.98 \pm 0.03$	18.8	0.50
WD0222-0100	NOV3	4	$12060 \pm 120$	$8.12 \pm 0.05$	18.0	0.60
WD0303-0808	NOV4	2	$11400 \pm 110$	$8.49 \pm 0.06$	18.8	0.85
WD0345-0036	NOV5	3	$11430 \pm 150$	$7.76 \pm 0.09$	19.0	0.80
WD0747+2503	NOV3	3	$11050 \pm 110$	$7.93 \pm 0.08$	18.4	0.90
WD0853+0005	NOV4	2	$11750 \pm 110$	$8.11 \pm 0.06$	18.2	0.55
WD1031+6122	NOV4	2	$11480 \pm 180$	$7.68 \pm 0.11$	18.7	0.85
WD1136-0136	NOV2	1	$11710 \pm 070$	$7.96 \pm 0.04$	17.8	0.62
WD1337+0104	NOV4	2	$11830 \pm 210$	$8.39 \pm 0.11$	18.6	0.60
WD1338-0023	NOV4	1	$11650 \pm 090$	$8.08 \pm 0.05$	17.1	0.85
WD1342-0159	NOV4	2	$11320 \pm 160$	$8.42 \pm 0.09$	18.8	0.85
WD1345+0328	NOV6	1	$11620 \pm 140$	$7.80 \pm 0.08$	18.6	0.70
WD1432+0146	NOV5	1	$11290 \pm 070$	$8.23 \pm 0.06$	17.5	0.80
WD1443-0006	NOV5	1	$11960 \pm 150$	$7.87 \pm 0.07$	18.7	0.80
WD1503-0052	NOV4	3	$11600 \pm 130$	$8.21 \pm 0.07$	18.4	0.85
WD1658+3638	NOV4	4	$11110 \pm 120$	$8.36 \pm 0.09$	19.2	0.85
WD1726+5331	NOV7	1	$11000 \pm 110$	$8.23 \pm 0.08$	18.8	0.60

because neighboring atoms predominantly affect higher energy levels (Hummer & Mihalas 1970), and their density depends on  $\log g$ . The external uncertainties in  $\log g$  for our ensemble may be as high as 0.1, twice that of the estimated uncertainty for the Bergeron et al. (2004) sample. We find an average  $\log g$  of  $\simeq 8.10$  for our sample of 31 objects, while the 36 objects in Bergeron et al. (2004) average at  $\simeq 8.11$ . G 238-53 is common to both samples; Bergeron et al. (2004) derive  $T_{\text{eff}}=11890\text{ K}$  and  $\log g=7.91$ , while the SDSS determination places G 238-53 at  $T_{\text{eff}} = 11820 \pm 50$  and  $\log g = 8.02 \pm 0.02$ . The temperature values agree within  $1\sigma$  uncertainties. Temperature is mainly determined by the continuum and the  $H\alpha$ ,  $H\beta$ , and  $H\gamma$  lines; the low S/N at the blue end of the SDSS spectra has a reduced effect on temperature determinations. The well calibrated continuum, extending from 3800–9200 Å provides an accurate temperature determination.

The gradual change in mean mass as a function of temperature for the SDSS DA white dwarf fits is addressed in Kleinman et al. (2004), and Figure 7 of their paper shows a quantitative measure of this systematic effect. The increase in  $\log g$  across the width of the instability strip is only  $\sim 0.02$ , and implies that our determinations of cDAV masses are negligibly higher. These systematic effects are small in the range of the ZZ Ceti instability strip, and cannot produce either the narrow width or the impurity of the observed strip.

We conduct a simple Monte Carlo simulation to estimate the internal  $T_{\text{eff}}$  uncertainties of our ensemble. Using the observed pulsation characteristics, we can separate the DAVs into two classes: hDAVs and cDAVs (see section 2.2). We show the observed distribution of the hDAVs and cDAVs in the lowest panel of Figure 4.2. These distributions are distinct, except for 3 objects. Based on the empirical picture, we conceive that the underlying DAV distribution may look similar to that shown in the topmost panel of Figure 4.2. We perform a Monte

Carlo simulation, drawing hDAVs and cDAVs randomly from the expected DAV distribution, and using Gaussian uncertainties with  $\sigma = 300$  K. We show the resulting distribution in the second panel; the large uncertainties cause significant overlap between the cDAVs and hDAVs, swamping the central gap. We perform a similar simulation with  $\sigma = 200$  K (third panel), and it compares well with the observed distribution considering the small numbers of the empirical distribution. This suggests that the internal uncertainties in effective temperature for our ensemble are  $\sigma \leq 200$  K per object, provided we believe that the hDAVs and cDAVs each span a range of at least 300 K. Note that the internal uncertainties for a few individual objects maybe as large as 250–300 K.

## 4.2 Probing the non-uniform DAV distribution using pulsation periods

The mean or dominant period of a pulsator is an indicator of its effective temperature (see section 2.2). This asteroseismological relation is not highly sensitive, but it provides a technique independent of spectroscopy to study the DAV temperature distribution. We show the distribution of the dominant periods of the SDSS DAVs in Figure 4.3. The top right panel in Figure 4.3 shows the number of DAVs per period interval and is suggestive of a bimodal distribution; this increases the likelihood that the dearth of DAVs near the center of the strip is real<sup>4</sup>.

---

<sup>4</sup>We made a similar plot using the dominant periods for the 36 previously known DAVs, but did not find any evidence for a bimodal distribution. Determining the dominant period of the 36 ZZ Ceti stars in the literature proved to be difficult and quite inhomogeneous compared to our own data on the SDSS DAVs.

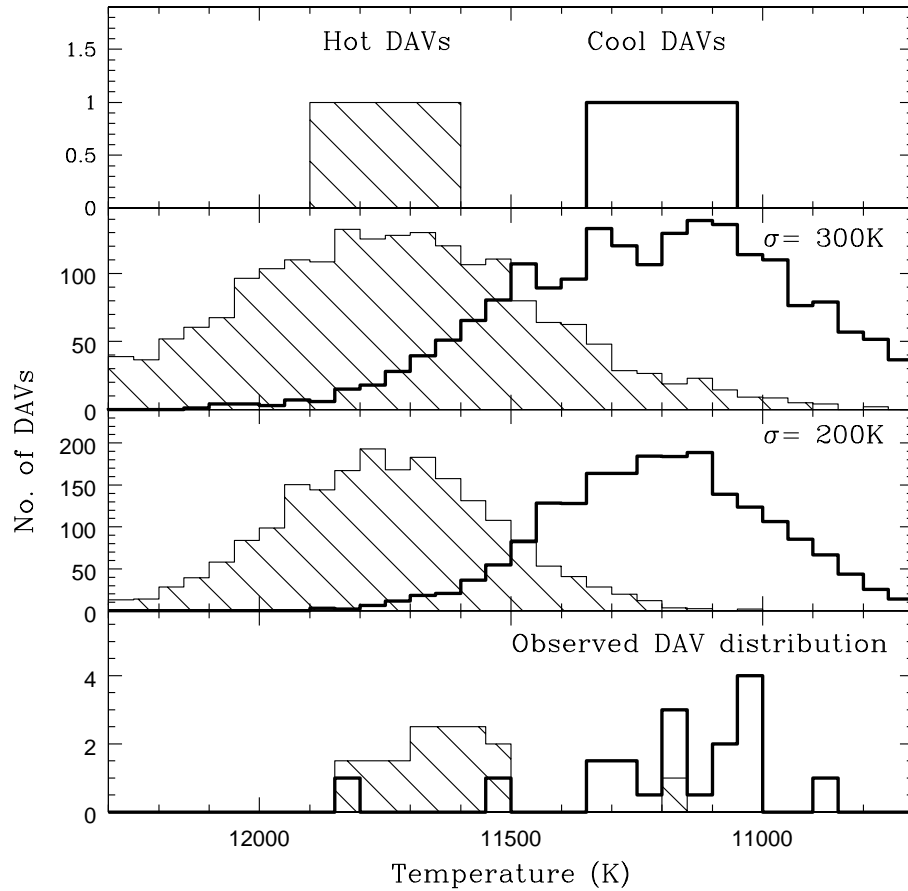


Figure 4.2: We choose hDAVs and cDAVs from the distributions shown in the top panel, and use a Gaussian error function with  $\sigma = 300\text{K}$  to compute the distributions shown in the second panel. We also similarly determine a DAV distribution with internal uncertainties of order 200 K, shown in the third panel. Comparing the empirical DAV distribution, shown in the bottom panel, to the synthetic computations, we conclude that the average internal uncertainty for our ensemble is  $\sigma \leq 200\text{K}$ .

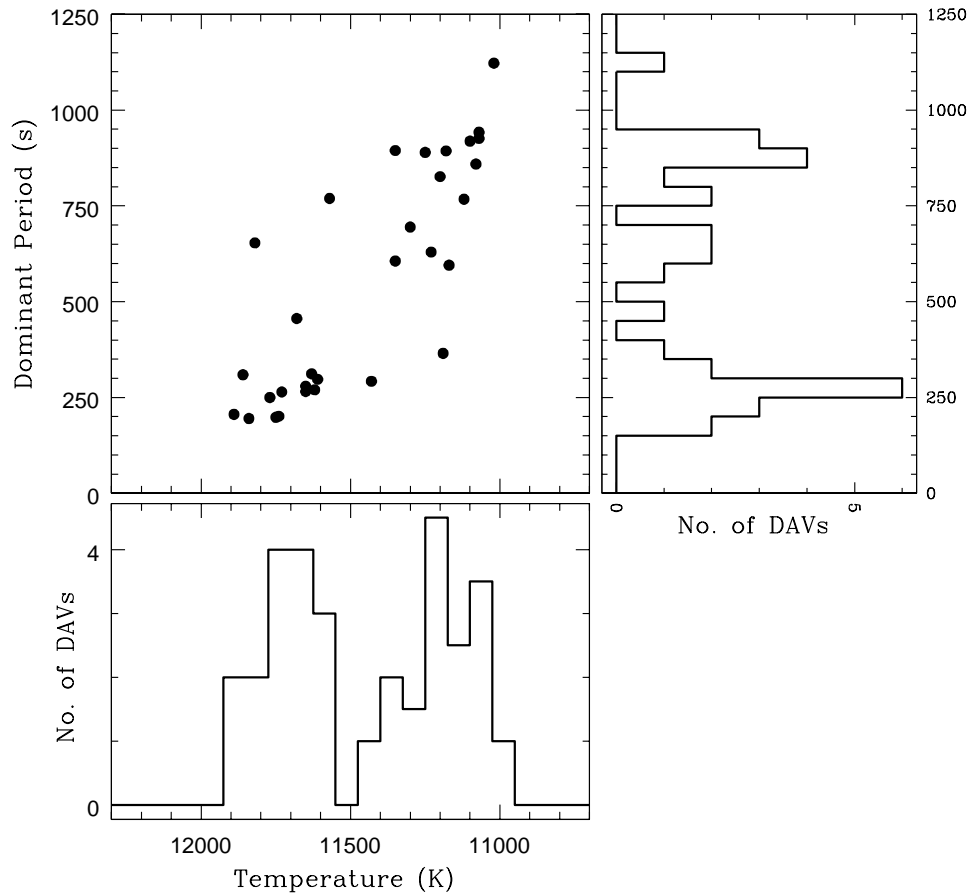


Figure 4.3: Period distribution of the SDSS DAVs as a function of temperature. The top left panel exhibits two distinct clumps consisting of the short period hDAVs and the long period cDAVs. The dominant period of a DAV is a seismological temperature indicator and the histogram shown in the top right panel is suggestive of a bimodal distribution.

### 4.3 Questioning the impurity of the instability strip

Non-variables in the instability strip imply that all DA white dwarfs do not evolve in the same way. This notion has a severe implication: decoding the inner structure of a DAV will no longer imply that we can use the results towards understanding DA white dwarfs in general. Hence we question our findings, and conduct simulations to verify our results. Although we estimate the internal  $T_{\text{eff}}$  uncertainties to be at most 200 K in section 2.3, we will conservatively assume  $\sigma = 300$  K for all subsequent calculations.

The SDSS spectra do not show any evidence of a binary companion for all the non-variables within the instability strip. Also, we used D. Koester's model atmospheres to ascertain that the SDSS algorithm had chosen a solution consistent with the photometric colors ( $u - g$ ,  $g - r$ ) in every case.

We now conduct a Monte Carlo simulation assuming a pure instability strip enclosed by non-variables, as shown in the top panel of Figure 4.4. Note that we have not included a  $\log g$  dependence in our model, as we expect it to be a smaller effect than what we are about to demonstrate. We choose non-variables from outside the strip and add uncertainties chosen randomly from a Gaussian error distribution with  $\sigma = 300$  K to determine the NOV distribution shown in the middle panel. We find that although non-variables leak into the strip, they are found mostly at the outer edges and their number tails off within the strip. The observed NOV distribution (bottom panel) does not show any signs of tailing off within the instability strip. Rather, it displays the same number of non-variables at the edges as in the center of the strip. This suggests that the instability strip is impure, and that all the NOVs within the instability strip did not leak in due to large  $T_{\text{eff}}$  uncertainties. We carried out these simulations several times to verify these results.

We compute the likelihood that the instability strip is pure based on the

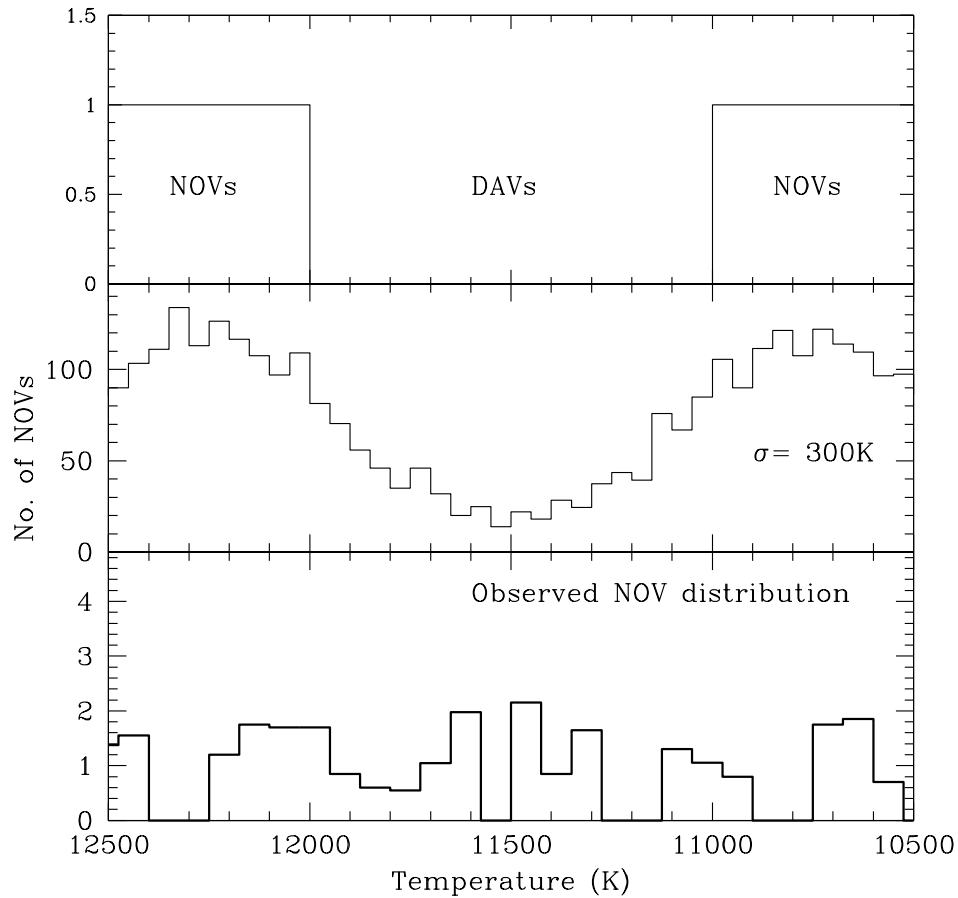


Figure 4.4: Assuming a pure instability strip as shown in the top panel, we use a Monte Carlo simulation assuming a Gaussian distribution for the internal uncertainties with  $\sigma = 300\text{K}$  to determine the expected distribution for non-variables within the strip. The observed NOV distribution is flat, and shows no signs of tailing off within the strip. The observed distribution shows the same number of non-variables at the edges as in the center of the instability strip.

following two criteria. There are two ways in which a non-variable can disappear from the instability strip: subsequent observations show it is a (low amplitude) variable or the internal uncertainties in  $T_{\text{eff}}$  prove to be large enough to allow the possibility that it may have leaked into the strip. Table 1 lists our estimates of the probabilities that the NOV's found within the strip are genuine non-variables. The chance that NOV's may have leaked into the strip due to large internal uncertainties  $\sigma = 300 \text{ K}$  are: 0.35 for WD0037+0031, 0.18 for WD0050-0023, 0.13 for WD0303-0808, 0.04 for WD0345-0036, 0.25 for WD0747+2503, 0.42 for WD0853+0005, 0.15 for WD1031+6122, 0.38 for WD1136-0136, 0.31 for WD1338-0023, 0.11 for WD1342-0159, 0.28 for WD1345+0328, 0.13 for WD1432+0146, 0.25 for WD1503-0052, 0.20 for WD1658+3638, and 0.31 for WD1726+5331. The probability that each of the above non-variables disappear from the instability strip is then: 0.48, 0.59, 0.26, 0.23, 0.33, 0.68, 0.28, 0.62, 0.41, 0.24, 0.50, 0.30, 0.36, 0.32, and 0.59 respectively.

Three or four of the above non-variables may have an inclination angle that reduces the observed amplitude below the detection threshold. Instead of calculating various permutations, we will evaluate the likelihood of the worst case scenario. Let four NOV's that have the least chance of disappearing from the instability strip be the ones that have an unsuitable inclination angle for observing pulsations. In that case, the chance that the instability strip is pure is 0.004%. The impurity of the instability strip suggests that parameters other than just the effective temperature and  $\log g$  play a crucial role in deciding the fate of a DA white dwarf, i.e., whether it will pulsate or not.

#### 4.4 Narrow width of the ZZ Ceti strip

Computing the width of the instability strip using the effective temperatures of the hottest and coolest pulsators gives us a value, independent of our concep-

tion of the shape of the ZZ Ceti strip. Determining whether the blue and red edges continue to be linear for very high ( $\log g \geq 8.5$ ) or very low ( $\log g \leq 7.7$ ) masses is presently not possible with either our sample or the Bergeron et al. (2004) sample. The width of the instability strip calculated from the empirical edges at different values of  $\log g$  involves additional uncertainties from our linear visualization of the edges.

The empirical SDSS DAV instability strip spans from the hottest objects G 238-53 and WD0825+4119, both at  $T_{\text{eff}} = 11820 \pm 170$  K, to the coolest object WD1732+5905 at  $10860 \pm 100$  K. This span of  $960 \pm 200$  K is considerably smaller than the 1500 K width in the literature (Bergeron et al. 1995; Koester & Allard 2000). The hottest pulsator in the Bergeron et al. (2004) sample is G 226-29 at 12460 K and the coolest pulsators are G 30-20 and BPM 24754 at 11070 K. The extent of the instability strip for the Bergeron et al. (2004) sample is then  $\sim 1400$  K.

The drift rates of the stable ZZ Ceti pulsators give us a means of measuring their cooling rates (e.g. Kepler et al. 2000a, Mukadam et al. 2003a). Our present evolutionary cooling rates from such pulsators suggest that given a width of 950 K, a  $0.6 M_{\odot}$  ZZ Ceti star may spend  $\sim 10^8$  yr traversing the instability strip. This agrees with theoretical calculations by Wood (1995) and Bradley, Winget, & Wood (1992). The narrow width constrains our understanding of the evolution of ZZ Ceti stars.

## 4.5 Empirical blue and red edges

We draw blue and red edges around the DAV distribution that enclose all of the variables. This is shown in Figure 4.5 by the solid line for the blue edge and the line with dots and dashes for the red edge. These edges also include non-variables within the instability strip.

We now demonstrate an innovative statistical approach to find the best-fit blue and red edges that maximize the number of variables and minimize the number of non-variables enclosed within the strip. To the best of our knowledge, no standard technique can be used to solve this interesting statistical problem. Our statistical approach has two advantages: we are accounting for the uncertainties in temperature and  $\log g$  values and we are utilizing most of the variables and non-variables in our determination rather than just a handful close to the edge.

This problem has essentially two independent sources of uncertainties: the uncertainties in temperature and  $\log g$  that shift the location of a star in the  $T_{\text{eff}}\text{-}\log g$  plane and the uncertainty concerning the genuine nature of a non-variable. Pulsators masquerading as non-variables can significantly alter our determination of the blue and red edges. Hence, we assign different weights to DAVs and NOVs. Since the DAVs are confirmed variables, we assign them a unit weight. We use the non-variability limit to decide the weight of all the NOVs that lie outside the empirical ZZ Ceti strip, as in section 2.2, while we assign the weights listed in Table 1 for NOVs within the instability strip.

#### 4.5.1 Technique

We construct a grid in  $T_{\text{eff}}$  and  $\log g$  space in the respective ranges 9000–14000K and 6.0–10.5 with resolutions of 50K and 0.05. For each point in the grid, we consider possible blue and red edges that vary in inclination angle relative to the temperature axis from 15 degrees to 165 degrees by half a degree with each successive iteration.

For each point of the grid, and for each possible blue edge, we compute a net count as follows: DAVs on the cooler side of the edge count as +1 each and on the hotter side count as  $-1$  each. NOVs on the hotter side of the edge

count as  $+w$ , and on the cooler side as  $-w$  each, where  $w$  is the weight of the corresponding NOV. To determine the best blue edge, we consider all DAVs and NOVs that satisfy  $T_{\text{eff}} \geq 11500$  K. This ensures that the NOVs close to and beyond the red edge do not influence the determination of the blue edge. If the DAV or NOV is within  $3\sigma$  of the edge, then we determine the net chance that it lies on the hot or cool side of the edge, assuming a Gaussian uncertainty distribution. We multiply this chance with the count for that object, before adding it to the total count. An effect of this choice is that the best edge is determined by the global distribution of DAVs and NOVs, rather than the few close to the edge.

Similarly, we determine the best red edge at each point of the grid by counting DAVs on the hotter side of the edge as  $+1$  and NOVs on its cooler side as  $+w$ , and vice versa. We consider all DAVs and NOVs within the instability strip and cooler than 11820 K to compute the best red edge. If the DAV or NOV is within  $3\sigma$  of the red edge, then its contribution is a fraction of the above, depending on the probability that it lies on one side of the edge or the other.

To test our statistical approach, we input the  $T_{\text{eff}}$  and  $\log g$  determinations of the previously known DAVs from Bergeron et al. (2004) along with the SDSS NOVs. The resulting red and blue edges are fairly similar to those of Bergeron et al. (2004), and we attribute most of the difference to using an independent set of NOVs<sup>5</sup>. Figure 4.5 shows our best-fit for the red edge and our constraint on the blue edge using our statistical approach.

$$\log g = 0.0043T_{\text{eff}} - 43.48 \qquad \text{Best fit blue edge} \qquad (4.1)$$

$$\log g = 0.0010T_{\text{eff}} - 3.01 \qquad \text{Best fit red edge} \qquad (4.2)$$

---

<sup>5</sup>We cannot use the same set of non-variables as Bergeron et al. (2004) as they did not publish the non-variable parameters or identifications.

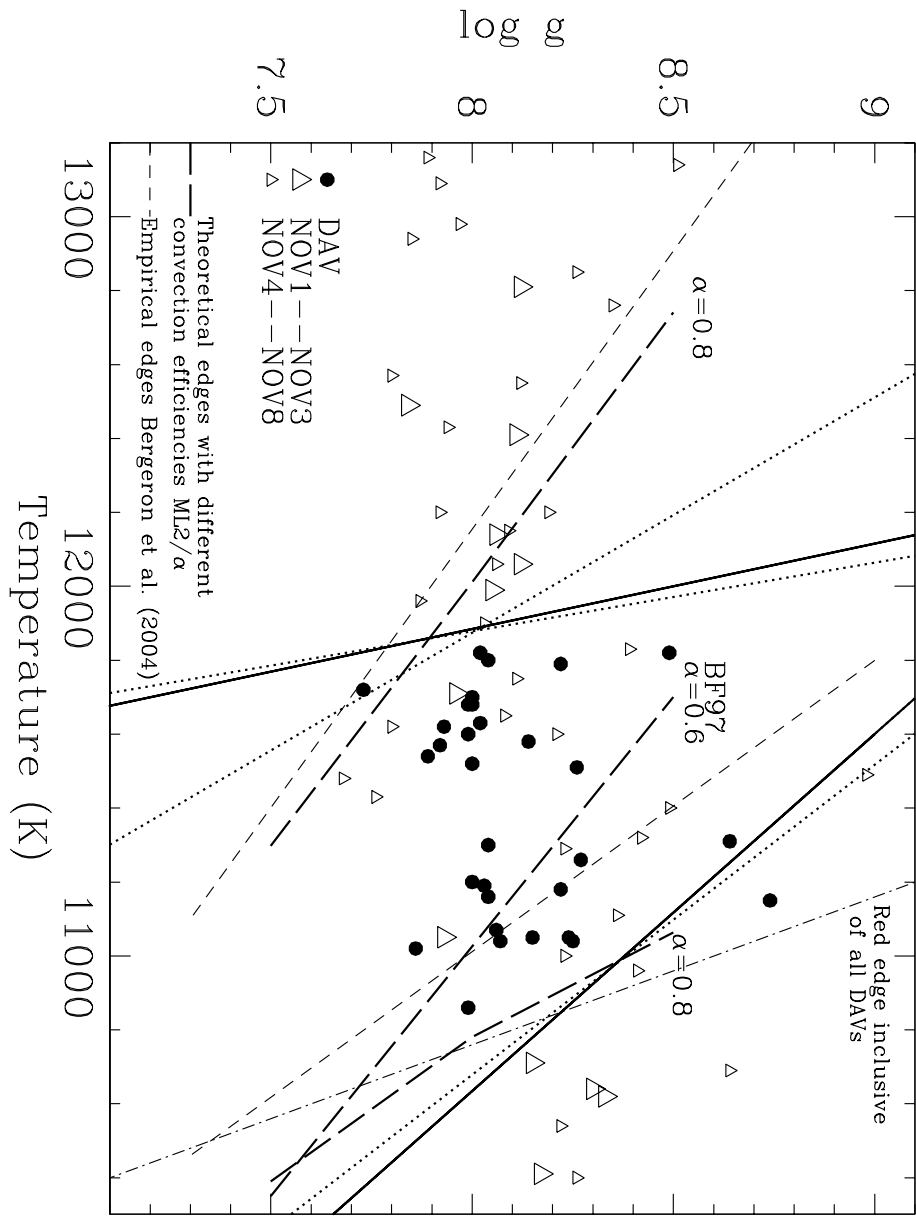


Figure 4.5: Statistical determination of the blue and red edges (solid lines) from the homogeneous set of 31 SDSS DAVs with an estimated  $1\sigma$  uncertainty (dotted lines; red edge coincides with one of the dotted lines). We also show a red edge inclusive of all DAVs (dash-dotted line). We show the empirical edges from Bergeron et al. (2004) as dashed lines, and the theoretical blue edge from Brassard & Fontaine (1997;  $ML2/\alpha=0.6$ ) for comparison. We show Mike Montgomery’s computations (Montgomery 2004; private communication) of the theoretical edges assuming  $ML2/\alpha=0.8$  convection, based on the convective driving theory of Wu & Goldreich (1999).

## 4.5.2 Estimating the uncertainties

The dominant effect that dictates the uncertainties in the slope ( $\log g$  dependence) and location (in temperature) of the edges arises as a result of the unreliable nature of the NOVs. Are they genuine NOVs or low amplitude pulsators? Our simulations in section 2.2 show that we miss 30% of high mass pulsators due to their low amplitude. We estimate this should introduce an uncertainty of order 0.2 in the total count for both the red and blue edges. The NOVs close to the blue edge, but within the instability strip, can introduce additional uncertainties in our determination. We add these independent sources of uncertainty in quadrature to obtain an estimated  $1\sigma$  uncertainty of 0.6 for the red edge and 0.4 for the blue edge. We show these as dotted lines in Figure 4.5. Our estimates of the  $1\sigma$  uncertainties clearly show that the red edge is well constrained, and the slope of the blue edge is not.

For the blue edge, we determine:

$$\log g = 0.0016T_{\text{eff}} - 10.64 \quad +1\sigma \text{ away from the blue edge} \quad (4.3)$$

$$\log g = 0.0037T_{\text{eff}} - 36.35 \quad -1\sigma \text{ away from the blue edge} \quad (4.4)$$

For the red edge, we determine:

$$\log g = 0.0012T_{\text{eff}} - 4.73 \quad +1\sigma \text{ away from the red edge} \quad (4.5)$$

$$\log g = 0.0010T_{\text{eff}} - 3.01 \quad -1\sigma \text{ away from the red edge} \quad (4.6)$$

Note that we already account for the uncertainties in  $T_{\text{eff}}$  and  $\log g$  in determining the red and blue edges. The unreliability of these uncertainties contributes towards an uncertainty in the slope of the edges; this turns out to be a negligible second order effect.

### 4.5.3 Comparison with empirical edges

We show the empirical blue and red edges from Bergeron et al. (2004) in Figure 4.5 for comparison. The slopes of the red edges from both samples agree within the uncertainties. But our constraint on the blue edge differs significantly from that of Bergeron et al. (2004) and Kepler et al. (2000b), and suggests that the dependence on mass is less severe.

The mean temperature of our sample is 11400 K, while the mean temperature for the Bergeron et al. (2004) sample is 11630 K. The observed extent of our instability strip defined by 31 objects spans 10850–11800 K, while that of Bergeron et al. (2004) spans 11070–12460 K<sup>6</sup>. We can consider these values to imply a relative shift of  $\sim 200$  K between our sample and that of Bergeron et al. (2004).

We would also like to point out that our sample is magnitude limited and reaches out to  $g = 19.3$ . We are effectively sampling a distinct population of stars as most of our sample lies between 200–250 pc, while the Bergeron et al. (2004) sample is within 100 pc.

### 4.5.4 Comparison with theoretical edges

In Figure 4.5, we show the theoretical blue edge from Brassard & Fontaine (1997) due to the traditional radiative driving mechanism; they use a  $ML^2/\alpha = 0.6$  prescription for convection in their equilibrium models. We also show Mike Montgomery’s computations (Montgomery 2004; private communication) of the blue *and* red edges from the convective driving theory of Wu & Goldreich (Brickhill 1991; Wu 1998; Wu & Goldreich 1999), assuming  $ML^2/\alpha = 0.8$  for convection.

We see that the blue edges of the two theories are essentially the same,

---

<sup>6</sup>Excluding G 226-29, the Bergeron et al. (2004) sample spans a width of 1060 K from 11070 K to 12130 K.

and would nearly coincide if the mixing-length parameter were tuned. To obtain the red edge of Wu & Goldreich, Mike Montgomery made the following assumptions: (1) the relative flux variation at the base of the convection zone is no larger than 50%, (2) the period of a representative red edge mode is 1000 s, and (3) the detection limit for intensity variations is 1 mma. Within this theory, the convection zone attenuates the flux at its base by a factor of  $\sim \omega\tau_C$ , where  $\tau_C$  is the thermal response time of the convection zone, so we have adjusted  $\tau_C$  such that the surface amplitude  $0.5/(\omega\tau_C) \sim 10^{-3}$ , equal to the detection threshold.

The observed distribution of variables and non-variables suggests that the mass dependence of the blue edge is less severe than predicted by the models. Both the slope and the location of the red edge we calculate are consistent with the observed variables and non-variables within the uncertainties.

## 4.6 Conclusion

Using a statistically significant and truly homogeneous set of 31 ZZ Ceti spectra, we find a narrow instability strip between 10850K and 11800K. We also find non-variables within the strip and compute the likelihood that the instability strip is pure to be  $\sim 0.004\%$ . Obtaining higher signal-to-noise spectra of all the SDSS and non-SDSS DAVs as well as non-variables in the ZZ Ceti strip is crucial to a better determination of the width and edges of the instability strip, and in investigating the purity of the instability strip. This should help constrain our understanding of pulsations in ZZ Ceti stars.

The DAV distribution shows a scarcity of DAVs in the range 11350–11500K. After exploring various possible causes for such a bimodal, non-uniform distribution, we are still not entirely confident that it is real. The data at hand are suggestive that the non-uniformity of the DAV distribution is real, and stayed hidden from us for decades due to the inhomogeneity of the spectra

of the previously known DAVs. However, we are in the domain of small number statistics and unless we investigate additional targets in the middle of the strip, we cannot be confident that the bimodal distribution is not an artifact in our data.

## Chapter 5

# ZZ Ceti Ensemble characteristics

### 5.1 Pulsations in ZZ Ceti models

Pulsations in ZZ Ceti models (and in stars) are self-driven oscillations. Stochastic noise frequencies coincident with the eigenfrequencies are amplified by the driving mechanism to observable amplitudes. The driving frequency is governed by the thermal timescale at the base of the hydrogen partial ionization zone. The blue edge of the ZZ Ceti instability strip occurs when the star is cool enough to have a hydrogen partial ionization zone, sufficiently deep to excite global pulsations.

The hydrogen partial ionization zone constitutes a region of recombination, where both free-free and bound-free opacities are significant. It is not only a region of higher opacity, but it has the ability to modulate the degree of ionization as it expands or contracts, more than any other layer in the star.

A stochastic nonradial expansion, occurring locally in the partial ionization zone, will reduce the density, and hence the degree of ionization in that region. This will allow that portion of the star to cool easily. The restoring force of buoyancy will subsequently cause this region to contract, increasing the den-

sity. As the density is increasing, the degree of ionization continues to increase. This reduces the flow of energy through this region, causing it to heat up.

### 5.1.1 Growth of amplitude

Why should the amplitude of such stochastic processes increase? A source of opacity provides a contracting region a method of stowing away energy, without a significant increase in temperature. This allows the region to contract some more. In the downstroke, as a region of the partial ionization zone is contracting, the degree of ionization increases. This enables it to continue contracting past density maximum, until it reaches pressure maximum. Similarly, when the region is expanding, the degree of recombination increases. The amplitude continues to grow with each passing cycle. This is similar to a child pumping energy into a swing; the child straightens his/her legs while swinging up, and folds his/her legs while swinging down, increasing the amplitude in both directions. The energy absorbed by the partial ionization zone between density maximum and pressure maximum is a measure of the energy pumped into the pulsation mode. This additional boost will cause the region to expand more during the upstroke. Recombination during expansion implies that pressure minimum will follow density minimum. The additional energy that flows through the region between the density and pressure minima serves as another boost, increasing the amplitude of pulsation.

Is the presence of a partial ionization zone the only requirement for a star to pulsate? In order for a region to drive, it must absorb energy at maximum compression. If the expansion and contraction is adiabatic, then the region cannot pump energy into pulsation amplitudes. The partial ionization should be significantly above the adiabatic-nonadiabatic transition zone, in the nonadiabatic regime, in order to drive.

Can any region in the nonadiabatic domain drive pulsations? A stochastic expansion or contraction will not modulate the degree of ionization as much for any region in the nonadiabatic domain, as for a region in the partial ionization zone. Hence, the same amount of energy flows essentially unmodulated and radially through the system. Higher pulsation amplitude is related to higher modulation of the degree of ionization, and hence to the size of the partial ionization zone.

What limits the amplitude growth? If a region loses heat during compression, then it serves as an energy sink or a damping mechanism. In the downstroke, energy is radiated from the heated regions. Radiative damping then serves to limit the pulsation amplitude.

### **5.1.2 Fluid motions in the star**

Why are these pulsations non-radial? The star requires substantially more energy to expand against gravity for radial displacements compared to nonradial motions. The nonradial expansion necessitates that if some regions of the partial ionization zone are expanding, others must be contracting at the same time. The star has corresponding bright and dark regions on the surface. Frequencies with a phase mismatch cancel each other, and their amplitude do not grow beyond that of white noise.

Are these fluid motions restricted to the surface? Similar to ripples in water, these non-radial motions penetrate below the surface, although with reducing amplitude. Montgomery & Winget (1999) and Montgomery, Metcalfe, & Winget (2003) showed that pulsations probe up to the inner 99% of the star. Even though the amplitude in the core is extremely small, it is dense and massive enough that modes are sensitive to changes in the core conditions. We can learn more about the stellar interior from white dwarf variables than we can

from some other classes of variables, because white dwarfs are not as centrally condensed.

## 5.2 Trends across the instability strip

The distinct behavior of the pulsation periods and amplitudes of the ZZ Ceti stars as a function of temperature has been discussed in several papers, e.g. McGraw et al. (1981), Winget & Fontaine (1982), and was systematically demonstrated for a significant sample of DAs by Clemens (1993) and more recently by Kanaan, Kepler, & Winget (2002). We now demonstrate and discuss these trends for the newly discovered DAVs.

### 5.2.1 Observed pulsation periods

The driving frequency in ZZ Ceti models is governed by the thermal timescale at the base of the hydrogen partial ionization zone. As the star cools, the base of the partial ionization zone moves deeper in the star, and the thermal timescale increases. Hence, we expect cool ZZ Ceti stars to show longer periods compared to the hot ZZ Ceti variables.

Figure 5.1 confirms this expectation; it shows a clear increase in the mean period, weighted by the observed amplitude, as the star cools across the instability strip. The bimodal distribution that we see in Figure 4.3 is not evident in this figure. This is perhaps because there are systematic differences between the SDSS  $T_{\text{eff}}$  and  $\log g$  determinations and those taken from Bergeron et al. (2004). Additionally, larger internal inhomogeneities in the Bergeron et al. (2004) sample could be swamping out the underlying bimodal pattern.

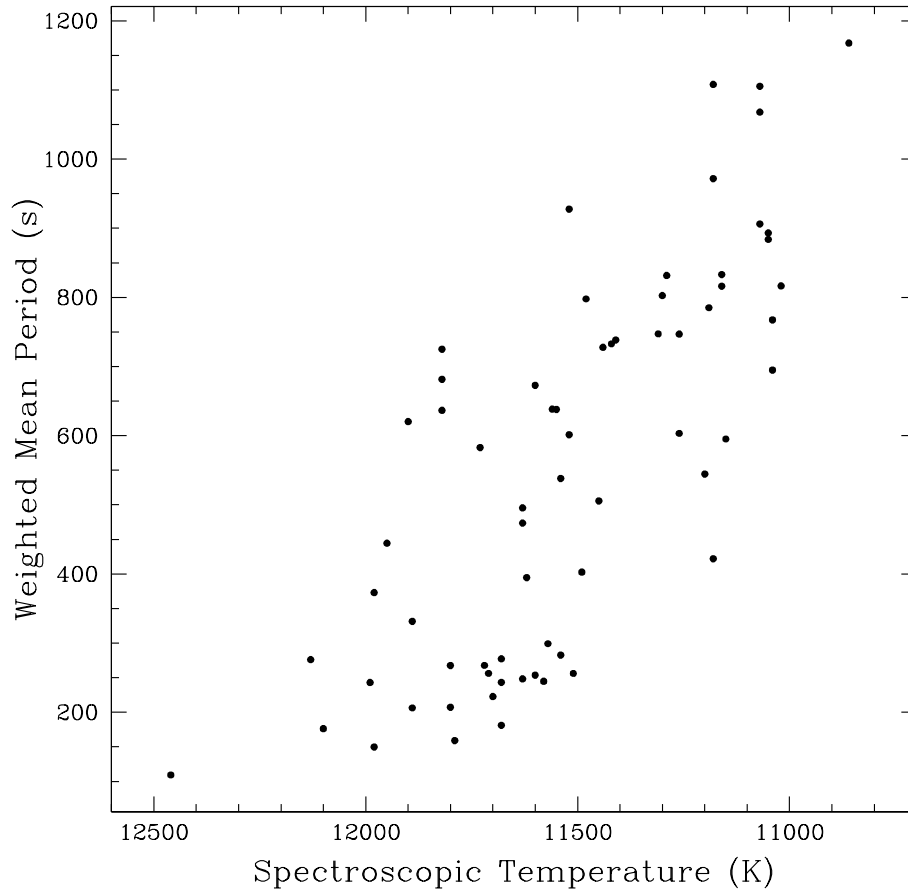


Figure 5.1: We show the weighted mean period of 67 ZZ Ceti stars vs their spectroscopic temperature; each period was weighted by the observed amplitude. The figure clearly indicates an increase in the pulsation period as DAVs cool across the ZZ Ceti strip.

### 5.2.2 Observed pulsation amplitudes

As the base of the partial ionization zone moves deeper in the star, it increases in size. As a result, we expect an increase in pulsation amplitudes as the star cools across the DAV instability strip. Figure 5.2 shows the average amplitude of 67 DAVs as a function of their spectroscopic temperature. The outer envelope of these plots is a better indicator of the intrinsic pulsation amplitude, and shows an increase as we move from the blue edge to the red edge of the instability strip.

The observed amplitude in a ZZ Ceti star can be lower than the intrinsic amplitude due to inclination angle effects, geometric cancellation, and limb darkening. We are not able to resolve the disk of the star from Earth. Hence the observed amplitude of each pulsation mode is lower due to a disk-averaging effect, depending on the angle of inclination. Therefore, we have a higher probability of detecting  $\ell=1$  modes than  $\ell=2$  modes, and so on. At ultraviolet (UV) wavelengths, the increased limb darkening decreases the contribution of zones near the limb. Hence, modes of higher  $\ell$  are canceled less effectively in the UV compared to the low  $\ell$  modes (Robinson, Kepler, & Nather 1982). The intrinsic amplitude also depends on the mass of the star. We indicate the three massive pulsators, BPM 37093, WD0923+0120, and WD1711+6541 with hollow boxes to show that their high gravity is responsible for their low pulsation amplitudes. Nonradial g-modes have a non-negligible radial component, the amplitude of which scales with stellar mass and plays a role in dictating the amplitude of the nonradial component.

Figure 5.3 shows the mean amplitude of the 30 SDSS DAVs as a function of their spectroscopic temperature. This plot exhibits a fairly homogeneous sample, with consistent data reductions, and we find reduced scatter compared to Figure 5.2. Figure 5.2 shows a decline in amplitude near the red edge of

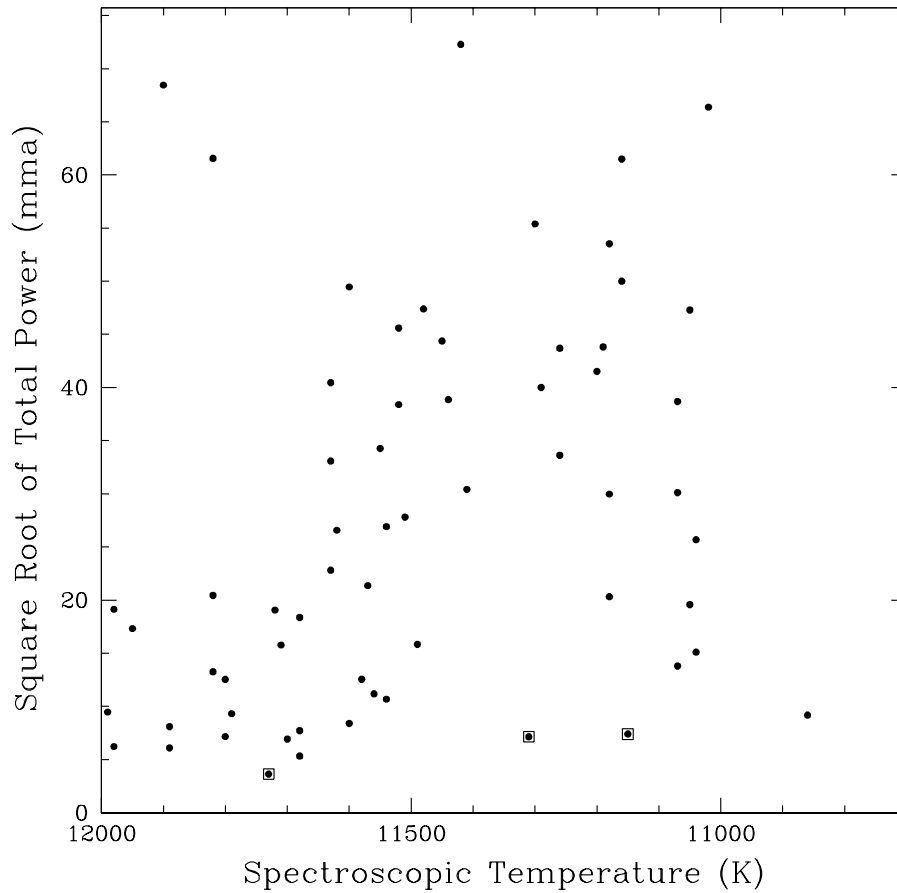


Figure 5.2: We show the square root of the total power of 67 ZZ Ceti stars vs their spectroscopic temperature. There is clearly an increase in the average power, as the ZZ Ceti stars cool towards the red edge of the instability strip. The scatter in this diagram comes chiefly from different inclination angles and masses that alter the observed amplitude, and the outer envelope is indicative of the intrinsic average amplitude of the star. The points enclosed by a hollow square indicate the massive, and consequently low amplitude pulsators, WD1711+6541, WD0923+0120, and BPM 37093.

the instability strip, if we believe that the six low amplitude pulsators close to the red edge do not all have unfavorable inclination angles. If this is true, then this is the first observational evidence that the red edge is not abrupt, and that pulsation amplitudes decline close to the red edge, before the star stops pulsating.

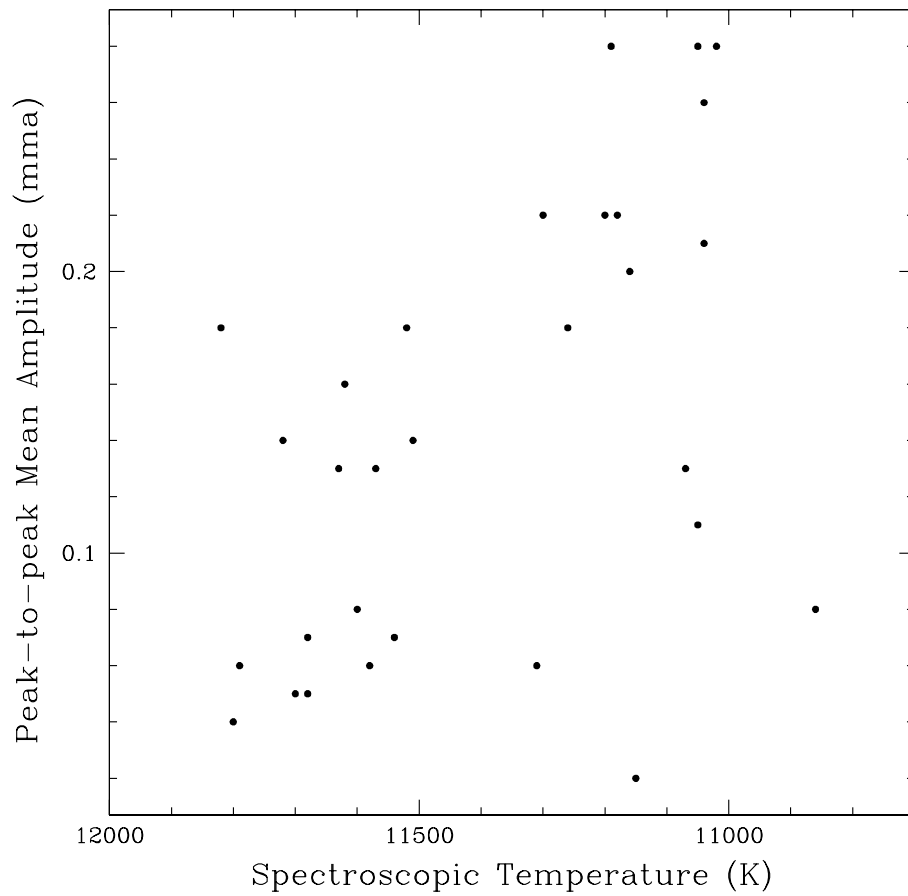
### 5.2.3 Mode density

For a given  $\ell$ , increasing the radial overtone increases the period. The period spacing for nonradial g-modes reduces asymptotically. The density of available eigenmodes as a function of period changes quite dramatically between the blue and red edges of the ZZ Ceti strip. At the red edge, multiple eigenmodes have a frequency close to the driving frequency and are excitable. While we expect to observe only a few modes close to the blue edge due to the relatively larger spacing.

## 5.3 Drifting eigenmodes

Kepler et al. (2000a) conclude that the evolutionary  $\dot{P}$  is dictated by the rate of cooling for the DAV stars, and contraction is not significant in the temperature range of the DAV instability strip. O'Donoghue & Warner (1987), Kepler et al. (2000a), and Mukadam et al. (2003a) have constrained the unidirectional drift rate of the 192 s mode in L 19-2, 215 s mode in G 117-B15A, and 213 s mode in R 548 respectively to be smaller than a few  $\times 10^{-15}$  s/s. To put this number in perspective, these clocks are expected to lose or gain one cycle in a few billion years. These drift rates are consistent with evolutionary cooling in our models (e.g. Bradley, Winget, & Wood 1992; Bradley 1996).

However, the 274 s mode in R 548 indicates a drift rate faster than the



213 s mode by a factor of  $\sim 100$  (Mukadam et al. 2003a). The 270 s and the 304 s modes in G 117-B15A indicate a drift rate faster than the 215 s mode by factors of 10 and 20 respectively (Costa 2004). Different modes sample the star in a different way, and their drift rates could well be influenced by changing conditions other than cooling. They could be undergoing an avoided crossing. It is also conceivable that the 270 s modes measure stellar cooling, while the 215 s mode constrains the stability of the mode trapping mechanism.

The cDAV stars exhibit many pulsation modes, the amplitudes of which are observed to change significantly on timescales, orders of magnitude shorter than the evolutionary cooling (e.g. Pfeiffer et al. 1996; Kleinman et al. 1998). Although the eigenmodes of the cDAVs should also drift at the evolutionary rate, we have not yet been able to confirm this theoretical expectation.

## 5.4 Why study ZZ Ceti stars as an ensemble?

Fundamental physics of degenerate matter governs the interior equation of state of white dwarf stars. White dwarf masses are distributed in a narrow range around  $0.6 M_{\odot}$ . The ZZ Ceti variables have effective temperatures confined in the range 10850–11800 K. White dwarfs with masses in the range  $0.55$ – $1.1 M_{\odot}$  possess carbon-oxygen cores (Iben 1990), and their composition is dictated by the  $^{12}\text{C}(\alpha, \gamma)^{16}\text{O}$  nuclear reaction rate (Metcalf, Winget, & Charbonneau 2001; Metcalfe, Salaris, & Winget 2002; Metcalfe 2003). These fundamental similarities between various ZZ Ceti stars assure us that ensemble seismology may prove to be an effective technique in probing the stellar interiors. Pulsation modes that probe the core better than others are likely to show a signature of this similarity. Ensemble seismology seems to be the only way to decipher pulsators that show relatively few modes, such as the typical hDAVs.

## 5.5 Teaching different DAVs to play the same tune

Different ZZ Ceti stars have different masses, even though the dispersion in mass is small. Increasing the mass of a pulsating white dwarf causes the star to contract, and reducing the size of this resonating structure changes the eigenfrequencies. This is similar to changing the length of a vibrating string. Massive white dwarfs are also comparatively more dense than  $0.6 M_{\odot}$  white dwarfs; this is similar to increasing the density of the vibrating string. As a pulsator cools, traversing across the instability strip, the periods of the eigenmodes increase at the rate of  $\sim 4 \times 10^{-15} \text{ s/s}^1$  (Kepler 2004; private communication). Hydrogen and helium layer masses also play a role in tuning the eigenfrequencies of this musical instrument.

Massive pulsators ( $\log g \geq 8.6$ ) are expected to be substantially crystallized (see section 1.2.3). Pulsations are excluded from the crystallized region; the crystallization front serves as a hard boundary and this changes the pulsation periods substantially in our models of ZZ Ceti stars. In order to study these stars as an ensemble, i.e. in order to add the observed periods of different ZZ Ceti stars to a single set of modes, we will have to take their differences into account.

### 5.5.1 Scaling the pulsation spectra

We show all the pulsation periods of all the ZZ Ceti stars in the Tables 5.1 and 5.2. Figures 5.4–5.6 show the pulsation spectra of individual DAVs. We also show the grand sum of all the observed modes in Figure 5.7, and indicate a histogram of the observed periods. If we vary the bin size in the histogram,

---

<sup>1</sup>Note that this slow drift in the eigenmodes as a result of cooling is different from the increase in observed pulsation periods as the ZZ Ceti star traverses the instability strip (sections 1.1, 5.2). The increase in observed pulsation periods is due to the change in the driving frequency, which causes different eigenmodes to be excited in the star.

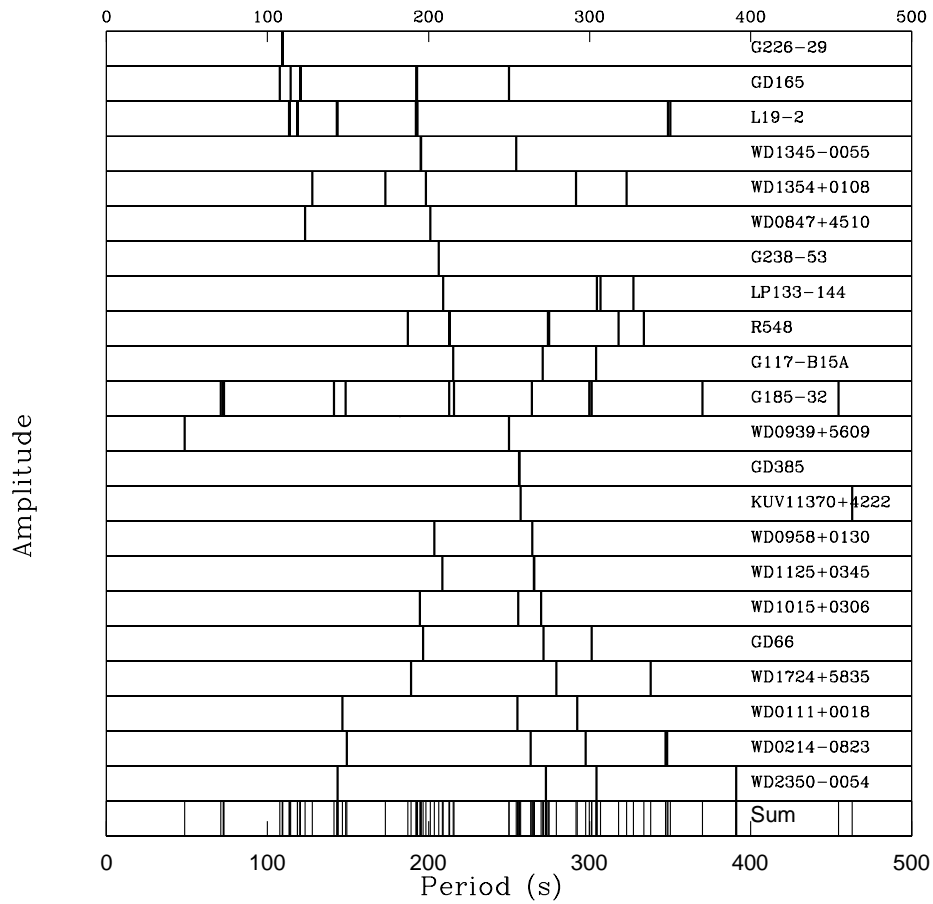


Figure 5.4: Pulsation spectra of the hDAVs

we find that various peaks rise and fall due to small number statistics. But we are convinced that the peaks marked in Figure 5.7 are real, as they are easily distinguished for various bin sizes. The histogram is suggestive that the peaks indicate modes with the same  $\ell$  and  $k$  values in different DAVs. But this may not be true for all cases.

Assuming that all the periods observed close to 205 s in the ZZ Ceti stars correspond to the same mode, we determine a group mean period at 204.8 s. We

Table 5.1: Pulsation periods and amplitudes of the known ZZ Ceti stars

Object	Mass ( $M_{\odot}$ )	Period (s) and Amplitude (mma)
G 226–29	0.78	109.47, 2.8; 109.28, 1.1; 109.09, 2.5
GD 165	0.64	120.36, 4.8; 249.90, 0.6; 192.79, 0.8; 192.68, 2.3; 192.57, 1.9; 120.40, 1.8; 120.32, 1.4; 114.28, 0.7; 107.60, 0.3
L 19–2	0.74	192.61, 5.8; 350.15, 1.0; 348.73, 0.4; 193.09, 1.0; 192.13, 0.7; 143.42, 0.6; 143.04, 0.3; 118.68, 1.1; 118.52, 1.8; 113.78, 2.1; 113.27, 0.6
WD1345–0055	0.63	195.20, 5.5; 254.40, 2.4; 195.50, 3.9
WD1354+0108	0.61	198.30, 6.0; 322.90, 1.9; 291.60, 2.2; 173.30, 1.1; 127.80, 1.50
WD0847+4510	0.61	201.00, 7.3; 123.40, 2.50
G 238–53	0.55	206.30, 8.10
LP133–144	0.53	209.18, 10.0; 327.32, 4.0; 306.90, 5.0; 304.50, 4.0
R 548	0.59	213.13, 6.7; 333.65, 1.0; 318.08, 0.9; 274.78, 2.9; 274.25, 4.1; 212.77, 4.1; 187.27, 1.0
G 117–B15A	0.59	215.22, 19.8; 304.15, 8.8; 270.86, 7.1
G 185–32	0.64	215.74, 1.9; 651.70, 0.7; 537.59, 0.6; 454.56, 0.4; 370.21, 1.6; 301.41, 1.1; 299.79, 0.9; 264.19, 0.5; 212.82, 0.5; 181.90, 0.03; 148.45, 0.6; 141.24, 0.4; 72.92, 0.4; 72.54, 0.9; 70.93, 0.7
WD0939+5609	0.74	249.90, 7.2; 48.50, 5.9
GD 385	0.63	256.13, 11.4; 256.33, 10.9
KUV 11370+4222	0.64	257.10, 5.3; 463.00, 3.0
WD0958+0130	0.60	264.40, 4.7; 203.70, 2.5
WD1125+0345	0.60	265.50, 7.2; 265.80, 3.3; 208.60, 2.8
WD1015+0306	0.69	270.00, 8.4; 255.70, 7.3; 194.70, 5.8
GD 66	0.64	271.40, 14.7; 810.40, 6.5; 301.40, 9.7; 196.70, 3.7
WD1724+5835	0.54	279.50, 8.3; 337.90, 5.9; 189.20, 3.2
WD0111+0018	0.77	292.30, 21.9; 255.30, 15.6; 146.50, 7.1
WD0214–0823	0.56	297.50, 16.0; 348.10, 8.4; 347.10, 8.2; 263.50, 7.1; 149.20, 3.5
WD2350–0054	0.80	304.30, 15.4; 391.10, 7.5; 273.00, 11.2; 143.50, 5.0
GD 244	0.66	307.00, 14.0; 294.60, 5.0; 256.30, 10.0; 203.30, 4.0
KUV 08368+4026	0.64	307.90, 10.0; 778.80, 5.0; 519.90, 4.0; 400.10, 5.0; 362.50, 2.0; 257.30, 9.0
WD0842+3707	0.44	309.30, 17.9; 212.30, 5.2; 154.10, 4.0
WD0815+4437	0.56	311.70, 22.0; 787.50, 6.6; 511.50, 7.3; 311.30, 9.3; 258.30, 6.2
G 207–9	0.82	317.97, 8.9; 738.55, 7.4; 557.41, 8.6; 291.97, 8.9; 259.07, 3.6
HS0507+0435	0.71	355.80, 23.7; 743.40, 7.7; 557.60, 15.7; 556.60, 5.8; 555.30, 17.1; 446.10, 13.5; 445.30, 2.8; 444.60, 11.6; 355.40, 4.3; 354.90, 10.0
WD0949–0000	0.74	365.20, 17.7; 711.60, 6.0; 634.20, 5.1; 516.60, 16.2; 364.00, 7.3; 363.20, 12.5; 213.30, 6.0; 181.10, 3.9
WD1015+5954	0.62	400.70, 19.2; 1116.50, 12.8; 454.90, 17.9; 292.40, 8.5; 213.00, 13.0
MCT 0145–2211	0.69	462.20, 25.0; 823.20, 15.0; 727.90, 18.0
HL Tau 76	0.54	540.00, 29.0; 597.00, 14.0; 494.00, 26.0; 382.00, 16.0
WD0923+0120	1.06	595.20, 7.4
WD1711+6541	1.00	606.20, 5.3; 1248.20, 3.2; 690.20, 3.3; 234.00, 1.3
EC 14012–1446	0.71	610.00, 61.0; 937.00, 11.0; 724.00, 18.0; 530.00, 18.0; 399.00, 14.0

Table 5.2: Pulsation periods and amplitudes of the known ZZ Ceti stars (Cont'd)

Object	Mass ( $M_{\odot}$ )	Period (s) and Amplitude (mma)
G29-38	0.69	614.00, 40.3; 915.44, 5.9; 894.04, 14.0; 859.64, 24.6; 809.45, 30.1; 770.75, 5.1; 678.40, 9.7; 648.70, 7.8; 551.90, 4.4; 499.30, 8.6; 401.23, 7.4; 400.43, 4.7; 399.66, 6.8; 354.94, 2.9; 283.87, 4.1
BPM31594	0.68	617.30, 24.2; 401.90, 9.4; 532.60, 5.0; 416.10, 5.0
WD1502-0001	0.61	629.50, 32.6; 687.50, 12.0; 581.90, 11.1; 418.20, 14.9; 313.60, 13.1
BPM37093	1.11	637.00, 1.6; 633.00, 1.3; 614.00, 1.1; 601.00, 0.7; 583.00, 0.9; 582.00, 1.1; 565.00, 1.2; 548.00, 1.1; 531.00, 1.2; 512.00, 0.7; 549.00, 0.8
WD0825+4119	0.91	653.40, 17.1; 611.00, 11.2
PG 1541+650	0.67	686.00, 45.0; 757.00, 14.0; 564.00, 15.0; 467.00, 0.7
HE 0532-5605	0.91	688.80, 8.0; 586.40, 7.8
WD0942+5733	0.77	694.70, 37.7; 550.50, 12.2; 451.00, 18.4
HE 1258+0123	0.63	744.60, 23.0; 1092.10, 14.0; 528.50, 10.0; 439.20, 10.0
WD0332-0049	0.76	767.50, 15.1
WD0906-0024	0.61	769.40, 26.1; 618.80, 9.1; 574.50, 23.7; 457.90, 9.5; 266.60, 7.6
BPM30551	0.75	823.00, 29.0; 744.70, 9.0; 682.70, 8.0; 607.00, 12.0
WD0318+0030	0.65	826.40, 21.1; 587.10, 10.1; 536.10, 10.6
KUV 02464+3239	0.66	831.60, 40.0
R 808	0.63	833.00, 50.0
WD1122+0358	0.64	859.10, 34.3; 996.10, 17.9
G 191-16	0.64	860.00, 70.0; 596.00, 10.0; 508.00, 10.0; 388.00, 10.0; 365.00, 5.0
WD1617+4324	0.63	889.60, 36.6; 626.30, 24.1
WD1700+3549	0.63	893.40, 54.7; 955.30, 20.4; 450.50, 19.3
WD1417+0058	0.63	894.50, 43.1; 812.50, 31.3; 522.00, 15.2
WD1157+0553	0.70	918.90, 15.9; 1056.20, 5.8; 826.20, 8.1; 748.50, 5.6
WD0102-0032	0.76	926.10, 37.2; 830.30, 29.2
PG 2303	0.66	936.30, 43.7; 1228.50, 7.7; 577.93, 11.6; 539.84, 5.1; 482.60, 6.2; 394.32, 8.8
G 38-29	0.55	938.00, 28.00, 1024.00, 26.00; 1020.00, 26.0; 910.00, 27.0
WD1056-0006	0.52	942.20, 62.3; 474.40, 22.9
G 255-2	0.71	985.22, 4.4; 898.47, 8.7; 855.43, 10.3; 819.67, 10.4; 775.19, 14.0; 773.40, 11.7; 681.20, 24.2; 607.90, 12.1; 568.51, 10.7; 325.42, 4.5
EC 23487-2424	0.67	993.00, 37.7; 804.50, 19.3; 868.20, 12.8; 989.30, 11.0
GD99	0.66	1026.00, 8.1; 1071.70, 3.4; 1059.50, 5.2; 1004.80, 4.1; 1002.30, 2.1; 849.70, 2.2; 665.30, 1.5; 633.10, 2.0; 300.70, 1.4; 230.60, 1.6; 228.60, 4.5; 223.30, 2.7; 221.40, 1.7; 126.10, 2.1
G 30-20	0.58	1068.00, 13.8
WD1732+5905	0.60	1122.40, 8.0; 1248.40, 4.5
BPM 24754	0.63	1176.50, 22.6; 1123.60, 6.5; 1098.90, 6.1; 1087.00, 13.2; 1052.60, 9.1; 980.40, 7.7
GD 154	0.70	1186.50, 16.7; 1190.50, 6.3; 1183.50, 4.6; 1092.00, 3.0; 1088.60, 5.0; 1084.00, 5.6; 402.60, 2.7
WD1443+0134		968.90, 7.5; 1085.00, 5.2
WD1524-0030		873.20, 111.5; 434.00, 47.8
WD2350-0054		304.30, 15.4; 391.10, 7.5; 273.00, 11.2; 143.50, 5.0
HS0951+1312		208.00, 9.3; 281.60, 8.8; 258.60, 3.6
HS0952+1816		1159.70, 4.8; 1466.00, 4.5; 853.80, 3.9

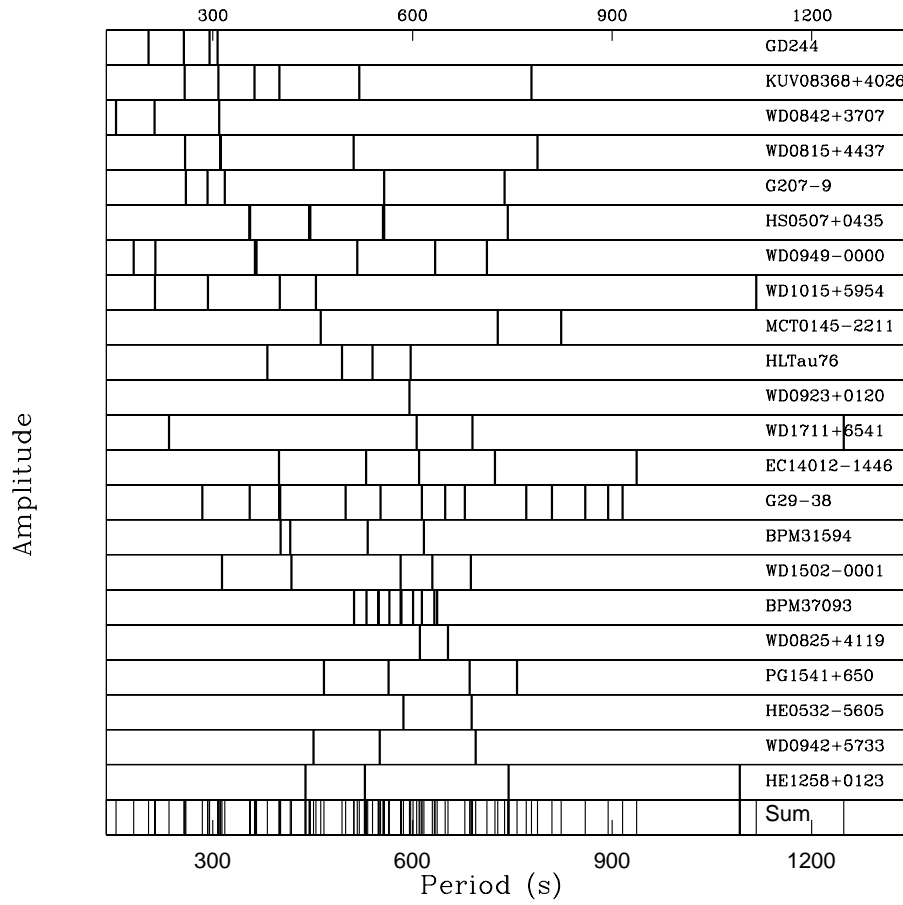


Figure 5.5: Pulsation spectra of the intermediate temperature DAVs

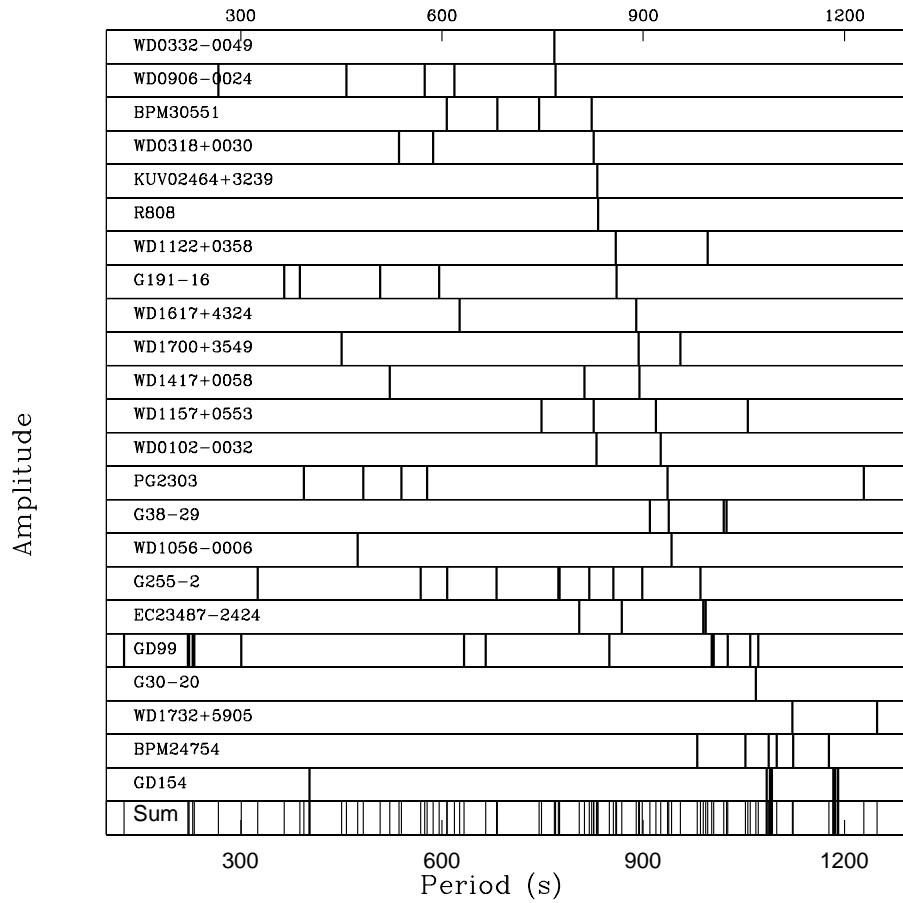


Figure 5.6: Pulsation spectra of the cDAVs

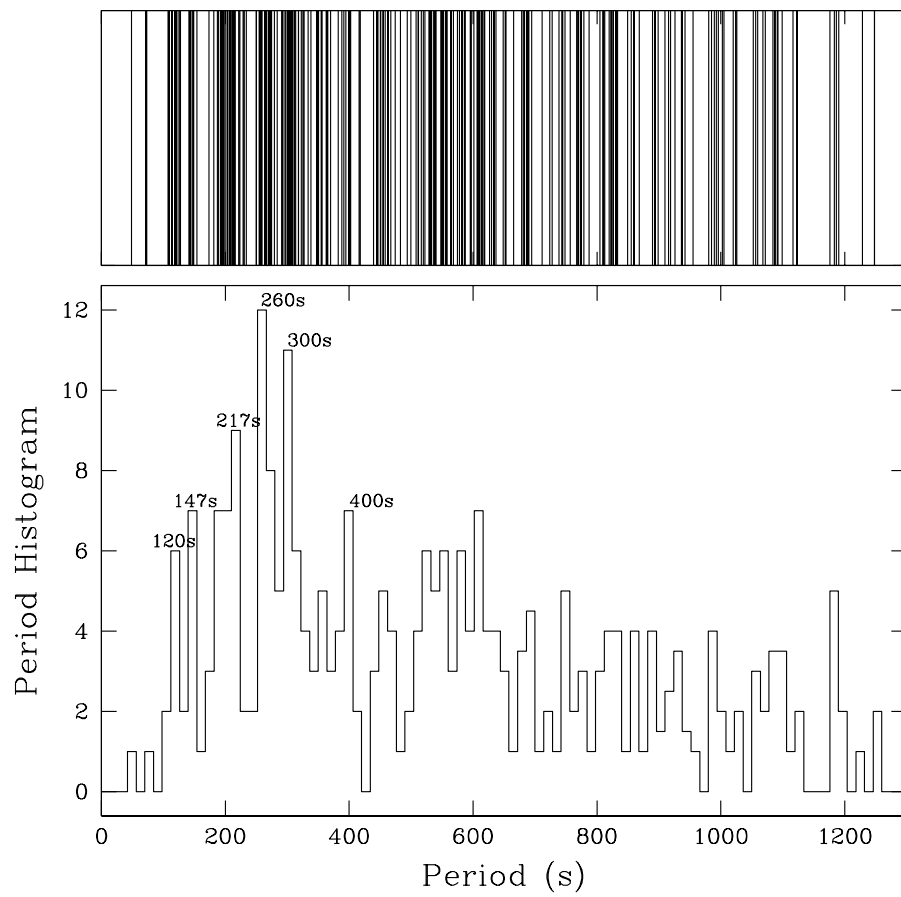


Figure 5.7: Grand Sum of the pulsation spectra of all DAVs

Table 5.3: Periods observed close to 205 s as a function of  $\log g$

Object	SDSS $T_{\text{eff}}$ (K)	SDSS $\log g$	$P_{\text{obs}}/P_0$
GD165	$11980 \pm 200$	$8.06 \pm 0.05$	0.94
L19-2	$12100 \pm 200$	$8.21 \pm 0.05$	0.94
WD1354+0108	$11750 \pm 050$	$8.05 \pm 0.02$	0.97
WD0847+4510	$11740 \pm 120$	$7.97 \pm 0.07$	0.98
WD1345-0055	$11840 \pm 060$	$8.09 \pm 0.03$	0.95
G238-53	$11890 \pm 200$	$7.91 \pm 0.05$	1.01
LP133-144	$11800 \pm 200$	$7.87 \pm 0.05$	1.02
R548	$11990 \pm 200$	$7.97 \pm 0.05$	1.04
G117-B15A	$11630 \pm 200$	$7.97 \pm 0.05$	1.05
GD244	$11680 \pm 200$	$8.08 \pm 0.05$	0.99
WD1015+0306	$11620 \pm 030$	$8.17 \pm 0.01$	0.95
WD1125+0345	$11650 \pm 130$	$8.05 \pm 0.07$	1.02
WD0958+0130	$11730 \pm 060$	$8.03 \pm 0.03$	0.99
GD66	$11980 \pm 200$	$8.05 \pm 0.05$	0.96
WD0842+3707	$11860 \pm 210$	$7.60 \pm 0.10$	1.04
G185-32	$12130 \pm 200$	$8.05 \pm 0.05$	1.05
WD1724+5835	$11650 \pm 080$	$7.94 \pm 0.05$	0.92
GD99	$11820 \pm 200$	$8.08 \pm 0.05$	1.09
WD0949-0000	$11190 \pm 130$	$8.26 \pm 0.11$	1.04
WD1015+5954	$11680 \pm 110$	$8.03 \pm 0.06$	1.04

plot the ratio of the observed periods, divided by the group mean, as a function of  $\log g$  in Figure 5.8. We indicate these values in Table 5.3.

M. Montgomery (Montgomery; private communication) computed DA white dwarf models close to  $0.6 M_{\odot}$  with a He layer mass of  $2 \times 10^{-2} M_{\star}$  and a H layer mass of  $2 \times 10^{-4} M_{\star}$ . Keeping the layer masses constant, he changed the mass of the star by  $0.05 M_{\odot}$  in both directions and determined the corresponding fractional change in period. We show these points (squares) from the numerical models in Figure 5.8, and find that the models agree with the observations for a significant fraction of the DAVs.

Assuming that all the periods close to 260 s correspond to the same mode, we arrived at a group mean of 262.1 s. We show the observed periods

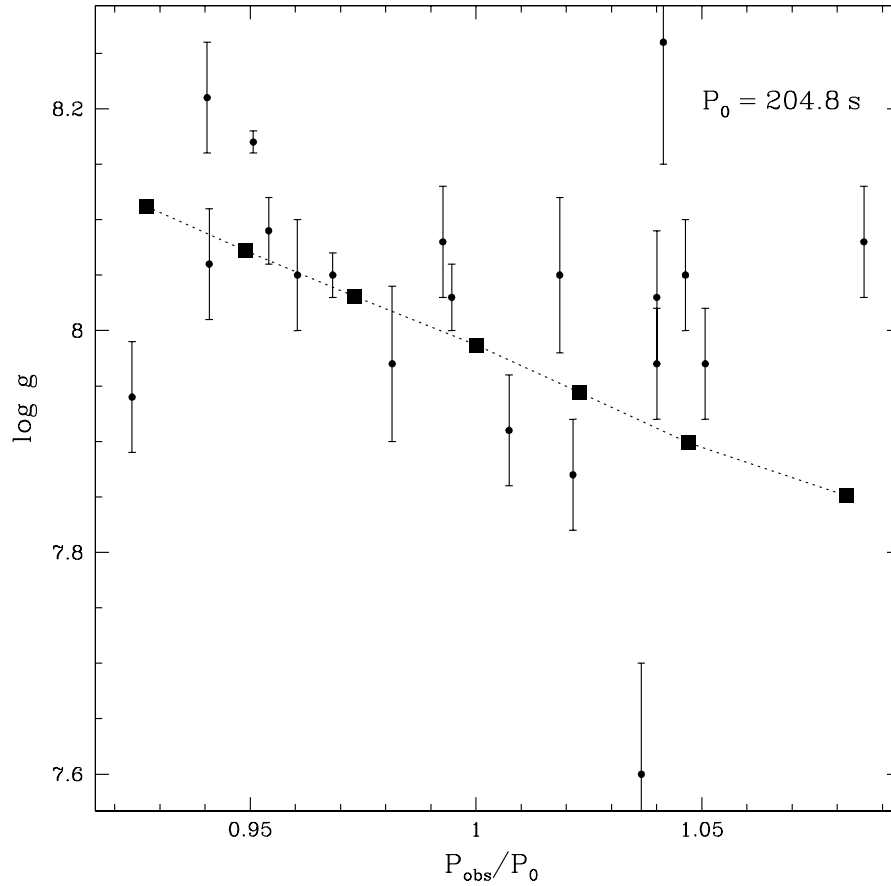


Figure 5.8: ZZ Ceti stars with periods around 205 s exhibit a group mean at 204.8 s. Dividing the pulsation period of each star by the group mean gives us a relative shift in individual periods, which we plot as a function of  $\log g$ . The squares connected by the dotted line indicate values of the shift computed using DA white dwarf models around  $0.6 M_{\odot}$  with a He layer mass of  $2 \times 10^{-2} M_{\star}$  and a H layer mass of  $2 \times 10^{-4} M_{\star}$ .

Table 5.4: Periods observed close to 262 s as a function of  $\log g$

Object	SDSS $T_{\text{eff}}$ (K)	SDSS $\log g$	$P_{\text{obs}}/P_0$
GD165	$11980 \pm 200$	$8.06 \pm 0.05$	0.95
WD1345-0055	$11840 \pm 060$	$8.09 \pm 0.03$	0.97
R548	$11990 \pm 200$	$7.97 \pm 0.05$	1.05
G117-B15A	$11630 \pm 200$	$7.97 \pm 0.05$	1.03
GD244	$11680 \pm 200$	$8.08 \pm 0.05$	0.98
WD1015+0306	$11620 \pm 030$	$8.17 \pm 0.01$	0.98
WD1125+0345	$11650 \pm 130$	$8.05 \pm 0.07$	1.01
WD0958+0130	$11730 \pm 060$	$8.03 \pm 0.03$	1.01
WD0939+5609	$11770 \pm 160$	$8.27 \pm 0.07$	0.95
GD66	$11980 \pm 200$	$8.05 \pm 0.05$	1.04
WD0111+0018	$11430 \pm 100$	$8.27 \pm 0.06$	0.97
KUV11370+4222	$11890 \pm 200$	$8.06 \pm 0.05$	0.98
GD385	$11710 \pm 200$	$8.04 \pm 0.05$	0.98
WD0214-0823	$11610 \pm 090$	$7.99 \pm 0.05$	1.01
WD1724+5835	$11650 \pm 080$	$7.94 \pm 0.05$	1.07
WD2350-0054	$10390 \pm 060$	$8.30 \pm 0.06$	1.04
G185-32	$12130 \pm 200$	$8.05 \pm 0.05$	1.01
KUV08368+4026	$11490 \pm 200$	$8.05 \pm 0.05$	0.98
WD0815+4437	$11630 \pm 170$	$7.93 \pm 0.09$	0.99
G207-9	$11950 \pm 200$	$8.35 \pm 0.05$	0.99
WD0906-0024	$11570 \pm 090$	$8.00 \pm 0.06$	1.02

divided by the group mean as a function of  $\log g$  in Figure 5.9, and list the corresponding values in Table 5.4.

Both Figures 5.8 and 5.9 show a reasonable agreement with models in the vicinity of  $\log g = 8$ . But the periods observed for ZZ Ceti stars with relatively higher masses ( $\log g \geq 8.25$ ) and lower masses ( $\log g \leq 7.8$ ) do not agree with the models. There are many possible explanations, and we explore some of them below:

- Periods from heterogeneous modes: We assumed that all the periods close to 205 s and 260 s, respectively, correspond to the same modes; this need not be true. Preliminary investigations show that the periodicities close

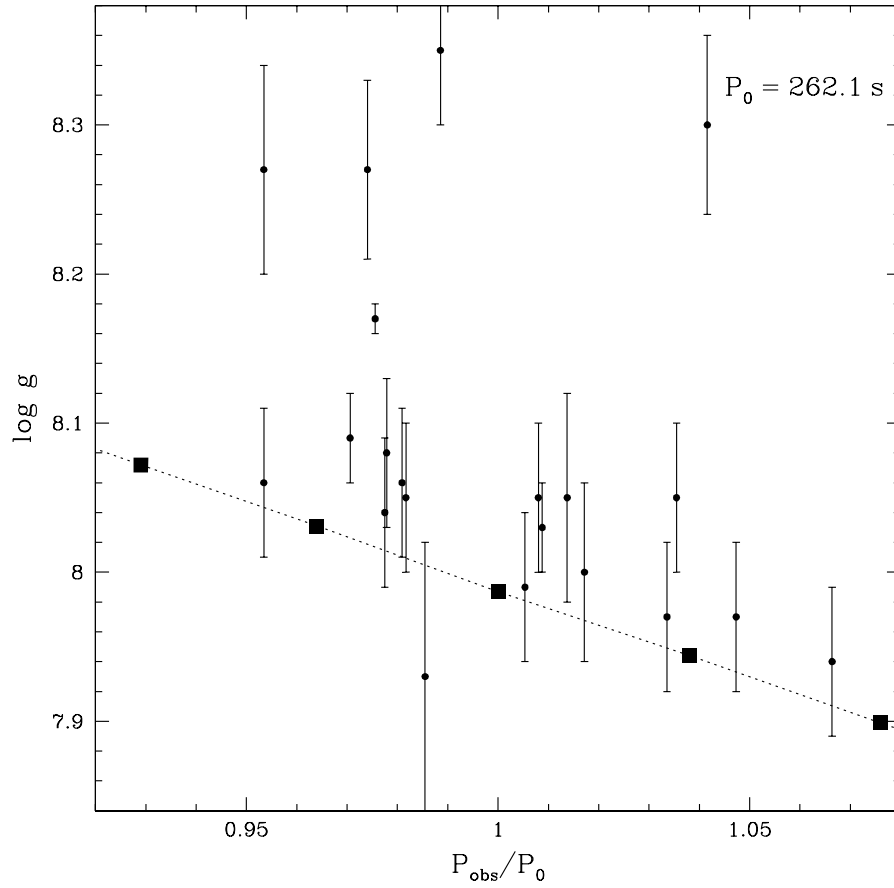


Figure 5.9: ZZ Ceti stars with periods around 260 s yield a group mean of 262.1 s. Dividing the pulsation period of each star by the group mean gives us a relative shift in individual periods, which we plot as a function of  $\log g$ . The points connected by the dotted line indicate values of the shift computed using DA white dwarf models around  $0.6 M_{\odot}$  with a He layer mass of  $2 \times 10^{-2} M_{\star}$  and a H layer mass of  $2 \times 10^{-4} M_{\star}$ .

to 205 s and 260 s in the stars LP133-44, G 238-53, WD0847+4510, and WD0815+4437 may well be  $\ell = 2$  modes.

- **Erroneous  $\log g$  determinations:** The low signal-to-noise of the blue end of the SDSS spectra reduces the reliability of the  $\log g$  values (see section 4.1.3) for the SDSS DAVs. However, massive DAVs with  $T_{\text{eff}}$  and  $\log g$  determinations from Bergeron et al. (2004) also deviate significantly from the models. Hence, it is unlikely that erroneous  $\log g$  determinations are causing the relative high and low mass ZZ Ceti stars to deviate from the models.
- **Effects of Mode Trapping:** Compositional stratification occurs in white dwarf stars due to gravitational settling and prior nuclear shell burning; this alters the kinetic energy of oscillation for different modes in our models. A mechanical resonance is induced between the local g-mode oscillation wavelength and the thickness of one of the compositional layers (Winget, Van Horn & Hansen 1981). This mechanical resonance serves as a stabilizing mechanism in model calculations (Brassard et al. 1992; Montgomery 1998). Trapped modes are energetically favored, as the amplitudes of their eigenfunctions below the H/He interface are smaller than untrapped modes. Modes trapped in the envelope can have kinetic oscillation energies lower by a few orders of magnitude, as compared to the adjacent non-trapped modes (Winget et al. 1981; Brassard et al. 1992). Benvenuto et al. (2002) claim a marked weakening of mode trapping effects with a time-dependent element diffusion in the DA white dwarf models with different thicknesses of the hydrogen envelope.

Mode trapping can alter the period spacing for low  $k$  modes. The periods we observe close to 205 s are probably  $\ell = 1, k = 2$ , and the periods close to 260 s are likely  $\ell = 1, k = 3$ . It is therefore possible that the observed

periods in Figures 5.8 and 5.9 constitute trapped and untrapped modes. It could also be that the modes trapped in the star are untrapped in the models, and vice-versa.

- Different layer masses: Different H and He layer masses alter the trapping properties in a ZZ Ceti star, and change the observed periods. The models we show in Figures 5.8 and 5.9 have the same H and He layer mass. Perhaps some of the scatter in the plots arises from different H and He layer masses in the ZZ Ceti stars.
- Binary evolution: We observe a substantial deviation from the models for relatively high and low mass ZZ Ceti stars. Perhaps these stars originated in interacting binaries, and have substantially different H and/or He layer masses as a result of a different evolution.
- Missing physics in models: It is also conceivable that our models are incorrect in predicting pulsation periods for the relatively high and low mass ZZ Ceti stars.

More than one of the above possibilities may be true; we hope to continue our explorations and analyses over the next few months. This chapter is a work in progress.

## 5.6 Conclusions

We find that the new DAVs conform to the well established trend of increasing pulsation periods and amplitudes, as we compare the cool ZZ Ceti stars to the hot DAVs. Our homogeneous sample with consistent data reductions suggests a decline in pulsation amplitudes close to the red edge, before pulsations shut

down entirely. This may be the first observational evidence that the red edge is not an abrupt feature in the ZZ Ceti evolution.

Clemens (1993) showed that all hDAVs are essentially identical, except for different stellar masses. He showed that their pulsation spectra could be aligned by translation, and a plot of the amount of shift vs  $\log g$  was linear. In attempting to extend this idea to the new DAVs, we find that although it works well around  $\log g \approx 8$ , it does not work for hDAVs with relatively higher masses ( $\log g \geq 8.25$ ) and lower masses ( $\log g \leq 7.8$ ). Perhaps high and low mass pulsators have different hydrogen and/or helium layer masses, since they went through a different evolutionary path. It is also possible that our assumption that all periods close to 205 s and 260 s belong to the same modes respectively, may not be true. We conclude that we can only use hDAVs with  $\log g \approx 8$  for ensemble asteroseismology, until we can explain the observed differences between the relatively massive and low mass variables.

## Chapter 6

# Summary and future work

### 6.1 Seismology of the ZZ Ceti stars

Global pulsations in stars provide the only current systematic way to study their interiors. White dwarf stars are the stellar remains of 98–99% of stars in the sky, and contain an archival record of their main sequence lifetime. Pulsating white dwarf stars serve as effective instruments to harness this archival record. Their high densities and temperatures make them good cosmic laboratories to study fundamental physics under extreme conditions. Known white dwarfs at  $T_{\text{eff}} \sim 4500$  K are among the oldest stars in the solar neighborhood, and they serve as reliable chronometers to date the Galactic disk and halo. The carbon-oxygen ratio in white dwarf cores contains the rate of the astrophysically important, but experimentally uncertain,  $^{12}\text{C}(\alpha, \gamma)^{16}\text{O}$  nuclear reaction.

Since 80% of all white dwarf stars are DAs, to understand the DAVs is to understand the most common type of white dwarf. Understanding the structure and evolution of a statistically significant sample of DAVs has implications for other areas of astronomy as well. We can use ensemble asteroseismology to probe the stellar structure; the ensemble of modes can be gathered from a single

DAV with a rich pulsation spectrum or from multiple DAVs with relatively fewer modes, if their structures are similar.

### **6.1.1 Benefits of an ensemble of DAVs**

The hDAVs that show modes with long term stability ( $\dot{P} \sim 10^{-15}$  s/s) can be used as accurate clocks. These clocks serve as potential detectors of planetary systems, since any reflex motion will cause a periodic variation in their drift rate. In the absence of orbiting companions, the slow unidirectional drift rate of their period can help us constrain the white dwarf evolutionary sequences. These cooling curves are ultimately useful in cosmochronometry, constraining the age of the Galactic disk and halo using the age distribution of white dwarfs vs effective temperature. Massive DAVs allow us to study crystallization in a stellar plasma, relevant for white dwarf cosmochronometry as well as neutron star crusts. The seismological distances for the DAVs are more accurate than distances from measured values of parallax. Pulsating DAVs are helpful in establishing a Galactic distance scale in more ways than one.

## **6.2 Ideal instrumentation for the DAV search**

Searching for a statistically significant number of DAVs seemed useful for all of the reasons listed above. However, since most of the nearby ZZ Ceti stars had been found, the only way to discover a large sample of new DAVs was to observe at fainter magnitudes. That required a new instrument; our previous photometer based on PMTs enabled us to observe targets brighter than B=17 on the 2.1 m telescope at McDonald Observatory. Thus, Argos was born and it saw first light on 1 November 2001 at the prime focus of the 2.1 m telescope, six months after we purchased the CCD camera from Roper Scientific. R. E. Nather single

handedly wrote the data acquisition program, operable in a Linux environment. Gordon Wesley and David Boyd designed the prime focus mount for the camera, and the parts were built in a commercial machine shop. Gary Hansen designed the timing card that serves as a crucial component for instrument timing.

We obtained usable data with Argos on the very first night, when we observed KUV08368+4026 at the 2.1 m telescope at McDonald Observatory. We list the significant improvements to the instrument over the following two years:

- The commissioning run made us realize that the shiny aluminium surfaces of the mount were acting as a mirror for stray light. We bead-blasted the metallic parts of the mount, and had them hard anodized (Type II). The matt dark surface, resistant to corrosion, improved data quality substantially.
- We initially used GPS pulses from the adjacent 2.7 m telescope as input 1 Hz pulses for instrument timing. The S/N ratio was reduced due to the long length of the cable, so that the timing card sometimes counted noise pulses as genuine pulses. We then solved a large fraction of our timing problems by using 1 Hz pulses from our own GPS system at the 2.1 m telescope.
- The initial design for Argos consisted of a single baffle, 10% larger than the F/3.9 light beam. This allowed us to observe each car passing by the Observatory, and practically every glow worm in the dome. We substituted the dysfunctional baffle with an effective 5-stage baffle system, designed with help and guidance from Phillip McQueen. The baffles were machined by George Barczak in the department.
- Dr. R. E. Nather made the next significant improvement to Argos; we stopped using the PC clock tuned by NTP for timing, and started using

information from the GPS system directly to tune the PC clock.

- The dome of the 2.1 m telescope does not track; an observer needs to guide the dome manually as needed. We purchased a new uncooled CCD camera to ride on the telescope, and take pictures of the dome. These images, transmitted to the control room, serve to inform the observer when it is time to move the dome. Dr. R. E. Nather wrote the data acquisition program for Cyclops, and Denis Sullivan helped us test the camera extensively, giving us valuable suggestions at every stage. Jimmy Welborn machined the mount for Cyclops.

### **6.3 Fruitful search for the ZZ Ceti stars**

We discovered 35 new ZZ Ceti stars with Argos, mainly observing DAV candidates from the Sloan Digital Sky Survey. After trying to select DAV candidates using  $u - g$  colors, and then equivalent widths, we settled with the higher success rate of the spectroscopic technique. Our SDSS collaborators, namely Scot and Atsuko Nitta Kleinman, sent us  $T_{\text{eff}}$  and  $\log g$  determinations for SDSS DA white dwarfs. We selected candidates for observation based on their  $T_{\text{eff}}$  values. Daniel Eisenstein used Detlev Koester's atmosphere models to derive these parameters, which were immensely useful to us. We could achieve a 90% success rate by confining our candidates between 12 000 K and 11 000 K at a detection threshold of 1-3 mma. But our interest in hDAVs and the blue edge of the instability strip led us to choose candidates between 12 500 K and 11 000 K, reducing our success rate to 80%. With the discovery of 35 new DAVs, we almost doubled the sample of 39 published ZZ Ceti stars.

## 6.4 Empirical ZZ Ceti instability strip

We used the 30 new variables with reliable  $T_{\text{eff}}$  and  $\log g$  determinations discovered within the SDSS, along with G 238-53, to re-define the empirical ZZ Ceti instability strip. This was the first time since the discovery of white dwarf variables in 1968 that we had a homogeneous set of spectra acquired using the same instrument on the same telescope, and with consistent data reductions, for a statistically significant sample of ZZ Ceti stars. The homogeneity of the spectra reduced the scatter in the spectroscopic temperatures and we found a narrow instability strip of width  $\sim 950$  K, from 10850–11800 K. We questioned the purity of the DAV instability strip due to the presence of several non-variables within. The slope of our best fit for the red edge of the instability strip is well constrained, but the slope of the blue edge is not.

The DAV distribution shows a scarcity of DAVs in the range 11350–11500 K. After exploring various possible causes for such a bimodal, non-uniform distribution, we are still not entirely confident that it is real. The data at hand are suggestive that the non-uniformity of the DAV distribution is real, and stayed hidden from us for decades due to the inhomogeneity of the spectra of the previously known DAVs. However, we are in the domain of small number statistics and unless we investigate additional targets in the middle of the strip, we cannot be confident that the bimodal distribution is not an artifact in our data.

## 6.5 Ensemble characteristics of the ZZ Ceti stars

The new ZZ Ceti stars exhibit the well established trend of longer pulsation periods and larger amplitudes, as we traverse across the instability strip to the red edge. We may have found the first observational evidence that the red edge

is not an abrupt feature in the ZZ Ceti evolution, and that pulsation amplitudes decline close to the red edge, before the variable stops pulsating.

Clemens (1993) showed that all hDAVs are essentially identical, except for different stellar masses. We tried to extend his work to the new DAVs; we find that ZZ Ceti stars with  $\log g \approx 8$  do seem fairly identical to each other, and we should be able to apply the technique of ensemble asteroseismology to their pulsation spectra. But we find that the relatively high ( $\log g \geq 8.25$ ) and low ( $\log g \leq 7.8$ ) mass ZZ Ceti variables cannot be scaled to the average mass hDAVs in a simple manner. Perhaps we are missing a relevant bit of physics in our models, or these stars have different H/He layer masses, composition, etc. reflective of their distinct evolution.

## 6.6 Future work

Multiple projects emerge as a result of the work described here, some of which we list below:

- High quality homogeneous spectra with  $S/N \geq 60$  for all the 74 DAVs known to date, followed by consistent data reductions, should lead to a reliable determination of the shape of the ZZ Ceti instability strip. The location and edges of the instability strip could help us understand the role of convection. This may also shed more light on WD2350-0054, the hDAV whose SDSS  $T_{\text{eff}}$  determination places it 650 K below the cool edge of the instability strip.

The impure instability strip defined by our sample is most disconcerting, since we have to be prudent in applying the conclusions drawn from variable white dwarfs to non-variable white dwarfs. This result should be verified independently, with reliable  $\log g$  determinations. Looking for

similarities between non-variables inside the ZZ Ceti strip may provide us with some explanations of why all DA white dwarfs do not evolve through the instability strip in the same way. Perhaps the blue edge depends not only on the temperature and mass of the star, but on additional parameters. Perhaps the non-variables have a strong magnetic field or some other mechanism that shuts down pulsations.

- High signal to noise photometric observations of massive pulsators such as WD 1711+6541 ( $g = 16.9$ ) and WD 0923+0120 ( $g = 18.3$ ) may lead to additional modes. Each mode we observe brings us closer to obtaining a unique model-fit to the star, which gives us an estimate of the crystallized mass fraction. Metcalfe, Montgomery, & Kanaan (2004) have already presented strong evidence that the massive DAV, BPM 37093, is 90% crystallized. Crystallization and phase separation represent the biggest sources of uncertainty in white dwarf cosmochronometry. This study is also relevant to neutron star crusts.
- The low mass pulsator WD 0842+3707 could be a He core white dwarf, most probably conceived in an interacting binary system. Single star evolutionary models cannot produce such low mass white dwarfs in a Hubble time (Iben 1990). Using pulsations to probe the equation of state for a He core white dwarf could prove to be highly enlightening, as we do not really understand how bosons behave at high densities.
- WD 0949-0000, WD 1015+5954, GD 99, and possibly a few other DAVs show signs of three mode resonances, where two observed frequencies add to a third frequency. A resonance mechanism is different from linear combinations, because the third frequency is located at the site of a real mode, as in a parametric resonance. Such a mechanism might serve to stabilize

or de-stabilize the third frequency. Additional observations of WD0949-0000, WD1015+5954, and GD 99 may help us investigate this possibility further.

- Monitoring all the modes observed in the newly discovered hDAVs can shed more light on why we measure different drift rates for different periodicities in the same hDAV. It can also help us de-convolve the effect of cooling from other mechanisms that can alter the drift rate: trapping, avoided crossings, resonances, crystallization, and possibly magnetic fields to name a few. Such an understanding is crucial since we already use drift rate measures of hDAV pulsation periods to constrain our evolutionary models, and to search for orbiting planets.
- Theoretical model computations can help us understand the significance of effects other than stellar mass, such as  $T_{\text{eff}}$ , H and He layer masses, core composition, convection, etc. that change the observed period and pulse shape for a given mode.
- Continuing the search to find additional DAVs, that may unearth seismologically curious or extreme mass pulsators and refine our determination of the ZZ Ceti instability strip, is an interesting project as well.

# Bibliography

- Abazajian, K. et al. 2003, AJ, 126, 2081
- Abrikosov, A., A. 1960, Zh. Exsp. Teor. Fiz., 39, 1798
- Benvenuto, O. G., Córscico, A. H., Althaus, L. G., & Serenelli, A. M. 2002, MNRAS, 335, 480
- Benvenuto, O. G., García-Berro, E., & Isern, J. 2004, Physical Review D, 69, 082002
- Bergeron, P., Wesemael, F., Lamontagne, R., Fontaine, G., Saffer, R. A., & Allard, N. F. 1995, ApJ, 449, 258
- Bergeron, P., Leggett, S. K., & Ruiz, M. T. 2001, ApJS, 133, 413
- Bergeron, P., Fontaine, G., Billères, M., Boudreault, S., & Green, E. M. 2004, ApJ, 600, 404
- Böhm, K. H. & Cassinelli, J. 1971, A&A, 12, 21
- Bradley, P. A., Winget, D. E., & Wood, M. A. 1992, ApJ, 391, L33
- Bradley, P. A. & Winget, D. E. 1994a, ApJ, 430, 850
- Bradley, P. A. & Winget, D. E. 1994b, ApJ, 421, 236
- Bradley, P. A. 1996, ApJ, 468, 350

- Bradley, P. A. 1998, *ApJS*, 116, 307
- Bradley, P. A. 2000, *Baltic Astronomy*, 9, 485
- Bradley, P. A. 2001, *ApJ*, 552, 326
- Brassard, P., Fontaine, G., Wesemael, F. & Hansen, C. J. 1992, *ApJS*, 80, 369
- Brassard, P. & Fontaine, G. 1997, *ASSL Vol. 214: White dwarfs*, 451
- Brickhill, A. J. 1975, *MNRAS*, 170, 405
- Brickhill, A. J. 1983, *MNRAS*, 204, 537
- Brickhill, A. J. 1991, *MNRAS*, 252, 334
- Chanmugam, G. 1972, *Nature Physical Science*, 236, 83
- Clemens, J. C. 1993, Ph.D. Thesis, University of Texas at Austin
- Costa, J. E. S., Kepler, S. O., & Winget, D. E. 1999, *ApJ*, 522, 973
- Costa, J. E. 2004, Ph.D. Thesis, Universidade Federal do Rio Grande do Sul
- Dolez, N. & Vauclair, G. 1981, *A&A*, 102, 375
- Dolez, N., Vauclair, G., & Koester, D. 1991, *NATO ASIC Proc. 336: White Dwarfs*, 361
- Dravins, D., Lindegren, L., Mezey, E., & Young, A. T. 1997, *PASP*, 109, 173
- Dravins, D., Lindegren, L., Mezey, E., & Young, A. T. 1998, *PASP*, 110, 610
- Duncan, M. J., & Lissauer, J. J. 1998, *Icarus*, 134, 303
- Dziembowski, W. 1977, *Acta Astronomica*, 27, 1
- Dziembowski, W. & Koester, D. 1981, *A&A*, 97, 16

- Fan, X. 1999, AJ, 117, 2528
- Finley, D. S., Koester, D., & Basri, G. 1997, ApJ, 488, 375
- Fleming, T. A., Liebert, J., & Green, R. F. 1986, ApJ, 308, 176
- Fontaine, G., Lacombe, P., McGraw, J. T., Dearborn, D. S. P., & Gustafson, J. 1982, ApJ, 258, 651
- Fontaine, G., Bergeron, P., Lacombe, P., Lamontagne, R., & Talon, A. 1985, AJ, 90, 1094
- Fontaine, G., Bergeron, P., Brassard, P., Billères, M., & Charpinet, S. 2001, ApJ, 557, 792
- Fontaine, G., Bergeron, P., Billères, M., & Charpinet, S. 2003, ApJ, 591, 1184
- Fukugita, M., Ichikawa, T., Gunn, J. E., Doi, M., Shimasaku, K., & Schneider, D. P. 1996, AJ, 111, 1748
- Giovannini, O., Kepler, S. O., Kanaan, A., Wood, A., Claver, C. F., & Koester, D. 1998, Baltic Astronomy, 7, 131
- Greenstein, J. L. 1982, ApJ, 258, 661
- Greenstein, J. L. & Liebert, J. W. 1990, ApJ, 360, 662
- Gunn, J. E. et al. 1998, AJ, 116, 3040
- Hagen, H.-J., Groote, D., Engels, D., & Reimers, D. 1995, A&AS, 111, 195
- Hansen, B. M. S. et al., 2002, ApJ, 574, L155
- Harris, H. C. et al. 2003, AJ, 126, 1023
- Hesser, J. E., Lasker, B. M., & Neupert, H. E. 1976, ApJ, 209, 853

- Hogg, D. W., Finkbeiner, D. P., Schlegel, D. J., & Gunn, J. E. 2001, *AJ*, 122, 2129
- Homeier, D., Koester, D., Hagen, H.-J., Jordan, S., Heber, U., Engels, D., Reimers, D., & Dreizler, S. 1998, *A&A*, 338, 563
- Homeier, D. & Koester, D. 2001a, *Astronomische Gesellschaft Meeting Abstracts*, 18, 111
- Homeier, D. & Koester, D. 2001b, in *ASP Conf. Ser. 226: 12th European Workshop on White Dwarfs*, eds. H.L. Shipman, J.L. Provencal, J. MacDonald & S. Goodchild, 397
- Homeier, D. 2001, Ph.D. Thesis, Christian-Albrechts-Universität zu Kiel
- Homeier, D. 2003, *NATO ASIB Proc. 105: White Dwarfs*, 371
- Hummer, D. G. & Mihalas, D. 1970, *MNRAS*, 147, 339
- Hynes, R. I., Robinson, E. L., & Jeffery, E. 2004, *ApJ*, 608, L101
- Iben, I. J. 1990, *ASP Conf. Ser. 11: Confrontation Between Stellar Pulsation and Evolution*, 483
- Isern, J., García-Berro, E., Hernanz, M., & Chabrier, G. 2000, *ApJ*, 528, 397
- Isern, J., García-Berro, E., & Salaris, M. 2002, *EAS Publications Series, Volume 2, Proceedings of "GAIA: A European Space Project"*, held 14-18 May, 2001 Les Houches, France. Edited by O. Bienaymé and C. Turon. EDP Sciences, 2002, pp.123-128, 2, 123
- Kalirai, J. S., Ventura, P., Richer, H. B., Fahlman, G. G., Durrell, P. R., D'Antona, F., & Marconi, G. 2001, *AJ*, 122, 3239
- Kanaan, A., Kepler, S. O., Giovannini, O., & Diaz, M. 1992, *ApJ*, 390, L89

- Kanaan, A., Winget, D. E., Kepler, S. O., & Montgomery, M. H. 2000a, in ASP Conf. Ser. 203, IAU Colloq. 176, The Impact of Large-Scale Surveys on Pulsating Star Research, ed. L. Szabados, & D. W. Kurtz (San Francisco: ASP), 518
- Kanaan, A., O'Donoghue, D., Kleinman, S. J., Krzesinski, J., Koester, D., & Dreizler, S. 2000b, *Baltic Astronomy*, 9, 387
- Kanaan, A., Kepler, S. O., & Winget, D. E. 2002, *A&A*, 389, 896
- Keeley, D. A. 1979, IAU Colloq. 53: White Dwarfs and Variable Degenerate Stars, 388
- Kepler, S. O., et al. 1991, *ApJ*, 378, L45
- Kepler, S. O., Giovannini, O., Kanaan, A., Wood, M. A., & Claver, C. F. 1995, *Baltic Astronomy*, 4, 157
- Kepler, S. O., Mukadam, A., Winget, D. E., Nather, R. E., Metcalfe, T. S., Reed, M. D., Kawaler, S. D., & Bradley, P. A. 2000a, *ApJ*, 534, L185
- Kepler, S. O., da Costa, A. F. M., Giovannini, O., & Koester, D. 2000b, *Baltic Astronomy*, 9, 125
- Kervella, P., Nardetto, N., Bersier, D., Mourard, D., & Coudé du Foresto, V. 2004, *A&A*, 416, 941
- Kirzhnits, D., A. 1960 *Sov. Phys.-JETP*, 11, 365
- Kleinman, S. J., Nather, R. E., & Phillips, T. 1996, *PASP*, 108, 356
- Kleinman, S. J. et al. 1998, *ApJ*, 495, 424
- Kleinman, S. J., et al. 2004, *ApJ*, 607, 426
- Koester, D. & Allard, N. F. 2000, *Baltic Astronomy*, 9, 119

Landolt, A. U. 1968, ApJ, 153, 151

Lasker, B. M. & Hesser, J. E. 1971, ApJ, 163, L89

Leggett, S. K., Ruiz, M. T., & Bergeron, P. 1998, ApJ, 497, 294

Lenz, D. D., Newberg, J., Rosner, R., Richards, G. T., & Stoughton, C. 1998, ApJS, 119, 121

Liebert, J., Dahn, C. C., & Monet, D. G. 1988, ApJ, 332, 891

Madej, J., Należyty, M., & Althaus, L. G. 2004, A&A, 419, L5

McGraw, J. T. & Robinson, E. L. 1975, ApJ, 200, L89

McGraw, J. T. 1976, ApJ, 210, L35

McGraw, J. T. & Robinson, E. L. 1976, ApJ, 205, L155

McGraw, J. T. 1977, Ph.D. Thesis, University of Texas at Austin

McGraw, J. T. 1979, ApJ, 229, 203

McGraw, J. T., Liebert, J., Starrfield, S. G., & Green, R. 1979a, IAU Colloq. 53: White Dwarfs and Variable Degenerate Stars, 377

McGraw, J. T., Starrfield, S. G., Angel, J. R. P., & Carleton, N. P. 1979b, SAO Special Report, 385, 125

McGraw, J. T. 1980, NASA. Goddard Space Flight Center Current Probl. in Stellar Pulsation Instabilities p 501-512 (SEE N80-25229 15-90), 501

McGraw, J. T., Fontaine, G., Lacombe, P., Dearborn, D. S. P., Gustafson, J., & Starrfield, S. G. 1981, ApJ, 250, 349

Mestel, L. 1952, MNRAS, 112, 583

Metcalfe, T. S., Winget, D. E., & Charbonneau, P. 2001, ApJ, 557, 1021

Metcalfe, T. S., Salaris, M., & Winget, D. E. 2002, ApJ, 573, 803

Metcalfe, T. S. 2003, ApJ, 587, L43

Metcalfe, T. S., Montgomery, M. H., & Kanaan, A. 2004, ApJ, 605, L133

Metcalfe, T. S. 2001, Ph.D. Thesis, University of Texas at Austin

Montgomery, M. H. 1998, Ph.D. Thesis, University of Texas at Austin

Montgomery, M. H., & Winget, D. E. 1999, ApJ, 526, 976

Montgomery, M. H., Klumpe, E. W., Winget, D. E., & Wood, M. A. 1999, ApJ, 525, 482

Montgomery, M. H., Metcalfe, T. S., & Winget, D. E. 2003, MNRAS, 344, 657

Mukadam, A. S., Winget, D. E., & Kepler, S. O. 2001, ASP Conf. Ser. 226: 12th European Workshop on White Dwarfs, 337

Mukadam, A. S., Kepler, S. O., Winget, D. E., & Bergeron, P. 2002, ApJ, 580, 429

Mukadam, A. S. et al. 2003a, ApJ, 594, 961

Mukadam, A. et al. 2003b, NATO ASIB Proc. 105: White Dwarfs, 227

Mukadam, A. S., et al. 2004, ApJ, 607, 982

Nather, R. E. & Warner, B. 1971, MNRAS, 152, 209

Nather, R. E. 1978, PASP, 90, 477

Nather, R. E., Winget, D. E., Clemens, J. C., Hansen, C. J., & Hine, B. P. 1990, ApJ, 361, 309

- Nather, R. E. & Mukadam, A. S. 2004, *ApJ*, 605, 846
- Nitta, A., Kepler, S. O., Winget, D. E., Koester, D., Krzesinski, J., Pajdosz, G., Jiang, X., & Zola, S. 1998, *Baltic Astronomy*, 7, 203
- Nitta, A., Mukadam, A., Winget, D. E., Kanaan, A., Kleinman, S. J., Kepler, S. O., & Montgomery, M. H. 2000a, *ASP Conf. Ser. 203: IAU Colloq. 176: The Impact of Large-Scale Surveys on Pulsating Star Research*, 525
- Nitta, A., Kanaan, A., Kepler, S. O., Koester, D., Montgomery, M. H., & Winget, D. E. 2000b, *Baltic Astronomy*, 9, 97
- O'Donoghue, D. & Warner, B. 1987, *MNRAS*, 228, 949
- O'Donoghue, D., Kanaan, A., Kleinman, S. J., Krzesinski, J., & Pritchett, C. 2000, *Baltic Astronomy*, 9, 375
- Oswalt, T. D., Smith, J. A., Wood, M. A., & Hintzen, P. 1996, *Nature*, 382, 692
- Petersen, J. O. & Hog, E. 1998, *A&A*, 331, 989
- Pfeiffer, B., et al. 1996, *A&A*, 314, 182
- Pier, J. R., Munn, J. A., Hindsley, R. B., Hennessy, G. S., Kent, S. M., Lupton, R. H., & Ivezić, Ž. 2003, *AJ*, 125, 1559
- Renzini, A., et al. 1996, *ApJ*, 465, L23
- Robinson, E. L., Nather, R. E., & McGraw, J. T. 1976, *ApJ*, 210, 211
- Robinson, E. L., Stover, R. J., Nather, R. E., & McGraw, J. T. 1978, *ApJ*, 220, 614
- Robinson, E. L. 1979, *IAU Colloq. 53: White Dwarfs and Variable Degenerate Stars*, 343
- Robinson, E. L., Kepler, S. O., & Nather, R. E. 1982, *ApJ*, 259, 219

Robinson, E. L. et al. 1995, ApJ, 438, 908

Salaris, M., Cassisi, S., García-Berro, E., Isern, J., & Torres, S. 2001, A&A, 371, 921

Salpeter, E. E. 1961, ApJ, 134, 669

Scargle, J. D. 1982, ApJ, 263, 835

Segretain, L. & Chabrier, G. 1993, A&A, 271, L13

Silvestri, N. M., Oswalt, T. D., Wood, M. A., Smith, J. A., Reid, I. N., & Sion, E. M.  
2001, AJ, 121, 503

Smith, J. A. et al. 2002, AJ, 123, 2121

Standish, E. M. 1998, A&A, 336, 381

Stevenson, D. J. 1980, Journal de Physique, 41, 2

Stoughton, C. et al. 2002, AJ, 123, 485

Strauss, M. et al. 2004, AJ, 128, in press

Van Horn, H. M. 1968, ApJ, 151, 227

Van Horn, H. M. 1971, in IAU Symp. 42: White Dwarfs, 42, 97

Vassiliadis, E., & Wood, P. R. 1993, ApJ, 413, 641

von Hippel, T. & Gilmore, G. 2000, AJ, 120, 1384

Warner, B. & Robinson, E. L. 1972, Nature Physical Science, 239, 2

Warner, B., & Woudt, P. A., 2003, astro-ph/0310072

Weidemann, V. 1990, ARA&A, 28, 103

Winget, D. E., Van Horn, H. M. & Hansen, C. J. 1981, ApJ, 245, L33

- Winget, D. E. & Fontaine, G. 1982, Pulsations in Classical and Cataclysmic Variable Stars, 46
- Winget, D. E., van Horn, H. M., Tassoul, M., Fontaine, G., Hansen, C. J., & Carroll, B. W. 1982a, ApJ, 252, L65
- Winget, D. E., Robinson, E. L., Nather, R. D., & Fontaine, G. 1982b, ApJ, 262, L11
- Winget, D. E., Hansen, C. J., & Van Horn, H. M. 1983, Nature, 303, 781
- Winget, D. E., Robinson, E. L., Nather, R. E., Kepler, S. O., & O'Donoghue, D. 1985, ApJ, 292, 606
- Winget, D. E., Hansen, C. J., Liebert, J., van Horn, H. M., Fontaine, G., Nather, R. E., Kepler, S. O., & Lamb, D. Q. 1987, ApJ, 315, L77
- Winget, D. E., Kepler, S. O., Kanaan, A., Montgomery, M. H., & Giovannini, O. 1997, ApJ, 487, L191
- Winget, D. E. 1998, Journal of Physics: Condensed Matter, 10, 11247
- Winget, D. E. et al. 2003, ASP Conf. Ser. 294: Scientific Frontiers in Research on Extrasolar Planets, 59
- Wood, M. A. 1990, Ph.D. Thesis, University of Texas at Austin
- Wood, M. A. 1992, ApJ, 386, 539
- Wood, M. A. 1995, LNP Vol. 443: White Dwarfs, 41
- Wu, Y. 1998, Ph.D. Thesis, California Institute of Technology
- Wu, Y. & Goldreich, P. 1999, ApJ, 519, 783
- Wu, Y. & Goldreich, P. 2001, ApJ, 546, 469

York, D. G. et al. 2000, AJ, 120, 1579

Zoccali, M., et al. 2001, ApJ, 553, 733

# Vita

Anjum Shagufta Mukadam was born on the 29th of December, 1974 in Bombay, India. At the age of 10, she decided to become an astronomer, to her family's surprise and amusement. She completed her school years in St. Thomas High School and cleared the Senior Secondary Certificate Board Examination (Grade X) in April, 1990. She then joined Bhavan's Junior College to study science and passed the Higher Secondary Certificate Board Examination (Grade XII) in April, 1992. She then joined D. G. Ruparel College and got her Bachelor of Science degree in physics in May, 1995. Anjum pursued physics at the Indian Institute of Technology (IIT), Bombay, and was awarded the Master of Science degree in April, 1997. She then joined Tata Institute of Fundamental Research (TIFR), Bombay as a research scholar for a year. Anjum came to the United States in July 1998, and joined the University of Texas at Austin as a graduate student. She completed her Master's thesis in Astronomy in December 2000, and continued towards her Ph.D. at the University of Texas.

Permanent Address: 662 NE Valarie Ct

Hillsboro OR - 97124

This dissertation was typeset with  $\LaTeX 2_{\epsilon}$ <sup>1</sup> by the author.

---

<sup>1</sup> $\LaTeX 2_{\epsilon}$  is an extension of  $\TeX$ .  $\TeX$  is a collection of macros for  $\TeX$ .  $\TeX$  is a trademark of the American Mathematical Society. The macros used in formatting this dissertation were written by Dinesh Das, Department of Computer Sciences, The University of Texas at Austin, and extended by Bert Kay and James A. Bednar.